Detailed Study of Atomic Silicon Dangling Bond Charge State Dynamics on the Surface of Hydrogen Terminated Silicon (100)-2×1

by

Roshan Achal

A thesis submitted in partial fulfillment of the requirements for the degree of

Master of Science

Department of Physics

University of Alberta

Abstract

Atomic Silicon Dangling Bonds (DBs), which are natural quantum dots, are sites where silicon atoms on a hydrogen-terminated silicon surface have no bound hydrogen atom (leaving an un-reacted sp^3 hybrid orbital). These DBs hold the promise of new ultra-low power devices based on the Quantum Cellular Automata (QCA) architecture proposed for larger quantum dots decades earlier. The need for new devices is growing rapidly as the end of the current technological roadmap approaches. The advancement of these ultra-low power devices, however, is hindered by the fact that many theoretical models and estimations used to design them have yet to be experimentally verified.

In order to move towards the effective development of DB prototype devices, fundamental physical properties of DBs must first be characterized and studied. One of the properties inherent to DBs on the surface of a hydrogen-terminated n-type silicon (100) wafer (with a 2×1 surface reconstruction) is their ability to store electrons. They can exist in a positive, neutral, or negative charge state when storing zero, one, or two electrons respectively. At low temperatures (4 K) when imaging a DB with a Scanning Tunneling Microscope (STM) at particular bias voltages, fluctuations of the DB charge state can be observed in the image that are driven through influence of the STM tip. An analysis framework was developed based on

a correlation analysis method borrowed from biophysics to study the manifestations of these fluctuations between charge states in the STM tunneling current itself.

Through these studies the dependence of the transition rates between charge states on the radial distance of the STM tip (from the DB centre) was uncovered, along with preliminary studies on the sensitivity of these rates to applied bias voltage. The charging pathway between states was also identified, showing a linear pathway between negative–neutral–positive charge states with no direct transition between the negative and positive charge states.

It was found that the filling rate of electrons into the DB from an STM tip had an exponential relationship with radial separation between the tip and the DB centre. The rates were found to be 50 Hz–3000 Hz within the scope of the experiments. These rates also showed little dependence on applied sample bias voltage over the range of 1.30 V to 1.45 V.

The behaviour of the emptying rates of electrons into the silicon bulk showed a very different relationship with radial tip distance. It was found that the emptying rates were almost independent of radial tip separation, having a flat and constant value between 50 Hz–1000 Hz. The value of the emptying rates depended quite sensitively on applied sample bias voltage, however, and it was found that these rates increase with increasing bias voltage. The exact form of this dependence still requires further investigation. The results of these experiments also hint at what the dynamics of the DB charging might be in the absence of the STM tip.

Using the calculated rates for both the filling and emptying processes, stochastic simulations of the DB charging dynamics were created in order to investigate both

the success of the correlation method, and the validity of the results themselves. The simulations of charge state dynamics using the experimental rates showed good agreement with these experimental data. The simulations also showed strong support for the linear charging pathway determined experimentally.

The results and analytical techniques described here open the doors to study more complex systems of interacting DBs as well, which is another important step towards making practical ultra-low power devices.

To infinity...

and beyond!

-BUZZ
LIGHTYEAR

Acknowledgments

Knowing nothing about the field of Condensed Matter Physics, I walked through the doors of the University of Alberta for the first day of Graduate school a bit worried. Since then I was able to become immersed in a huge field of science, while also benefiting from a great entrepreneurial atmosphere. However, I know I've only scratched the *surface* (science) of the field, and can't wait to get further into the *bulk* of it!

First off, I'd like to thank Dr. Robert Wolkow. When we first met I was planning to change fields for my graduate studies to study neurons, or even attend medical school. Dr. Wolkow made an offer I couldn't refuse though, with the promise that "I would only be limited by my creativity in his lab." This has certainly proven true over the course of this degree. In his group Dr. Wolkow has been supportive of many scientific endeavours as well as business ventures, and I am very grateful for the opportunities I have been given.

I'd like to especially thank Marco Taucer for taking the time to help me get initially acclimated to the lab, and always being a willing and eager collaborator or troubleshooter. I'd also like to thank Dr. Moe Rashidi, who worked tirelessly with me to establish and maintain our scanning tunneling microscope; without you many of these measurements wouldn't have been possible.

I really appreciated the world class training on the microscopes from Dr. Paul Piva and Dr. Jason Pitters. You both have very different approaches, and it was fantastic to learn them both. Mark Salomons and Martin Cloutier, you guys are amazing, and have helped take problems that would need months to fix and minimized the downtime to days.

These last few years wouldn't have been nearly as enjoyable without the rest of

the Wolkow group either, so thank you to Taleana Huff, John Wood, Erika Lloyd, Peter Legg, Hatem Labidi, Ken Gordon, Bruno Martins, Mohammad Koleini, Lucian Livadaru, and Radovan Urban. It has also been a pleasure meeting new friends in Edmonton with such diverse backgrounds, and of course having people to throw a Frisbee around with every once in a while when the weather isn't all snow and ice.

I'd also like to thank all of my friends who slogged through endless assignments with me during Undergrad, it was an important lesson to learn that Physics is best accomplished with a good group of people. I'd like to thank all of the professors too who gave me the chance to spend a summer or two in their labs during my Undergraduate degree. Through working with you I was able to explore many areas of research, be mentored by experienced Graduate students, and gain a unique perspective, as well as an arsenal of tools.

Finally, no acknowledgments section would be complete without thanking my family. Although, it would fill another thesis to thank you all properly for everything you've done, since I couldn't have accomplished anything in life without all of your contributions, big or small. I'd like to thank my Mother for always supporting me and my endeavours, encouraging me to learn languages, and keep rounded interests. I'd like to thank my Father for instilling a scientific curiosity in me at an early age, constantly pushing me to do a job the right way, not the easy way, and to take risks. Thank you to my Aji and Aja (grandparents) who have given me unwavering support and helped me become a better student. Also thank you to my Ba and Dada (grandparents) who have always been inspirational and supportive as well. I'd like to thank my Kaka (uncle) and family who are always willing to step in and help, along with all my other uncles and aunts. Last but not least, I'd like to thank my girlfriend, Jordan, you've been with me through this whole ride, putting up with late nights in the lab, and occasionally obscure hours. Your understanding and support has been endless and I truly appreciate it.

Contents

List of Figures

Chapter One

Introduction and Background

1.1 Current State of Technology

The technological world is fast approaching a cross roads. The current silicon chip based technologies that are ubiquitous in most modern day devices are approaching their physical size and performance limits [1]. Due to this, the present trend in increasing computational power and speed with each new generation of devices cannot be maintained [1, 2]. Without the ability to improve upon speed and performance of computing technologies the consumer market risks stagnation [1, 2]. Many areas of research and industry are devoted to finding a viable road for new technologies which can overcome the physical limitations of the current silicon based architecture. Among these candidate technologies include spin systems [3], block co-polymers [4], and atomic silicon dangling bonds [2, 5].

1.1.1 At the Atomic Limit

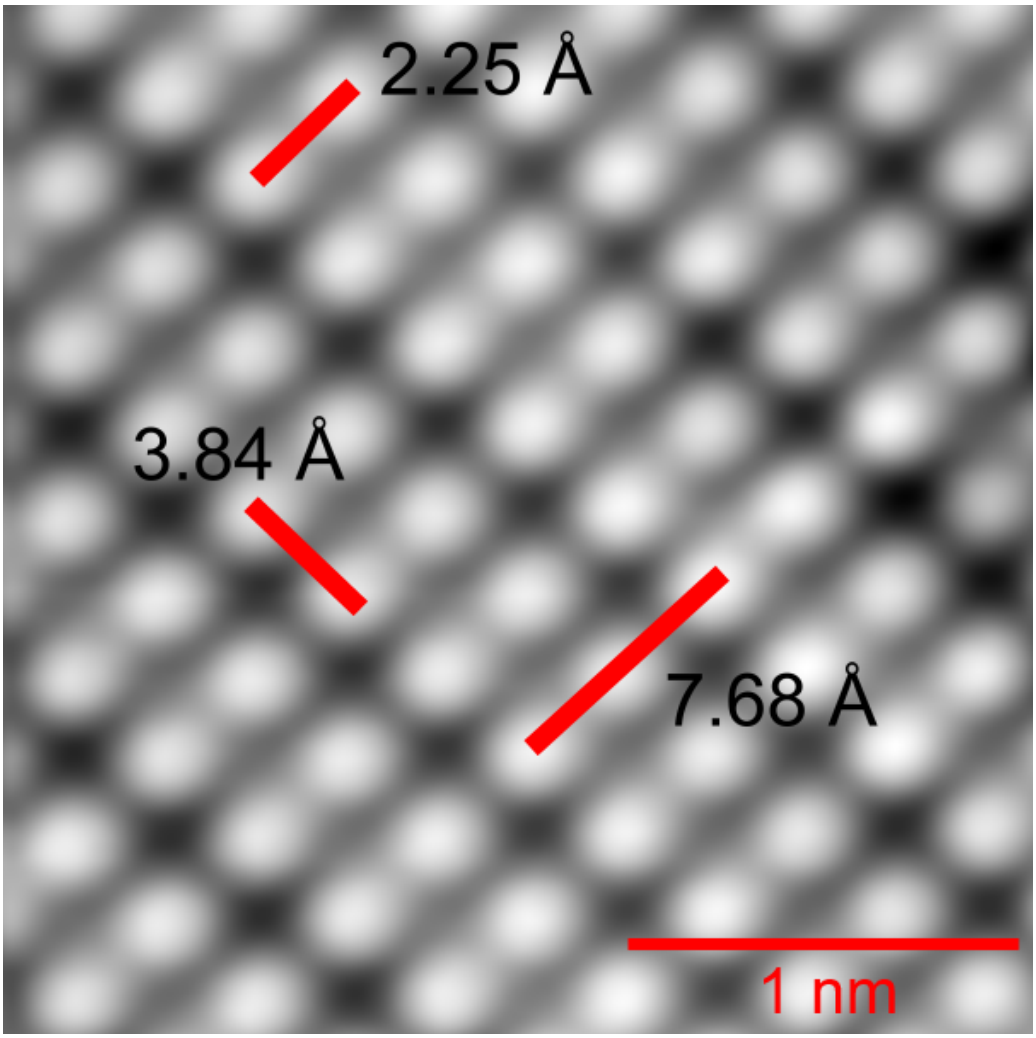

Figure 1.1: A high resolution STM image of the surface of a hydrogen-terminated silicon (100) wafer (n-type) with a 2×1 surface reconstruction. The bright regions correspond to the location of hydrogen atoms. 2×1 cells of hydrogen atoms (dimers) can be observed (with 2.25 Å spacing) forming dimer rows orthogonal to the orientation of the dimers themselves (with 3.48 Å spacing). The image was acquired at a sample bias voltage of 1.6 V with a current set-point of 30 pA. The distances between atomic centres are indicated with black lines [2].

Atomic silicon dangling bonds are lone sp^3 hybrid orbitals of un-reacted silicon atoms on the surface of a hydrogen-terminated silicon chip. These dangling bonds (DBs) can localize (store) zero, one, or two electrons making them natural atomic quantum dots [2, 6, 7]. DBs can only be visualized through use of highly specialized machinery such as an atomic force microscope or scanning tunneling microscope (STM). These machines have the ability to image samples with atomic resolution and in addition also allow for the manipulation of single atoms [2, 5, 8, 9]. Figure 1.1 shows an example of an STM image of hydrogen atoms on the surface of a hydrogen-terminated silicon (100) wafer (n-type) with a 2×1 surface reconstruction, while figure 1.2 shows a high resolution image of a DB. More images of these two features can be found in Appendix A. The resolution of these images is at the edge of what is currently possible with present microscope technologies. With DBs taking up the room of approximately an atom of hydrogen and possessing quantum dot properties, they present a unique opportunity to create the ultimate nanoscale devices.

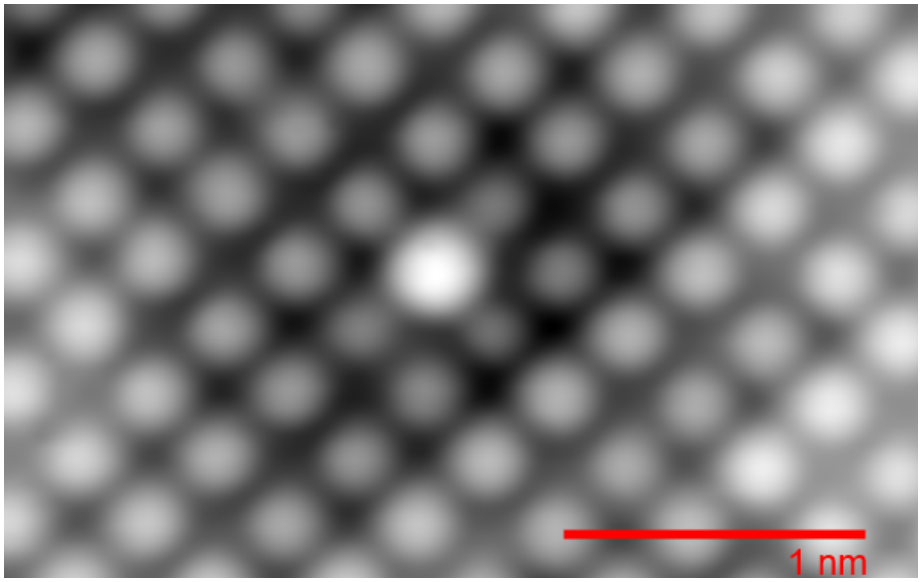

Figure 1.2: A high resolution STM image of an atomic silicon dangling bond on the surface of a hydrogen-terminated n-type silicon (100)–2 × 1 wafer. The dangling bond is the brightest feature in the middle of the image, where a hydrogen atom has been selectively removed to leave an open orbital. The image was acquired at a sample bias of 1.6 V and a constant current of 30 pA.

1.1.2 Quantum Cellular Automata

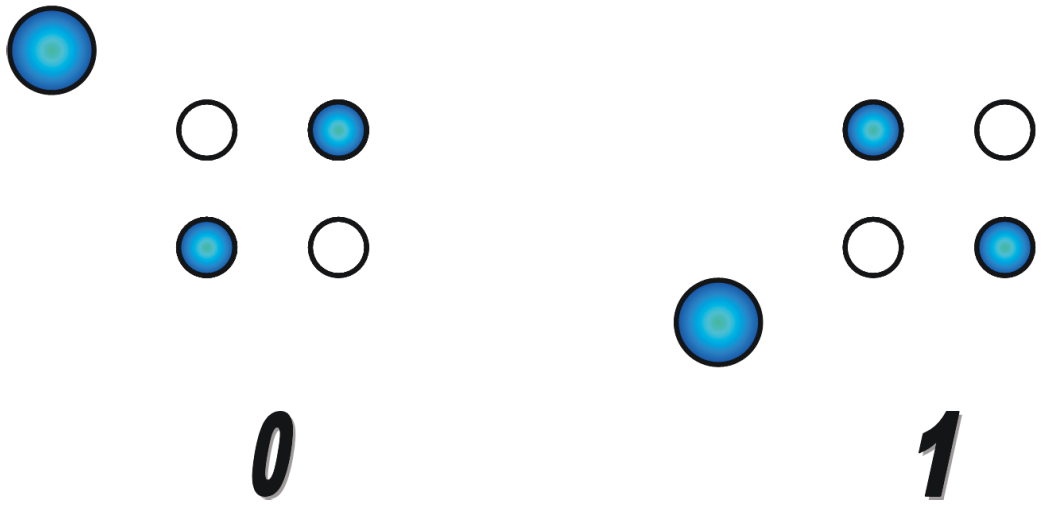

Figure 1.3: A simplified illustration of four tunnel coupled dangling bonds sharing two electrons (in blue) to form a QCA cell. The location of a larger control charge (larger circle) can influence the location of the electrons inside a QCA cell, causing the electrons to rearrange to minimize interactions with each other. By placing the control charge in one of two positions, two binary states of the QCA cell can be achieved ("0" and "1").

Lent et al. have previously proposed an architecture known as Quantum Cellular Automata (QCA) based on larger quantum dots where binary information can be transmitted along a wire made up of 2×2 cells of quantum dots containing two electrons [10–12]. This basic QCA structure, the "binary wire", has only two states: logical "0" or "1". Figure 1.3 shows an illustration of the locations of the electrons in a QCA cell for both states. The state of the cell can be changed by an electrostatic input arising from several spatially controlled electrons. When this larger charge is brought near a quantum dot containing an electron, the electrons in the QCA cell automatically switch positions (due to electrostatic repulsion) to reduce their interaction energy, thereby changing the state of the cell. Placing many QCA cells into a wire structure forces the cells to all align in the same state to reduce their interaction energy as well (Figure 1.4). Now when the state of the first cell

is switched, the rearrangement of electrons propagates along the wire (transmitting the binary information) to the end state which can be read as a "0" or "1". By implementing this scheme with atomic silicon dangling bonds, it has been theorized that the automatic rearrangement will allow the state information to be transmitted across the wires using very little power and at terahertz frequencies [2]. In addition to creating binary wires, the atomic silicon DBs under a QCA architecture may be able to create nanoscale circuit components such as logic gates [2, 12–16].

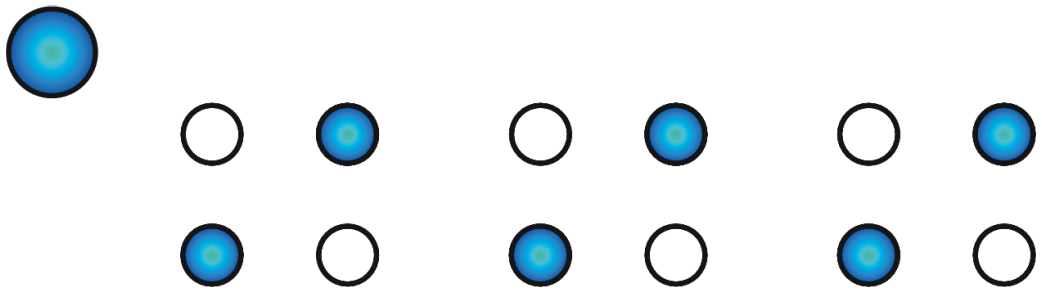

Figure 1.4: An example of a line of QCA cells forming a binary wire. The control charge at the start of the wire sets the state. When this charge is moved, the state of the first cell switches as in figure 1.3 and this change cascades down the wire such that binary information can be transmitted.

1.2 The Fundamentals

One limitation in the advancement of these QCA atomic silicon DB technologies is the fact that many theoretical models and estimations used to design these devices have yet to be experimentally verified [7, 17]. Experimental measurements are of paramount importance to the effective design of circuits, and need to be realized before further development can take place. Fundamental quantities such as the energy required to switch QCA cells between logic states, and electron transfer rates into and out of a DB need to first be better characterized and understood.

1.2.1 Electron Transfer Rates

An STM with a sufficiently sharp tungsten tip enabled a detailed study of the electron transfer rates into and out of DBs on the surface of a hydrogen-terminated n-type silicon (100)–2 × 1 wafer. The preparation of the wafer and experimental equipment/techniques are outlined in Chapter 2 and Chapter 3. The STM tip provided a source of electrons to inject into a given DB with random tunneling events and the bulk silicon substrate provided a drain to where the electrons could leave. By monitoring the STM tunneling current at particular radial distances from a DB centre it was possible to observe the signature of single electron movements into and out of the DB in the form of telegraph noise. A simple model was constructed to describe the observed behaviour of the DB system (Chapter 4) that helped guide more thorough investigations. In order to extract the filling (into) and emptying (out of) rates of a DB from the tunneling current at each radial distance, an analysis method was borrowed and adapted from biophysics and fluorescent chemistry (Chapter 5), where it was used to study protein folding and fluorescent lifetimes respectively [18–20]. The adaptations to the analysis have the potential to increase the ease of application to many other systems with similar signals. In addition to the dependence of the filling and emptying rates on the radial tip distance, their sensitivity to applied sample bias voltage was also explored. The calculated rates were eventually used in stochastic simulations of telegraph noise (Chapter 6) to determine if the rates were able to produce results consistent with nature. The simulations also provided a way of evaluating the performance and accuracy of the analysis methods. The impact, and extensions of this work are discussed in Chapter 7.

Chapter Two

Experimental Setup and Techniques

2.1 The STM

The Scanning Tunneling Microscope, better known as STM, has been a major contributor to many scientific discoveries over the last two decades [21–23]. It was first proposed, designed, and built by two researchers at IBM Zurich in the early 1980's, G. Binning, and H. Rohrer [24] who forever changed the world's ability to visualize and manipulate atoms. As such, they were rapidly awarded the Nobel prize in Physics in 1986 for their research and innovation. The popularity of the STM, due to the novel abilities it granted researchers, has only grown with time leading to many advances in their design and functionality. Companies such as Omicron (now a division of Oxford Instruments) have even commercialized STMs in order to capitalize on this demand. At the current forefront of these advances are ultra-stable low temperature (LT) STMs. These LT-STMs reduce environmental and thermal noise to such a degree that near thermal-drift-free sub-Angstrom imaging has become routine. More importantly, in addition to the exquisite resolution, is the stability of the STM tip placement at low temperatures. Atomically precise tip placement and the ability to stably fix the tip at a constant height (without control electronics on) for an extended period of time has enabled experiments and signal acquisitions/averaging that would otherwise be impossible at room temperatures. With the high resolution and stability of these LT-STMs the atomically precise manipulation of surface atoms is also possible, giving rise to whole fields dedicated to nanoscale fabrication [2, 9, 13, 25].

While these modern LT-STMs are significantly more advanced than their early predecessors, they function on the same basic principals and components. In order to image atoms a sharp tip is required to scan the surface of a sample, along with a suitably clean sample. A potential difference (bias) is placed between the tip and sample (the tip is grounded, so the bias is always referring to sample bias) such that a measurable tunneling current can be detected. To detect this current special pre-amplifiers are needed which are sensitive down to femtoamp levels. As the tip is moved along the surface in an x-y plane through the use of piezo motors, the tunneling current varies depending on location. Feedback electronics measure the tunneling current and alter the z height of the tip in order to maintain a constant current reading as the tip moves along the sample. The differences in height are mapped out to a computer screen to form an image. Bright regions are where the tip has been moved away from the sample and dark regions are where the tip has moved closer to the sample. Figure 1.1 shows an STM image recorded of hydrogen atoms on a silicon surface. With the feedback electronics off (tip at a constant height), another imaging mode is possible largely due to the stability of the LT-STMs. The constant height imaging mode provides some benefits when compared to constant current imaging. At a constant height the field effects of the tip are uniform throughout the image, and it is possible to image inside the band-gap of a given sample. If the tip is kept at a constant height while it is scanning, the bright regions in the image correspond to higher tunneling current, and the dark regions correspond to lower tunneling current. Figure 2.1 shows a basic schematic of an STM apparatus.

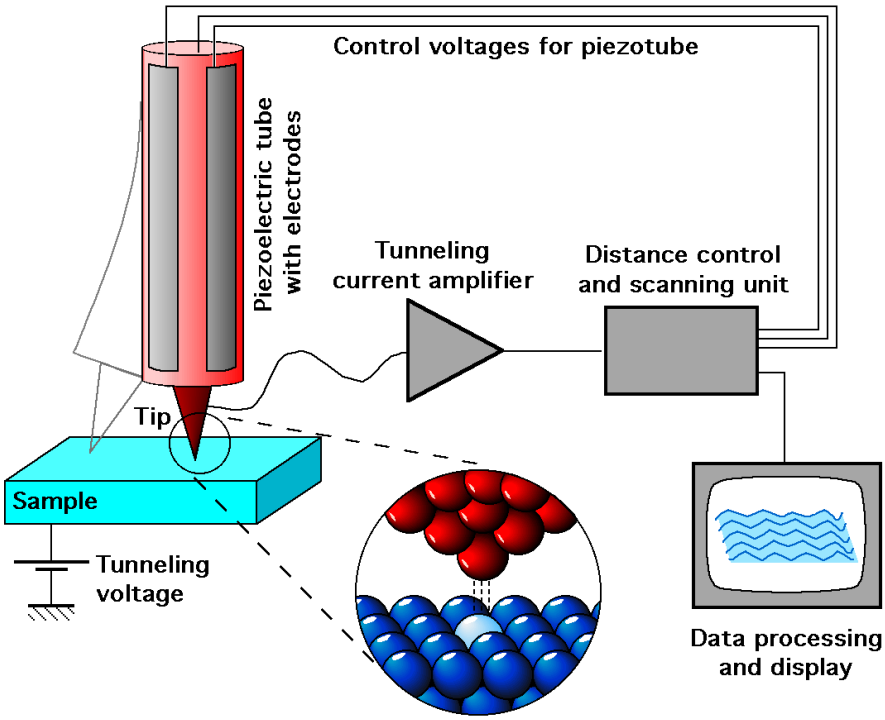

Figure 2.1: [26] A basic schematic of an STM setup. There is a sharp tungsten tip attached to a piezo motor and a sample of interest below. A bias is created between the tip and sample in order to create a measurable tunneling current of electrons between the two.

2.1.1 The Machine

Our modern LT-STM (or simply referred to as STM as well) is a hybrid combination of a commercial Omicron STM scan chamber, with all additional supporting chambers custom built in-house. Figure 2.2 shows the whole STM apparatus in the lab. Each chamber has a specific purpose, which will be described in sequence.

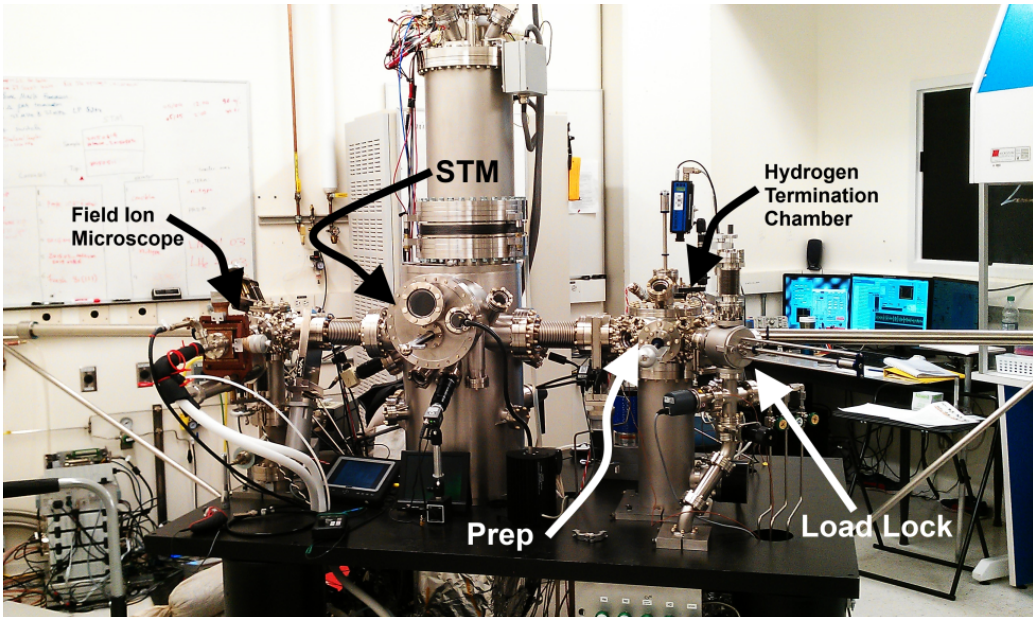

Figure 2.2: The entire LT-STM apparatus with the various chambers used for sample and tip preparation. The machine operates at liquid helium temperatures (4 K) and at pressures of 10^{-11} Torr.

The STM operates at ultra-high vacuum pressure (UHV) generally between 10^{-10} to 10^{-11} Torr. In order to maintain these low pressures it is very important to minimize or eliminate the ability for contaminants (such as water or other gases) from entering the machine. If the vacuum is compromised (broken) it could mean weeks of downtime in order to return to the low pressure regime. Due to this restriction on contaminations it might seem impossible to easily place new samples or tips inside the STM without breaking vacuum. In order to avoid breaking vacuum each time something needs to be removed or placed into the STM a Load Lock (LL) chamber (shown in figure 2.3) is utilized. This chamber is sealed off from the main STM and can be readily brought to atmospheric pressures in order to place or retrieve samples or tips. The LL is specially designed to be as small as possible in order to minimize the surface area where water and contaminates can settle, and to minimize the volume required to be pumped in order to create a vacuum inside. With a small volume (and surface area), it is quick to bring the pressure inside the LL down to approximately

10^{-8} Torr with a combination of a roughing pump and a turbomolecular pump. At this pressure most of the contaminates of concern have been pumped out, and the LL can be opened into the rest of the machine in order to retrieve or deposit items.

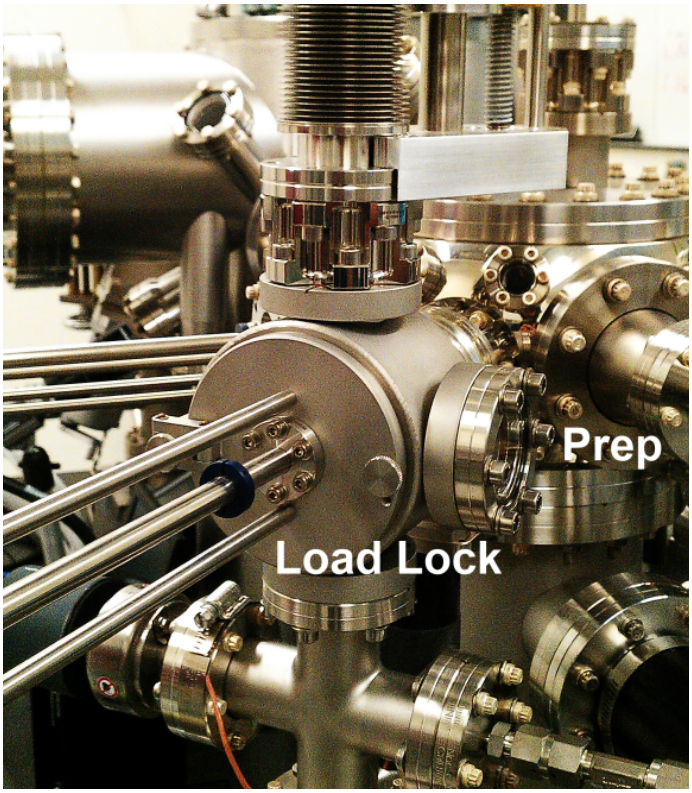

Figure 2.3: The load lock chamber and the prep chamber of the STM apparatus. The load lock chamber is a small chamber that is the main entry/exit point for samples and tips to be placed in or removed from the STM. It is small with minimal surface area so that it can easily be brought up to atmospheric pressures, and subsequently pumped back down to high vacuum levels. The prep chamber acts as a storage chamber and hub for transporting items between other chambers.

After the LL is pumped down to low pressures, it is opened to the Prep Chamber (PC) (Figure 2.3). The PC is a general hub inside the STM where tips and samples can be stored or transferred from the various other chambers. The PC has to be maintained at low pressures as well because freshly prepared samples are passed through this chamber and risk contamination at higher pressures. Ion pumps are

used inside this chamber to achieve low pressures. Titanium Sublimation Pumps (TSPs) are also included in the chamber and are activated when large quantities of hydrogen gas need to be pumped in order to lower the pressure further. Each chamber inside the STM is separated by a gate-valve, which are only opened when a transfer needs to occur.

Directly off of the PC is the Hydrogen Termination Chamber (HTC) (Figure 2.4). Samples that are stored in the PC can be transferred into the HTC for processing. The HTC, like the PC, also has an ion pump and TSP in order to reach low pressures (especially after sample preparations). In addition the HTC also has a transfer arm inside that is connected to an external power supply such that a current can be passed through the held sample in order to heat it. The HTC also has a tungsten filament connected to an external power supply, which is necessary in the hydrogen termination process (described in section 2.2.2). Figure 2.4 shows the HTC along with the illuminated tungsten filament. The temperature of the sample can also be recorded through the use of the external pyrometer shown in figure 2.4.

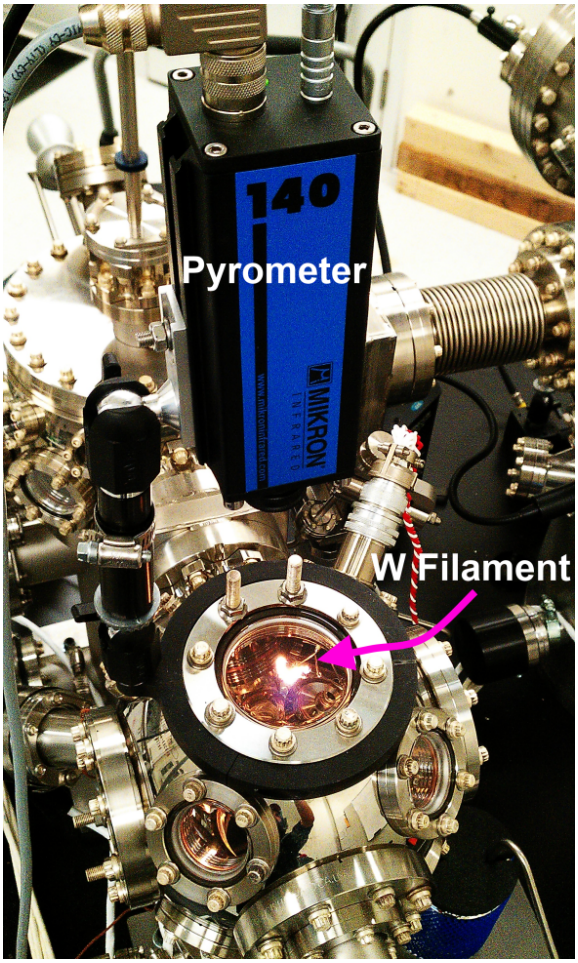

Figure 2.4: The hydrogen termination chamber is where all in vacuum sample preparation takes place. There is a tungsten filament which can be heated to approximately 1800 °C through the use of a DC current in order to break hydrogen gas into atomic hydrogen. Hydrogen gas can be added into the chamber through the use of a leak valve.

The main STM scanning chamber is shown in figure 2.2. Within this chamber is the STM scanner and sample. All experiments take place inside this chamber. Directly adjacent to the main STM chamber is the Field Ion Microscope (FIM) chamber (Figure 2.5). Within this chamber the tungsten tips can be further sharpened and cleaned. With an FIM setup it is possible to etch the tungsten tip down to a sin-

gle atom at the apex. A Residual Gas Analyser (RGA) is utilized inside the FIM chamber to monitor the pressure of helium and nitrogen gases during the etching process.

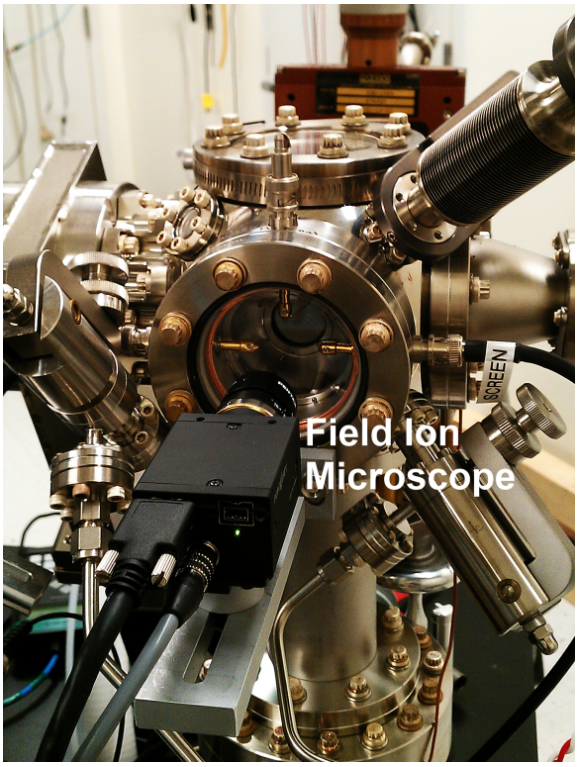

Figure 2.5: The field ion microscope chamber. Here the tungsten tips can be further cleaned and sharpened in vacuum. The FIM also allows for the controlled etch of the tungsten tip down to a single atom at the apex.

2.1.2 Noise Considerations

Since the tunneling current is so small (usually on the order of picoamps) it can be influenced quite dramatically by environmental noise. There are several significant contributors to the noise in an STM current, the most common of which is 60 Hz noise due to the power supplies of the majority of equipment in the lab and surrounding area. This noise is typically reduced by using well shielded power supplies, limiting the quantity of electronics in proximity of the STM, and also ensuring

proper grounding of equipment. Grounding issues (ground-loops) are avoided by using a common ground for all equipment. In addition to the 60 Hz noise, there is also low frequency mechanical noise present in the environment near 2–10 Hz. The reduction of this noise is achieved through the use of a large concrete slab upon which the STM table sits, and mechanical air legs to damp out many of the vibrations along with a heavy table top. The STM scanner/stage itself is held with springs that have a mismatched resonance frequency with the rest of the machine in order to reduce the transfer of energy to the scanner [27]. Metal fins surround the stage as well in a magnetic field to take advantage of Eddy current damping to further reduce vibrations [27].

In order to be measured, the small tunneling current signal needs to be amplified through the use of a current pre-amplifier. Beyond the environmental noise considerations, the electronics within the pre-amplifier and STM introduce noise as well in the form of Johnson noise and shot noise. The equation to calculate the shot noise is given by [23]:

$$I_{shot} = \sqrt{2eI\Delta F}, \tag{2.1}$$

where e is the charge of an electron in Coulombs, I is the measured DC current in amps, and ΔF is the bandwidth of the device [23]. In the case of the LT-STM electronics, the bandwidth of the pre-amplifier (3 dB) is specified at 800 Hz, and a typical value of tunneling current is 50 pA. Putting the appropriate values into equation 2.1,

$$I_{shot} = \sqrt{2 \times (1.6 \times 10^{-19}) \times (50 \times 10^{-12}) \times 800}, \tag{2.2}$$

$$I_{shot} = \sim 0.113 \text{ pA} . \tag{2.3}$$

Johnson noise I_J is given by [23]:

$$I_J = \sqrt{\frac{4k_B T \Delta F}{R}}, \tag{2.4}$$

where $k_B T$ is the Boltzmann constant, T is the temperature of the device, R is the resistance of the device, and ΔF is the bandwidth of the device [23]. The STM pre-amplifier is kept at room temperature, and has a feedback resistor of $3 \times 10^9\ \Omega$ [27]. Again, using the appropriate values inside equation 2.4,

$$I_J = \sqrt{\frac{4 \times (1.38 \times 10^{-23}) \times 300 \times 800}{3 \times 10^9}}, \tag{2.5}$$

$$I_J = 0.066 \text{ pA} . \tag{2.6}$$

The total theoretical root mean square (RMS) contributions from both noise sources together is less than 1 pA, with peak-to-peak current noise measured on the instrument as ∼1-2 pA.

2.1.3 Low Temperature

The STM is able to operate at a wide range of temperatures. It is able to be utilized at room temperature (300 K) or can be cooled with cryogenic fluids to temperatures of 77 K with liquid nitrogen and 4 K with liquid helium.

Lower temperatures provide directly observable improvements in STM performance and allow for measurements that are not conventionally possible in other STM systems. At the coldest operating temperature of 4 K the most noticeable improvement is the reduction in thermal-drift in the images. Thermal-drift results in an uncertainty of the position of the tip over time in both the x-y plane along with its z position. By reducing this issue, it is possible to place the tip with atomic precision in the x-y plane and ensure it remains there for an extended period of time such that an experiment can be carried out in a particular spatial location. In addition to the stability in the x-y plane, the z height stability allows for the tip to be locked at a fixed height (by deactivating feedback control) for extended periods of time without requiring active feedback controls from the STM electronics. At warmer temperatures, without feedback control, the thermal-drift in the system would change the z height and pose the risk of crashing the tip into the sample, or drifting away such

that no signal can be detected, both of which are undesirable.

Beyond the reduction of thermal drift, the next most noticeable improvement is the pressures obtained inside the STM chamber. The already extremely low pressures inside the STM chamber are brought down even further at lower temperatures. The cold walls of the chamber act as a cryo-pump and trap additional ambient gases. Slight warming of the chamber can result in large pressure spikes as a result of these gases being re-released. The exact pressure inside the STM chamber is not known since placing a gauge inside would lead to additional unwanted heating. With extremely low pressures inside the STM chamber the risk of sample contamination is significantly reduced. At warmer temperatures after several days unwanted particles begin to appear on the STM images (sample contamination), and eventually require the sample to be changed. At 4 K samples have been kept inside the chamber for nearly four months before there was a noticeable degradation in surface quality.

2.2 Sample Preparation

2.2.1 The Crystal

The samples utilized in this investigation were n-type crystalline silicon wafers with a 100 orientation. The silicon was degenerately doped with arsenic, with an approximate concentration of $2 \cdot 10^{19}$ $\frac{\text{As}-\text{atom}}{\text{cm}^3}$ giving a resistivity of 0.003-0.004 Ωcm. Silicon itself is an indirect band-gap semiconductor with a band-gap energy of 1.12 eV at room temperature, which increases slightly at lower temperatures (1.17 eV at 0 K) [28]. The degenerate doping is currently a requirement for low temperature STM investigations due to the lack of mobile charge carriers available in less doped silicon at 4 K. A lack of mobile charge carriers prevents a measurable tunneling current from being achieved.

The preparation of a clean sample is paramount in order to maintain UHV conditions, as well as avoiding sample contamination. All out of STM (in atmosphere) processing is done inside a laminar flow hood. Silicon can become contaminated very easily with nickel from stainless steel, which shows up as well known surface

defects at the atomic scale [29]. In order to avoid nickel defects, an Omicron molybdenum sample holder, and molybdenum tools are used along with various ceramic tweezers. The silicon wafers are cut (cleaved) to length using a molybdenum scribe. The dimensions of the crystal are ∼11–12 mm in length to span the sample holder, and 1.5–3.2 mm in width. Figure 2.6 shows a thin mounted crystal in a sample holder inside the HTC ready for in vacuum processing. The width of a wafer is an important factor in the overall sample quality; narrower wafers have less surface area to degas, resulting in shorter preparation times and the release of less potential contaminants. The narrow wafers also heat more uniformly, allowing for the whole sample to be prepared at a given temperature instead of having a large temperature gradient across the wafer (leading to incorrect surface reconstructions [30–32]).

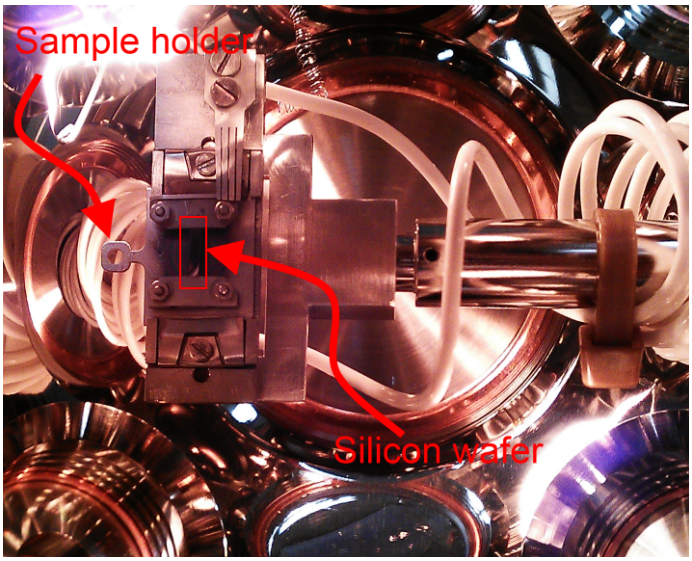

Figure 2.6: A molybdenum Omicron STM sample holder inside the hydrogen termination chamber. A very slim silicon wafer is mounted across the sample holder.

2.2.2 Surface Termination

Once placed in vacuum, the silicon wafer along with the sample holder need to be degassed in order to remove any water or other contaminants that may be present on them, which could be released during sample preparation (ruining vacuum or

the prepared sample). In order to degas the wafer a DC current is run through it until a constant temperature of 600 °C is achieved. The sample is maintained at the temperature for between 12–24 hours.

After the wafer has been thoroughly degassed, the native oxide layer formed in atmosphere that protects the surface of the silicon needs to be removed in order to passivate the surface with hydrogen. The oxide is removed by rapid repetitive heating (flashing) of the wafer to 1250 °C for 1–3 s, well beyond the threshold temperature where oxide tends to be removed [33, 34] along with carbides contaminates [34]. The flashing process is repeated between 5–10 times.

To hydrogen terminate the now bare surface of the silicon wafer, high purity gas-phase hydrogen first needs to be "cracked" into atomic hydrogen. The hydrogen is "cracked" through the use of a hot tungsten filament (pre-degassed) at a temperature between 1600–1900 °C. The first step of the termination process is to leak hydrogen into the hydrogen termination chamber to a pressure of 10^{-6} Torr using the leak valve. Once this pressure is maintained the cracking filament is activated. The wafer is rapidly flashed to 1250 °C one final time, then quickly brought down to a temperature between 300–330 °C for approximately two minutes and thirty seconds. After this time the current to heat the sample is turned off, the cracking filament is turned off, and the hydrogen leak valve is closed. If all the steps were successful the silicon wafer will now have a 2×1 surface reconstruction terminated with hydrogen (H:Si(100) 2×1) [35, 36] (Figure 1.1). The final temperature of the sample should always be recorded because it is a strong indication of the quality of the surface. If the temperature is too low it is possible to accidentally create 3×1 [30] and 1×1 [31] surface reconstructions. If the temperature is too high, then the surface has likely not terminated as thermal processes can prevent the hydrogen atoms from bonding to the silicon surface [32].

2.3 The Tip

The ability for an STM to achieve atomic resolution of the H:Si(100) 2×1 surface relies heavily on a well prepared and sharp tip. In the experiments undertaken in this

thesis, polycrystalline tungsten wire was used as the tip material. In order to obtain the best tips for imaging and manipulation of atoms, a multi-step tip preparation process was followed.

2.3.1 Chemical Etching

The first step to reaching an atomically sharp tip is cutting sections of tungsten wire into 5–8 cm segments. These wires need to be cleaned thoroughly to ensure any potential contaminants are removed. The wires were initially submerged into a beaker containing methanol and sonicated for ten minutes. The wires were then submerged in acetone and sonicated for an additional ten minutes. Finally the wires were submerged in distilled water and sonicated for ten more minutes. The clean wires are stored in this distilled water bath until they are needed for tip preparation.

Once a tip needs to be prepared a segment of wire is removed from the distilled water, and placed into the chemical etching setup shown in figure 2.7. The setup consists of a low current cut-off circuit, a cathode, tip holder (anode), a 2M NaOH solution, and a fine positioning motor.

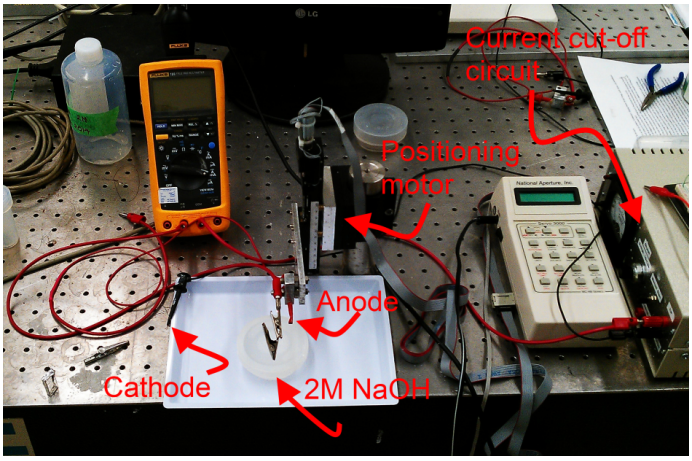

Figure 2.7: The chemical etch setup used in the lab to sharpen the tungsten wire down to a tip radius of 10–30 nm. The setup consists of a 2 M NaOH solution, a cathode placed in solution, an anode (the tungsten wire to be etched), a low current cut-off circuit, and a fine positioning motor to move the tip/wire into and out of the solution.

The tip is brought orthogonally towards the surface of the NaOH solution using the positioning motors, and then several centimetres of the tip are submerged into the solution. A current is run through the tip for 30 s in order to etch away the oxide later on the outside of the wire. When the wire is removed from the solution the etched area should have a silver gleam.

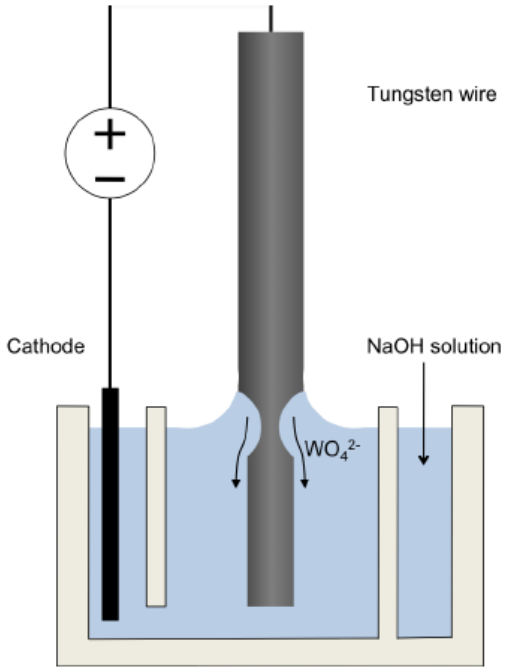

Figure 2.8: [37] A simplified view of a tip chemical etching station, and a tungsten wire being etched through the application of a DC current into the system. The tip is etched the most quickly near the surface and creates a very thin region. Once the wire becomes too thin the larger submerged portion of the tip drops off, leaving a sharp tungsten tip. The inner walls of the setup reduce the turbulence of the hydrogen bubbles produced at the cathode, which would otherwise disrupt the sensitive etching process.

In order to sharpen the tip, several millimetres of the now clean wire are re-submerged into solution. The current is again run through the tip in order to cause the etching reaction. Figure 2.8 shows the reaction process where the tungsten near the surface is eaten away first, thinning the wire, thus creating a tapered etch. When the tungsten has been eroded down sufficiently the less etched portion of the wire remaining in solution will drop off as its weight can no longer be supported by the thin wire. The remaining wire has now been sharpened down to a radius of ∼10–30 nm [38]. This level of sharpness is adequate for most STM applications, though more in vacuum processing is required. Before the tip can be placed inside the STM

it needs to be mounted in an Omicron tip holder. The etched wire is cut about 0.7–1 cm down from the apex and mounted in the holder. If the tip is too long it may become damaged inside the STM during transport. If the tip is cut too short it will not be able to reach the sample surface.

2.3.2 E-Beam and Field Emission

In order to further process the tip in vacuum for use in the STM the chemically etched and mounted tip must undergo e-beam heating and field emission procedures. These procedures, both taking place inside the FIM chamber of the STM, help clean and stabilize the tip.

The field emission of the tip is first characterized by applying a bias voltage to the tip. The high field produced at the apex of the tip from the applied bias is sufficient to lower the energy barrier for electrons to tunnel into vacuum and be collected as a current [39–41]. The sharper the tip the larger the field at the apex, and the lower the bias voltage required to cause field emission. Extremely sharp tips can field emit $\sim$1 nA of current with between -300 – -1000 V. If the tip is unable to field emit in this regime it is likely too dull for use. The emitted electrons are collected via a grounded tungsten filament in close proximity (several millimetres) away from the tip apex. The tip can be left to sit emitting at 100–500 nA for hours in order to ensure that a stable tip structure can be maintained and to further clean the tip through resistive heating.

The tip apex can also be heated to high temperatures through e-beam bombardment in order to remove the thin oxide layer formed after the chemical etch in atmosphere. A bias of +500 V is applied to the tip. Current is run through the tungsten wire in close proximity to the tip in order to boil off electrons. The filament is at a temperature of 1600 °C. The electrons are accelerated through the applied field towards the tip, causing it to heat on impact. A measurable current of 3–5 mA through the tip is also produced as a result of the flow of electrons. This current is maintained for 3–10 s, transferring a power of approximately 2.5 W to the tip apex region.

The process of e-beam and field emission is repeated until the field emission voltage no longer decreases and only shows rare jumps in emission current. At this point the tip is no longer becoming sharper or cleaner, and is ready for use in the STM. Any further e-beaming or field emission now risks significantly dulling the tip. The tip can optionally be processed further still through the use of a field ion microscope to etch it down to a single atom at the apex.

2.3.3 Field Ion Microscopy

The field ion microscope (FIM) was originally designed to provide atomic resolution of certain materials [42, 43], and is an invaluable tool to image and characterize the tungsten tip apex. It was later discovered that by controlling the bias voltage applied to the tip, along with the pressure of certain gasses it was possible to initiate a field-controlled etch of the tip down to a single atom at the apex [38]. In a pure FIM imaging mode helium gas at a pressure of 10^{-5} Torr is leaked into the FIM chamber, producing an image of the atomic structure of the tungsten tip (Figure 2.9) when a sufficiently large bias voltage is applied to the tip (between 5–20 kV). The field surrounding the tip apex region is so large that it can ionize the helium (though not large enough to ionize the tungsten itself), which is then projected along a well defined spatial path and collected at an imaging screen, providing up to a million times magnification [43]. The helium is ionized just above the tip atoms, but not in between them, giving the contrast necessary for atomic resolution.

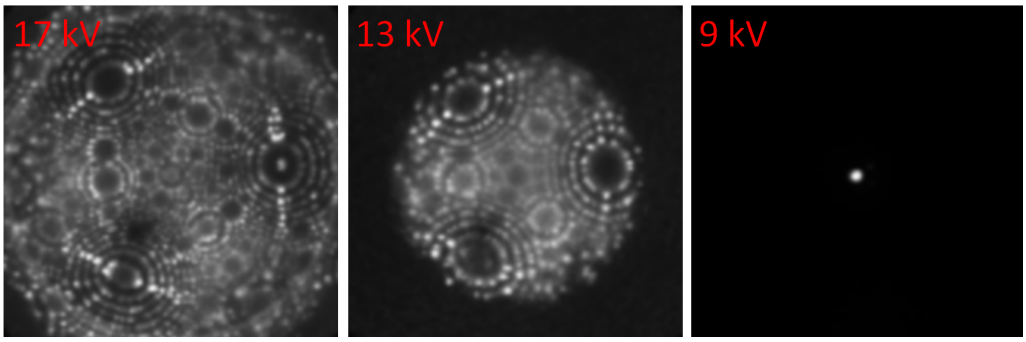

Figure 2.9: Field ion microscope images of a tungsten tip at various stages of the single atom sharpening process. The bright dots correspond to tungsten atoms. As the voltage applied to the tip is lowered sequentially during the etch more of the tungsten near the apex is able to be evaporated/etched away by the nitrogen gas present. The voltage is lowered until there is a single atom left at the apex of the tip.

In order to etch the tungsten wire, nitrogen gas is added into the FIM chamber at a pressure of 10^{-6} Torr. Nitrogen gas is able to reach the tungsten surface everywhere but in the highest field regions (tip apex) [38]. The nitrogen reacts spontaneously and dissociatively with the tungsten to form strong complexes that act as nano "lightning rods". The high fields at these locations cause the nitrogen-tungsten complexes to field evaporate from the surface, thus removing tungsten from the tip (etching it down) [38, 44]. By slowly lowering the applied bias voltage to protect sequentially less of the tip apex, tungsten can be removed approaching the end of the wire, creating a progressively sharper tip. Finally, when only the last atom is protected by the high fields from the nitrogen a single atom tip has been achieved (Figure 2.9) [38, 44]. At this point, all bias to the tip should be removed, and all gas valves closed. The single atom tip is now ready for use inside the STM.

2.4 Creation of a Dangling Bond (DB)

2.4.1 Initial Setup

In order to begin any STM experiments, the tip has to be brought towards the sample within a distance that allows for a measurable tunneling current to be detected. While it is not impossible to do manually, the risk of damaging the tip is very high so Nanonis (the STM control software and electronics) has a module to safely approach a tip. Before initializing this module though the tip is manually brought very close to the sample (approximately 1–3 mm away) with the coarse motion motors. The distance is determined by eye with an optical camera capturing images of the tip and sample together. When the tip is being manually approached, its reflection can be seen off of the polished silicon sample. The tip is moved in so that it is almost touching its own reflection. At this point, while the tip may appear to be close, it is still quite far from a tunneling distance (usually on the order of Angstroms). Now the Nanonis auto-approach module shown in figure 2.11 can be initialized. This module takes a number of coarse steps (number of pulses), which in this case is one, then uses the fine piezo positioning motors to travel through their full range (approximately 600 nm) attempting to sense for a measurable tunneling current. If none is detected, this process is repeated until the surface is reached. The approach can take anywhere from ten minutes to several hours.

Once the surface is reached the STM electronics attempt to maintain a user defined constant tunneling current (set-point) by modulating the tip-sample distance (z height). This modulation is the result of a feedback loop mechanism. The tunneling current is typically kept at a value between 30–50 pA. The feedback loop has two parameters that control its speed of response and sensitivity, the proportional and integral gains. Figure 2.10 shows typical settings for the feedback loop controls to achieve optimal image quality and tip stability.

Figure 2.10: The z height controller module of the Nanonis STM software. The feedback loop controls ensure the tip does not crash into the surface while scanning samples and producing images. The two parameters of the feedback loop, the proportional gain and integral gain are set here. The tunneling current set-point which the feedback loop attempts to maintain is also set here. Typical values are shown in here for optimal STM performance.

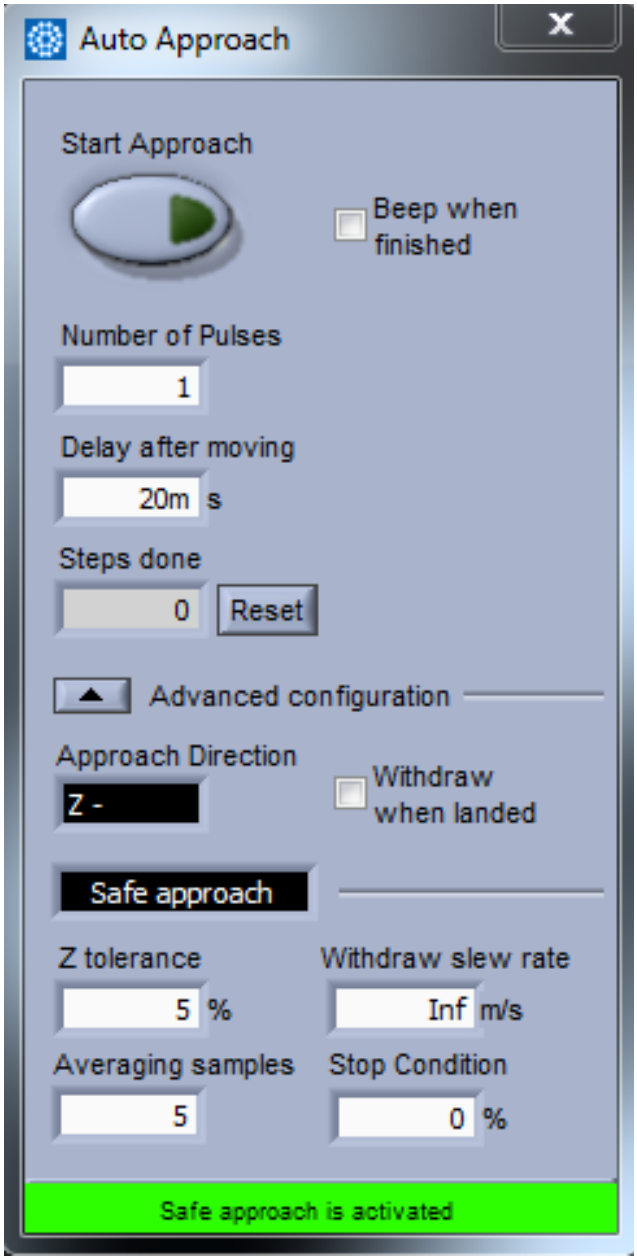

Figure 2.11: The Nanonis auto-approach module for safely bringing the tip within tunneling distance of the sample. The typical approach parameters are shown in the image. The number of pulses represents the number of coarse steps the tip can take each time. This number can be set between 1–2 steps safely.

2.4.2 Pulsing to Create a Dangling Bond

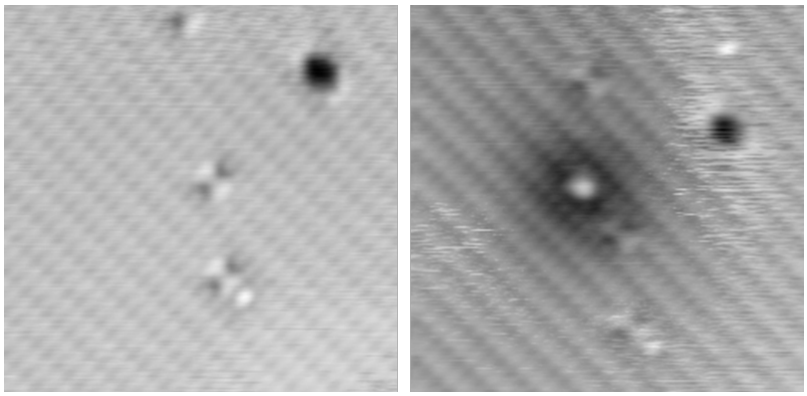

Figure 2.12: STM images at 1.40 V and a constant current of 30 pA of an area of hydrogen-terminated silicon before and after the creation of a DB. A voltage pulse of 2.3 V with a length of 10 ms was utilized. The black bow-tie structures are well known dihydride defects [45].

The procedure to make a single DB is straight forward. The STM tip is positioned over a hydrogen atom with the sample at a bias between -2 V to 1.6 V (generally). A voltage pulse with a value of 2.1–3.0 V is applied with a pulse length of 5–40 ms in order to break the H:Si bond and kick the hydrogen atom out. It is always recommended to start at the lower end of the voltage pulses, as larger voltages risk physically altering the tip structure. The bond breaking mechanism is generally believed to be repeated vibrational excitations of the H:Si bond through the electrons from the tip [46]. The Si:Si bond is chemically weaker than the H:Si bond, however, because there are three Si:Si bonds to break the hydrogen atom is removed [46–48].

Figure 2.12 shows an area before and after the creation of a DB. The bias pulses are set and implemented with the bias control box inside the Nanonis software. With the control box the pulse magnitude and duration can be set, and the pulse can be initialized with the pulse button. Figure 2.13 shows the bias control box with typical parameters to create a DB at 4 K.

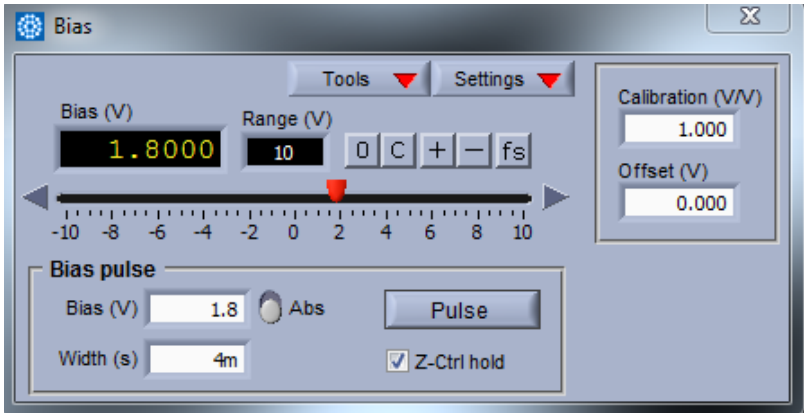

Figure 2.13: The bias pulse control box inside the Nanonis STM software. The pulse length and duration can be set, then the pulse can be created with the pulse button.

Chapter Three

Experimental Measurement of Telegraph Noise

The noise observed in the tunneling current near a DB has random telegraph-like characteristics [49]. There are sudden and random steps between discrete states within the tunneling current signal as illustrated in figure 4.1 associated with trapping and releasing of charges. Due to this similar behaviour to conventional telegraph noise [49,50] the noise measured and characterized in this thesis was termed telegraph noise as well.

3.1 Dangling Bonds, Halos, and Telegraph Noise

3.1.1 Dangling Bonds (DBs)

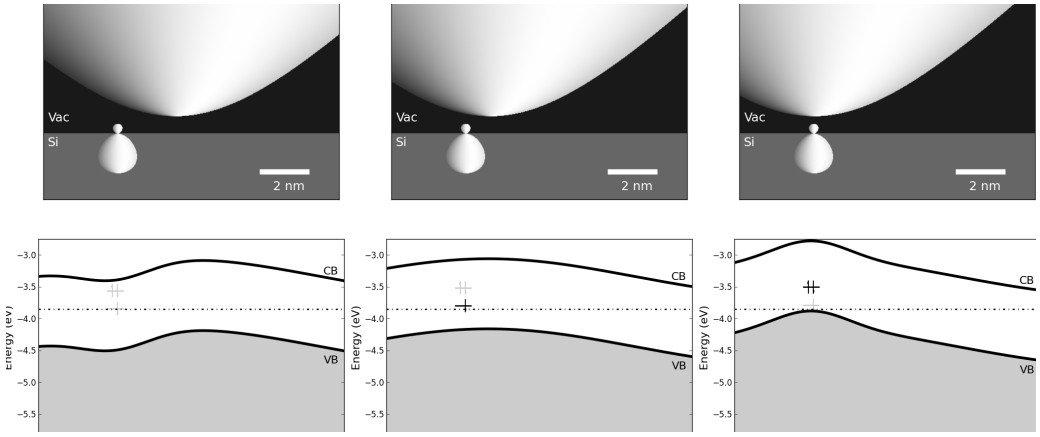

Figure 3.1: Three regimes of STM tip and dangling bond interactions. In the left panel the tip is too far to the right to inject charge, but it bends the bands near the DB, leaving the DB positive. In the middle panel the tip is near enough to the DB to inject some charge, and the band bending is more significant, leaving the DB neutral. In the right panel, the tip is close enough to inject charge faster than it can leave the DB, resulting in a net negative charge state.

A DB created on the surface of hydrogen-terminated silicon crystal (Section 2.4) is a lone sp^3 hybrid orbital of the underlying silicon atom that does not participate in bonding in an otherwise hydrogen-terminated region [5, 6, 8, 17] (Figure 1.2). It has a lobe both in the silicon bulk, and in vacuum as illustrated in figure 3.1. The DB creates a single surface state within the silicon band gap which can contain zero, one, or two electrons (Figure 3.1). These electronic occupations correspond to a positive, neutral, and negative charge state respectively [6, 8, 17]. Due to their ability to localize charge DBs can be considered as quantum dots, and are currently at the centre of many schemes for next generation devices [2, 15, 16, 25]. The energy of the DB gap-state above the valence band (VB) is not precisely known [17] and its energy varies with electron occupation. Estimates of the energy above the VB of the gap-state for a negative and neutral DB on the surface of n-type H:Si(100) 2×1

have been carried out by others [6, 17, 51–54]. It has been estimated that negative DB gap-state (containing two electrons) is ∼0.85 eV above the VB, and the neutral DB gap-state (containing one electron) is ∼0.35 eV above the VB [6, 17]. These energies are associated with transition levels $E_{\frac{=}{o}}$ and $E_{\frac{o}{+}}$ in conventional STM bias spectroscopy, where the charge state is determined by the position of the sample Fermi-level [6, 17]. If the Fermi-level is above a transition level then the DB will be in the associated charge state indicated above the slash in the subscript and if the Fermi-level is below the transition level the DB will be in the charge state indicated below the slash [17] (Figure 3.2). The positive DB gap-state does not have an associated energy in this context since it does not have a corresponding transition level and hence cannot be resolved by utilizing STM bias spectroscopy [6]. The ability to resolve three states with only two transition levels will be discussed in the following two sections.

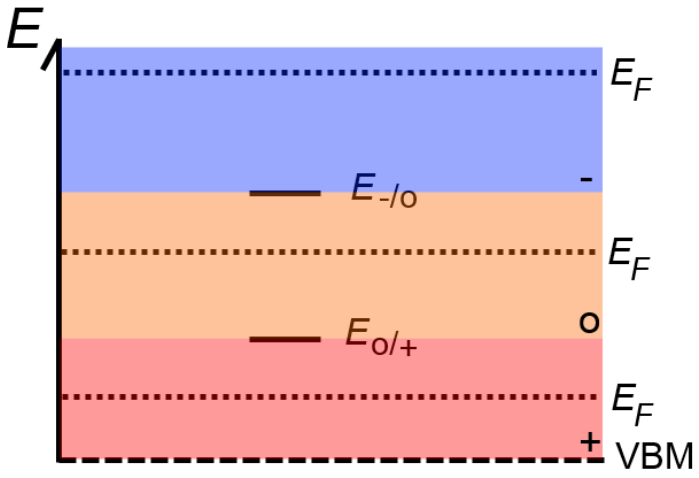

Figure 3.2: A graphical illustration of the transition levels above the valence band (VB) and the associated charge state of the DB when the relative position of the Fermi-level is changed. The DB is in a positive state (red) when the Fermi-level is below the first transition level. When the Fermi-level is above this level the DB is neutral (orange). Finally when the Fermi-level is above the second transition level the DB is negative (blue).

The position of the transition levels relative to the Fermi-level (and thus charge

state of the DB) can be altered by the electric field from the tip or trapped charges. These alterations are generally referred to as tip induced band bending (TIBB) and charge induced band bending (CIBB) respectively. Figure 3.3 shows estimated locations of the transitions levels, along with the calculations of the associated TIBB and CIBB for a neutral and negative DB [6, 17].

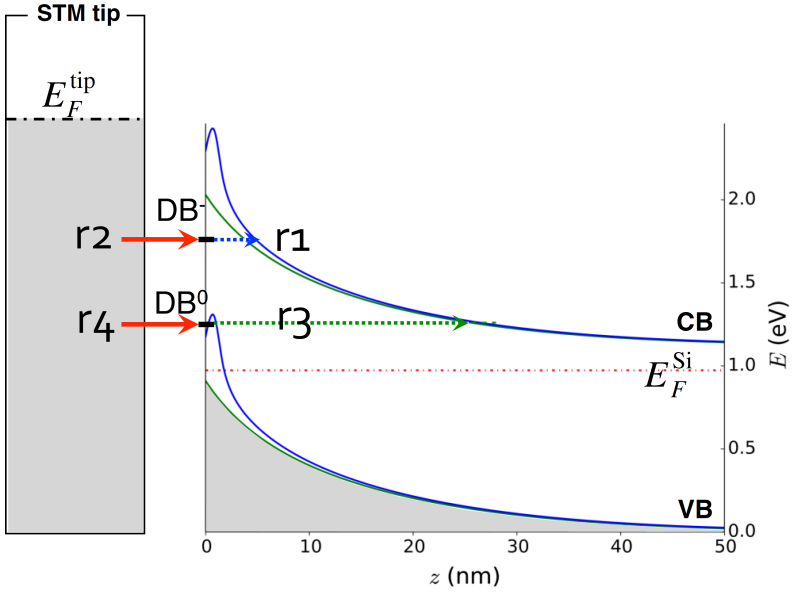

Figure 3.3: [6] This figure depicts the DB energy levels associated with each charge state, and the corresponding rates (scheme 5.1). The filling and emptying mechanisms are indicated by the rates with arrows. The TIBB and CIBB associated with each charge state is shown in solid green for a neutral DB and solid blue for a negative DB.

3.1.2 The Halo

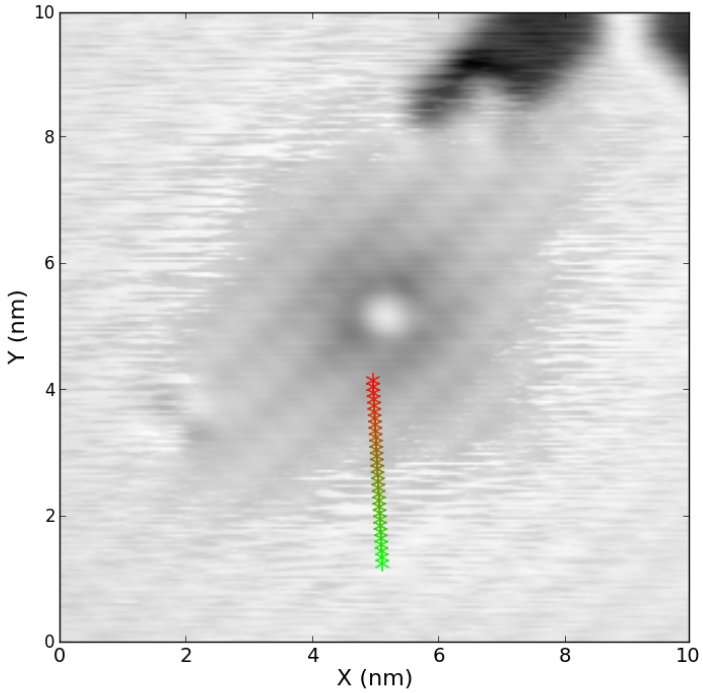

Figure 3.4: STM image of a DB taken at 1.40 V and constant current of 30 pA with a very clear halo region surrounding the bright DB centre. The random speckles of bright and dark at the halo edge are due to the fluctuation in charge state of the DB driven through influence of the STM tip. The size of this halo decreases with increasing bias voltage.

Dangling Bonds when imaged at certain bias conditions exhibit a dark halo region surrounding the DB centre. This halo tends to only appear at empty-state sample bias conditions (sample bias voltage above zero), and has been observed at both room temperature and cryogenic temperatures [5, 8, 17, 55] alike. The size of the halo can vary dramatically with bias conditions, with the halo size decreasing with increasing bias voltage. At sufficiently high bias voltages (usually above 2.0 V) the halo region can vanish entirely. The physical geometry of the STM tip can also influence the

size and shape of the halo (as discussed in Section 5.4.2).

The halo is postulated to be the result of non-equilibrium charging effects induced by the presence of the STM tip [8, 17], which force the DB to be negative. At close radial tip-DB separations the TIBB is strong enough to bend the energy bands of the silicon in such a way that the DB gap-state is above the Fermi-level [6, 8, 17] (Figures 3.1, 3.3). Normally this would result in a positive DB since its state is unoccupied due to its position relative to the Fermi-level. However, charge is also able to enter the DB through tunneling events from the tip. Within a certain region of radial tip-DB separation (the halo) the tunneling events from the tip into the DB are so frequent that the level is always filled, giving it a net negative charge. These tunneling events cause negligible current when compared to the tip-sample tunneling current, so the DB is not the current carrying state in these discussions (Figure 3.5). The best analogy for a negative DB in this scenario is to consider it as a bucket with a hole in the bottom being filled by a tap. If the flow of the tap is fast enough, the bucket will remain full despite it constantly losing water.

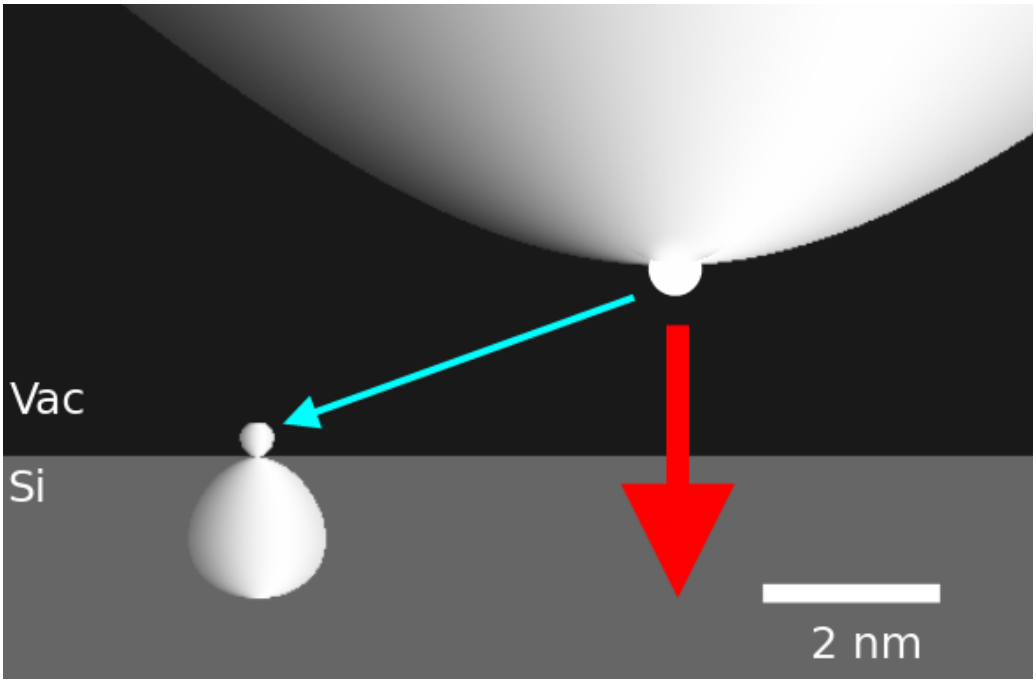

Figure 3.5: The tunneling current from the tip to the DB (blue) is negligible when compared to the main tip to sample tunneling current (red) that is recorded and measured.

The halo region appears dark because the negative charge of the DB is gating the main tip-sample tunneling current [6, 17, 56, 57]. The upward band bending caused by the negative DB reduces the local density of states (LDOS) available for electrons to enter from the tip. This reduction in LDOS causes a reduction in tunneling current [56], which manifests in the image as a dark region.

3.1.3 Three Charge States

The location of the Fermi-level as shown in figure 3.2 and described in the previous two sections is directly related to the ability of the DB to exist in multiple charge states. In the case of the degenerately doped n-type silicon used in these experiments, the Fermi-level is within the conduction band [58]. With the level so high it might be expected that the DB should always be negative making it impossible to exist

in, and subsequently detect the other two states. It is known, though, that the repetitive heating of the sample during surface preparation actually causes dopants to be depleted near the surface [59]. Within this dopant depleted region the Fermi-level is lower than its original pre-prepared position. With a lower Fermi-level (similar to the one shown in figure 3.3) it is possible to observe all three charge states with appropriate band bending conditions.

In figure 3.1 three radial tip-DB separations and the qualitative band bending associated with each charge state are shown. At distances too far for electrons to tunnel from the tip to DB, but where the TIBB can raise the DB level above the Fermi-level the DB is in its positive charge state. Positive charge causes downward band bending, which actually increases the LDOS near the surface of the sample for electrons to tunnel into through a similar gating mechanism to the negative state. The increased LDOS shows up as an increase in the tip-sample tunnelling current and causes the region outside the halo to appear bright [8,17]. When the tip moves in further, tunneling events are now possible and the DB can exist in the neutral state. Since the neutral state has no net charge there is no associated CIBB and as a result no increase or decrease in the brightness of the STM image. When the tip is moved radially closer still to the DB centre the negatively charged DB described in section 3.1.2 causes upward band bending, and reduces the observed tunnelling current. The reduction in tunneling current appears in the STM image as dark features.

At the halo edge in figure 3.4 the telegraph noise resulting from the fluctuation of the DB between charge states shows speckles of bright, neutral, and dark regions corresponding to the positive, neutral, and negative charge states. Since the presence of single electrons cause such pronounced gating effects (similar to those in a Field Effect Transistor) the tunnelling current acts as a sensitive charge detector [6]. When this telegraph noise is recorded, the discrete jumps in the current due to the different gating conditions from the DB are direct indications of single electron movements.

3.2 Collection of Telegraph Noise

3.2.1 Procedure

The collection of telegraph noise required a standardized procedure to ensure all datasets were collected in an identical manner. The procedure was implemented using the Nanonis software suite along with its LabView interface. The basic schematic of the telegraph measurements is as follows:

1. The tip is fixed at a constant height based on the current scanning parameters in a region without telegraph noise.
2. The tip is placed within a region of interest where telegraph noise can be observed in an STM image.
3. The tip-sample tunneling current is recorded for a fixed duration of time at a fixed sampling frequency.

In order to record the telegraph noise at fixed radial distances from the DB centre the bias spectroscopy function inside Nanonis was utilized, though not for its intended purpose. By setting the number of points, and the sweep time accordingly (as shown in figure 3.6) the maximum sample rate possible with the equipment was achieved (in our case 10 kHz). In typical bias spectroscopy the sample bias is swept over a range of values, however for a telegraph experiment the bias needs to remain constant. In order to ensure this, the start and end biases were set to matching values according to the desired bias for the experiment (also shown in figure 3.6).

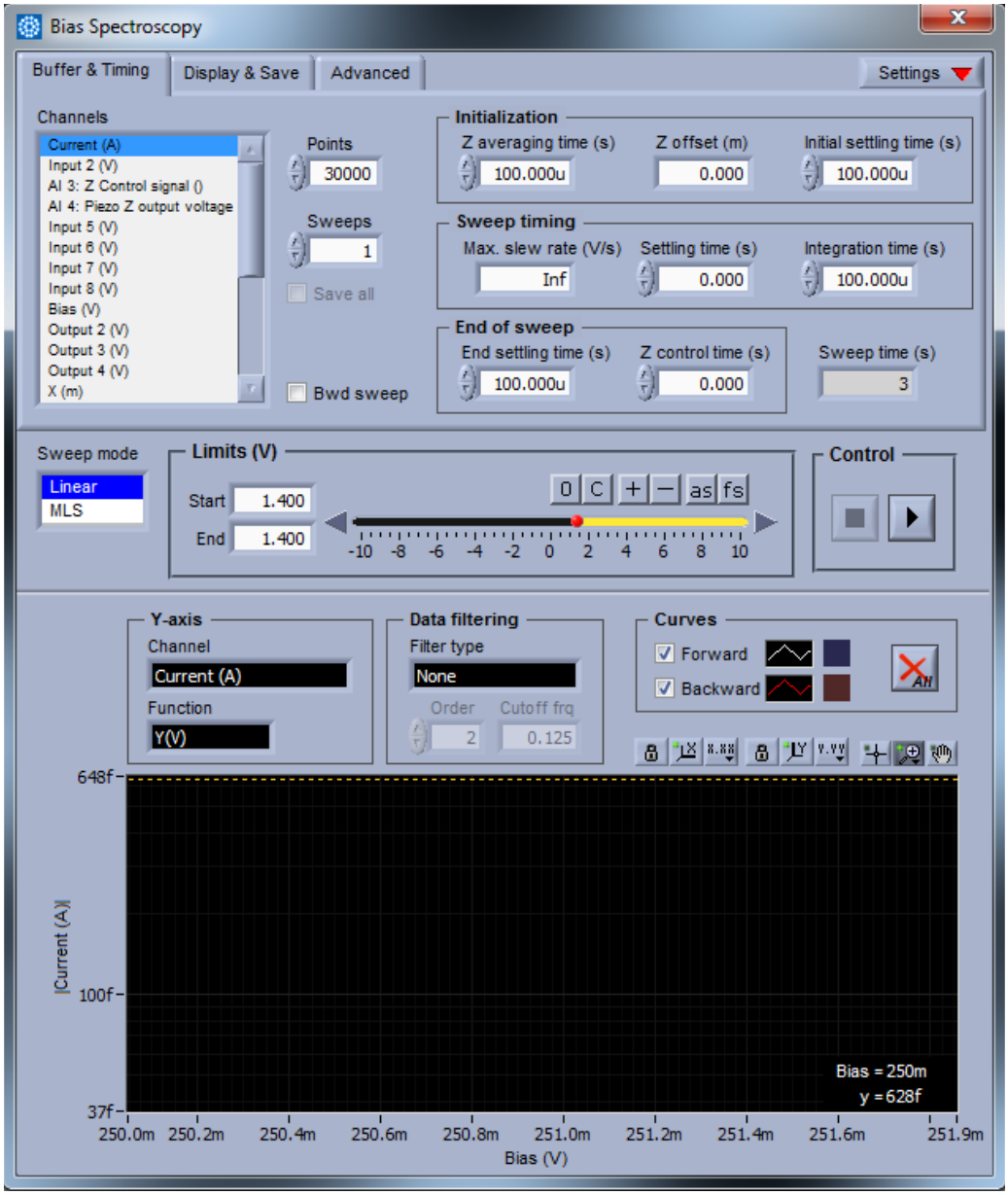

Figure 3.6: The Nanonis bias spectroscopy window with typical settings to allow it to be used for telegraph data acquisition. The number of points was set to 30000, and the sweep time was set to 3 s, giving a 10 kHz sampling rate. The limits of the bias voltage to sweep over were set to identical values, giving a constant bias over the length of the experiment.

Once these values were set, the grid-spectroscopy function inside Nanonis was utilized to designate points in the STM image where telegraph noise would be recorded. Figure 3.7 shows an STM image of a DB and the locations of the telegraph measurements where the basic schematic above was performed. The length of the line, and its position can be varied within the program. In general between 20–30 points per line were recorded. The radial distances could then be calculated from the location of the DB centre in the image, and from the recorded x-y coordinates of the experiment locations.

In order to ensure that there is minimal drift (thermal) or creep (from moving the tip) away from these points in figure 3.7 during a measurement (which can take up to 15 minutes) the STM is usually left to stabilize for 4–8 hours before the experiment is started once a DB of interest is located and imaged.

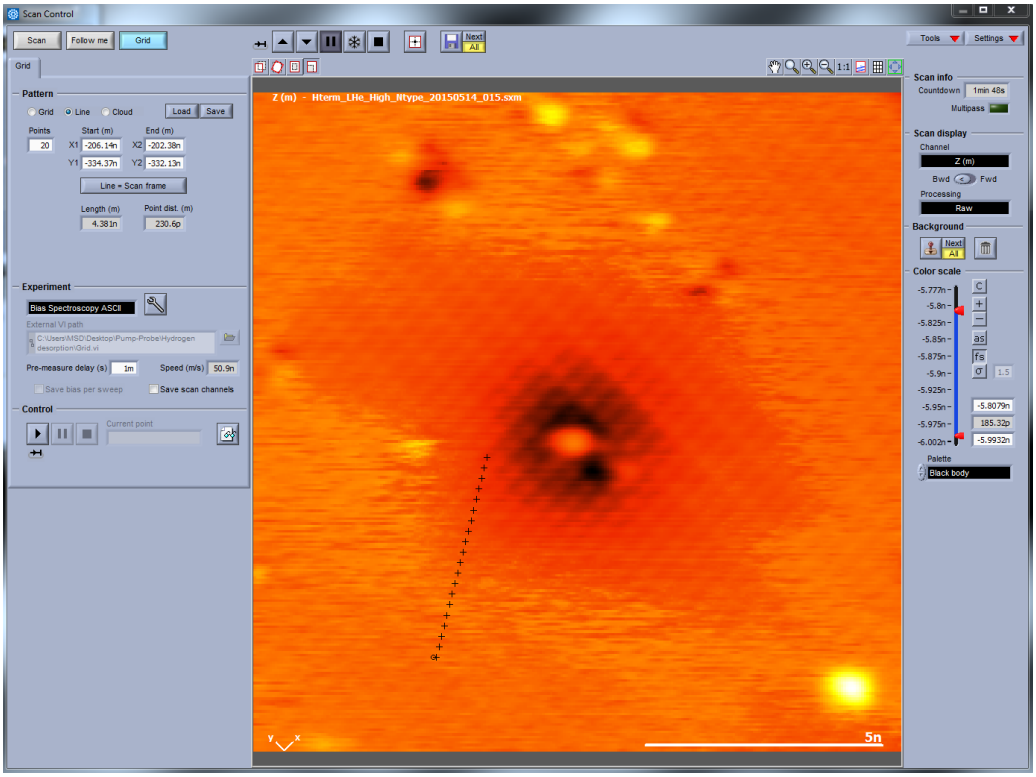

Figure 3.7: The grid-spectroscopy window inside Nanonis. The points where telegraph data are to be acquired are indicated with black x's in the image. This line can be varied in position and length within the program. The number of points in the line can also be set. Typical values for the telegraph experiments were 20–30 points in a line.

3.2.2 Other Considerations

Beyond thermal stability and bias parameters for a telegraph measurement, the tip-sample tunnelling current set-point is a crucial parameter for obtaining the best telegraph measurements. The set-point determines the relative tip-sample separation distance (how close the tip is to the surface). Based on this set-point the amount of environmental noise (undesired) in the experiment can vary greatly. It was found that in general for the best telegraph measurements a set-point of approximately 30 pA was ideal.

The noise in the tunneling current is not constant between all choices of set-points. There is more noise in the signal for instance at 50 pA than 30 pA. The tunneling current between an STM tip and sample can generally be described by an exponential relationship with the tip-sample distance z [23]:

$$I(z) \propto e^{\frac{-2\sqrt{2m\phi}z}{\hbar}}, \tag{3.1}$$

where m is the mass of the electron, ϕ is the average work function between the tip and sample, z is the tip sample distance, and $\hbar$ is the reduced Planck constant. The two main sources of noise in the measured current are the noise in the pre-amplifier (δI_{amp}), and the noise in z height of the tip caused by vibrations (δz). Both of these noise sources can be considered constant [60], and in the case of the pre-amplifier noise reasonably small (Section 2.1.2). However, while the displacement of the tip up and down is a constant, the resulting current noise (δI_z) varies with the magnitude of the tunnelling current. Figure 3.8 shows the region of δz and the resulting region δI_z. δI_z in this figure is given by:

$$\delta I_z(z_o) = I\left(z_o - \frac{\delta z}{2}\right) - I\left(z_o + \frac{\delta z}{2}\right). \tag{3.2}$$

Using equation 3.1, equation 3.2 can be written as:

$$\delta I_z(z_o) \propto e^{\frac{-2\sqrt{2m\phi}(z_o - \frac{\delta z}{2})}{\hbar}} - e^{\frac{-2\sqrt{2m\phi}(z_o + \frac{\delta z}{2})}{\hbar}}, \tag{3.3}$$

$$\propto Ae^{\frac{-2\sqrt{2m\phi}z_o}{\hbar}} - Be^{\frac{-2\sqrt{2m\phi}z_o}{\hbar}}, \tag{3.4}$$

$$\propto (A-B)e^{\frac{-2\sqrt{2m\phi}z_o}{\hbar}}, \tag{3.5}$$

$$\Rightarrow \delta I_z(z_o) \propto I(z_o)\ , \tag{3.6}$$

where A and B are constants. So according to equation 3.6 the noise in the current δI_z is directly proportional to the set-point I. This has been experimentally verified as well. The experiment was performed by finding a clean area of hydrogen-terminated silicon with no nearby defects, setting the bias-voltage at a fixed value,

then recording time-traces of current at a fixed location with differing tip-heights to change the measured tunnelling current (set-point). The time-traces produce Gaussian distributions of current centred around the set-point/tunnelling current value (Figure 3.9). These distributions were fit and the standard deviation (σI) of the Gaussian functions (corresponding to δI_z) were plotted as a function of current set-point, as shown in figure 3.10.

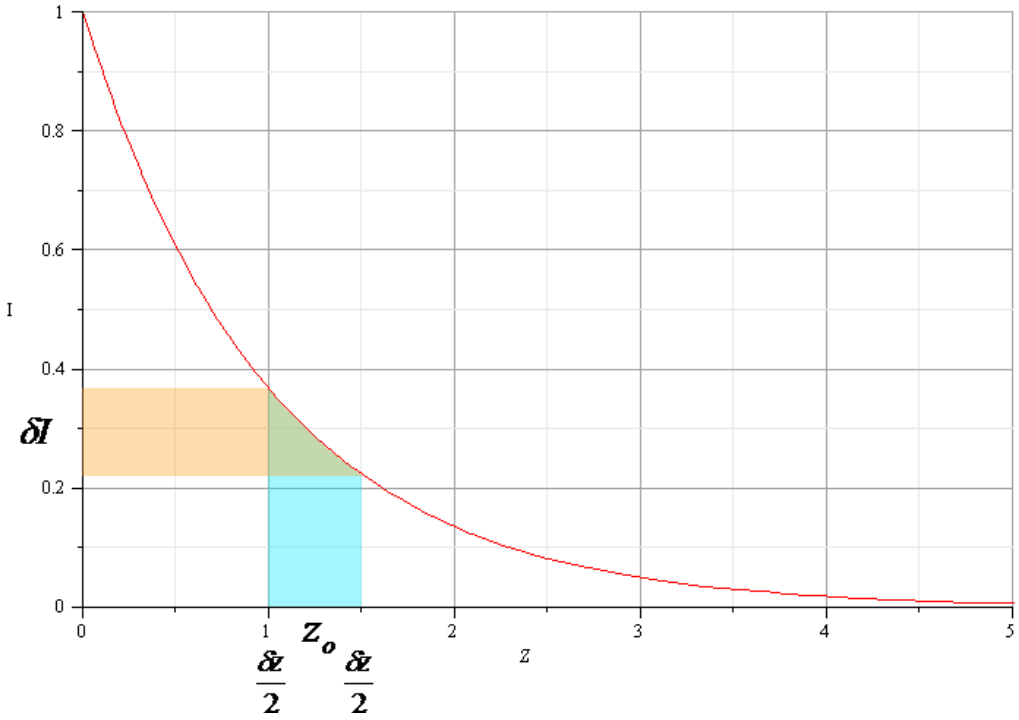

Figure 3.8: An example of the current distance relationship between an STM tip and sample. Both axes are in arbitrary units. The noise in z height (δz) is constant, however the resulting current noise (δI) varies with the tunnelling current.

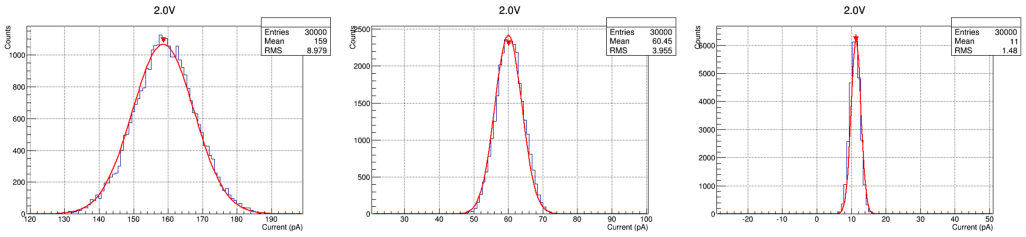

Figure 3.9: A series of time-traces of tunnelling current recorded over hydrogen-terminated silicon at various tunnelling current set-points. The width of the Gaussian distributions decrease with current set-point.

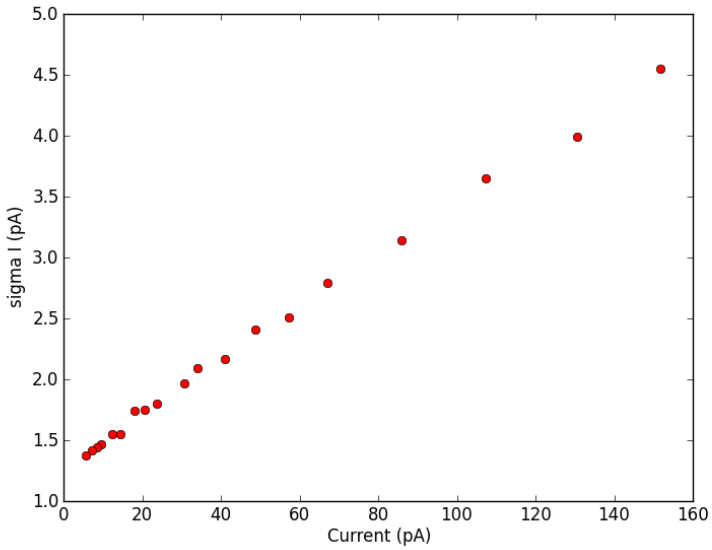

Figure 3.10: The standard deviation of the Gaussian fits shown in figure 3.9 plotted as a function of tunnelling current. It can be seen that there is a linear increase in current noise as the tunnelling current is increased.

Chapter Four

Basic "Toy" Model of DB Occupation Probabilities

4.1 Simple Model

When the telegraph-like fluctuations in the STM tunneling current were first observed at the halo edge of a DB (Figure 4.1) utilizing the methods described in section 3.2, it appeared as if there were three distinct regions in these data where the current tended to plateau.

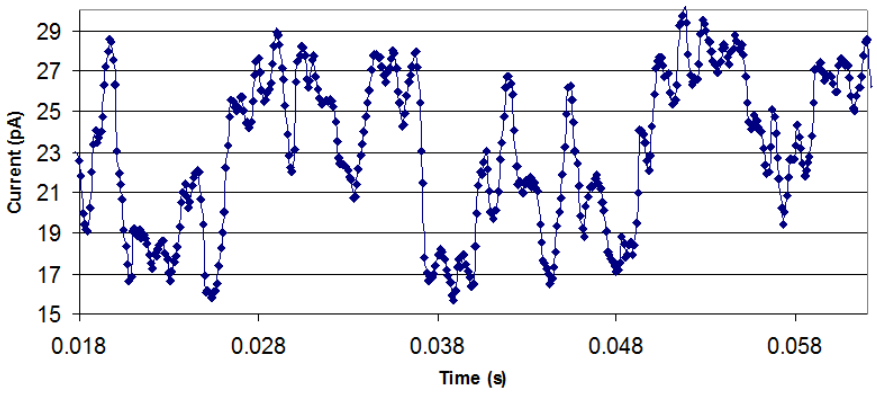

Figure 4.1: A snippet of a current vs time telegraph time-trace taken at the halo edge of a DB. Within these data points are three regions where the tunneling current tends to plateau.

The telegraph time-traces were converted into 1D histograms (Figure 4.2) and indeed many of the datasets exhibited three distinct peaks.

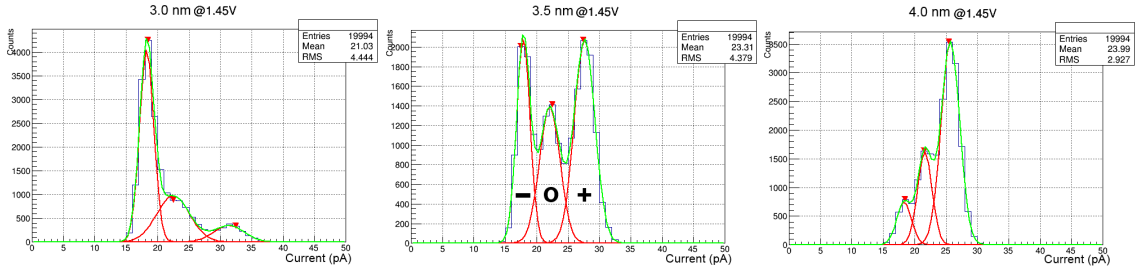

Figure 4.2: A series of histograms created from current vs time time-traces taken at various radial distances from a DB centre at a sample bias of 1.45 V and current of 30 pA. As the radial tip position is varied, the occupation of each state changes as well. The peak centred around the lowest current value represents the negative state, the next peak is the neutral state. The peak at the highest current value is the positive state. The histograms were fit with three Gaussian functions simultaneously.

The three peaks were attributed to three unique charge states of the DB: DB^{+}, DB^{o}, DB^{-}, when the DB contains zero, one, and two electrons respectively. The normalized area under each peak gives the steady-state probability of finding the DB in that particular charge state. It is important to note that the system (DB, tip, and sample) is in a steady-state, and not in equilibrium [17,61]. That is, if the STM tip were to be removed, the observed dynamics would also cease since electrons are no longer injected into the DB from the tip. The consequences of this are discussed further in section 5.2.2.

4.1.1 Basic Assumptions

As a first step towards describing the major dynamics of the system from these histograms, a simple model was developed which captured the essence of the non-equilibrium charging theory of DBs put forth by Livadaru, et al. [17]. This simple model doesn't make a distinction between the various filling and emptying processes described in [17]. Instead, the model assumes there is a constant intrinsic emptying rate from the DB (regardless of charge state) of electrons into the bulk silicon given by E. The model also assumes there is a state-independent filling rate F (Equation 4.1) of electrons into the DB that is dependent on an intrinsic filling rate F_0, the

radial distance of the DB from the STM tip d, and an arbitrary parameter γ that is related in some way to the overall geometry of the STM tip. The exponential form was chosen because tunneling is known to decay exponentially with distance [23].

$$F = F_0 e^{-\gamma d}. \tag{4.1}$$

Another important assumption in the model is that there is only a linear charging pathway to travel between states. That is, there is no direct charging pathway between the negative (DB^-) and positive (DB^+) states. The linear scheme is given by:

$$DB^- \underset{F}{\overset{E}{\rightleftharpoons}} DB^o \underset{F}{\overset{E}{\rightleftharpoons}} DB^+ \quad . \tag{4.2}$$

4.1.2 Creation of 1D Histograms

In order to simplify the process of creating histograms for datasets consisting of many measurements, a batch processing algorithm was created utilizing the python programming language along with the ROOT package from CERN, and numpy package [62–66] (all freely available). This algorithm reads in the .dat files generated during the data collection process described in section 3.2, then utilizes the peak-finding module in the ROOT package to identify prominent peaks in each histogram. This peak identification process helps filter these data so only those with three resolvable peaks can be used in analysis. The decision was made to limit these data to those with three resolvable peaks because identifying peaks buried within one another automatically is a current computational challenge. In addition to this, because of the atomic corrugation of the hydrogen-terminated surface, the mean of each histogram shifts with position depending on whether the tip is centred on an atom or in-between atoms (Figure 4.3), making it very difficult to predict where a state should be located if it is not already resolvable.

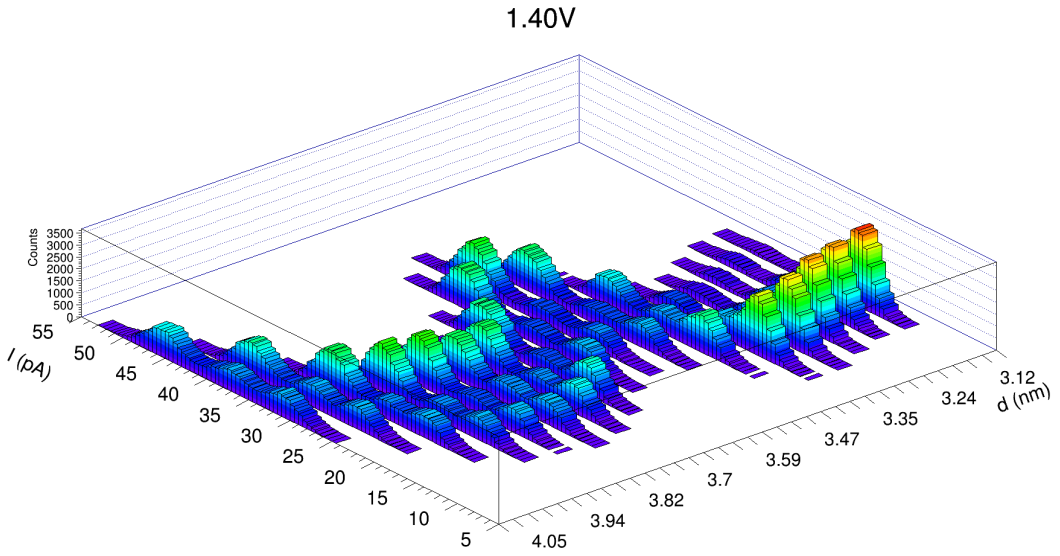

Figure 4.3: A 3D representation of the 1D histograms at various radial distances from a DB centre. The mean of each histogram is shifted due to the atomic corrugation of the hydrogen-terminated surface.

4.1.3 Derivation

When the histograms of these telegraph data were viewed in order of decreasing radial distance to the DB, it was noted that the negative peak became larger, while the other two peaks diminished in size. In order to quantitatively view this trend, Gaussian curves were fit to each state in all datasets that had three easily resolved peaks (Figure 4.2), and the area of each curve was extracted. This area was then normalized by the total number of points in the histogram to give the steady-state probability of each state. These probabilities were then plotted as a function of radial distance (Figure 4.4), showing an interesting sigmoidal trend. In order to fit these curves, a set of equations were created according to the reaction scheme 4.2 to describe the probabilities as a function of radial distance.

For a given state i the steady-state probability is given by:

$$P_{i_{ss}} = \frac{[\,i\,]}{[+] + [-] + [o]}, \tag{4.3}$$

where $[\,i\,]$ is the fraction of points in a given state. At steady-state $\frac{d[\,i\,]}{dt} = 0$ a set of master equations for the scheme 4.2 can be written based on the filling and emptying rates [67],

$$\frac{d[-]}{dt} = F \cdot [o] - E \cdot [-] = 0, \tag{4.4}$$

$$\frac{d[+]}{dt} = E \cdot [o] - F \cdot [+] = 0, \tag{4.5}$$

$$\Rightarrow \frac{E}{F} = \frac{[o]}{[-]} = \frac{[+]}{[o]}. \tag{4.6}$$

Defining $K \equiv \frac{E}{F}$ gives,

$$[+] = K \cdot [o], \tag{4.7}$$

$$[-] = \frac{[o]}{K}. \tag{4.8}$$

Now using the equations 4.7 and 4.8 in equation 4.3 for the positive state as an illustration,

$$P_{+_{ss}} = \frac{[+]}{[+] + [-] + [o]}, \tag{4.9}$$

$$= \frac{K \cdot [o]}{K \cdot [o] + \frac{[o]}{K} + [o]}, \tag{4.10}$$

$$= \frac{K \cdot [o]}{K \cdot [o] + \frac{[o]}{K} + [o]}, \tag{4.11}$$

$$= \frac{K}{K + \frac{1}{K} + 1}, \tag{4.12}$$

$$= \frac{1}{1 + \frac{1}{K^2} + \frac{1}{K}}. \tag{4.13}$$

From here, equation 4.1 can be substituted into equation 4.13 giving:

$$P_{+_{ss}} = \frac{1}{1 + \left(\frac{\frac{1}{E}}{F_0 e^{-\gamma d}}\right)^2 + \frac{\frac{1}{E}}{F_0 e^{-\gamma d}}}, \tag{4.14}$$

$$P_{+_{ss}} = \frac{1}{1 + \frac{e^{-2\gamma d}}{Q^2} + \frac{e^{-\gamma d}}{Q}}, \tag{4.15}$$

defining $Q \equiv \frac{E}{F_0}$. Following the same procedure for the negative and neutral states, the following equations are obtained:

$$P_{-_{ss}} = \frac{e^{-2\gamma d}}{Q^2 + Q e^{-\gamma d} + e^{-2\gamma d}}, \tag{4.16}$$

$$P_{o_{ss}} = \frac{e^{-\gamma d}}{Q + e^{-\gamma d} + \frac{e^{-2\gamma d}}{Q}}, \tag{4.17}$$

4.2 Fitting the Model to Data

4.2.1 Simultaneous Curve Fitting

The model equations for the probability of being in each state as a function of radial tip distance (Equation 4.15, 4.16, 4.17) have two free parameters Q and γ. Both of the parameters were expected to be constant (as a function of radial tip distance) since Q is defined as the ratio between the intrinsic emptying and filling rates E and F_0 ($Q \equiv \frac{E}{F_0}$) in the model, and γ is a constant related to the specific geometry of the tip.

There were several different possible options to fit the model equations to these state-probability data (Figure 4.4). The first option, which was easiest, but also the least desirable was to fit each equation to each curve individually and obtain three separate values for Q and γ. This option was the least desirable because it didn't represent the assumptions in the model that Q and γ are the same in each equation, leaving the possibility for differences between the parameters for each state (arising from limitations in the fitting algorithms, errors, different physical processes etc...). The second option was to fit all three equations simultaneously to their respective curves by finding an optimal value of the parameters based on the three states. There were no fitting routines readily available for simultaneous curve fitting, so one had to be implemented manually.

Utilizing the python programming language [62] along with the scipy, numpy, and ROOT packages [63, 64] a least squares optimization routine was created to fit all three of the model equations simultaneously. The routine works by calculating values for each model equation with varying values of Q and γ, then attempting to minimize the differences between these calculated values and real data values until a minima is achieved [64]. The result of the minimization can be seen in figure 4.4, giving values of $Q = 0.0058$ and $\gamma = 1.7$ (1/nm) respectively.

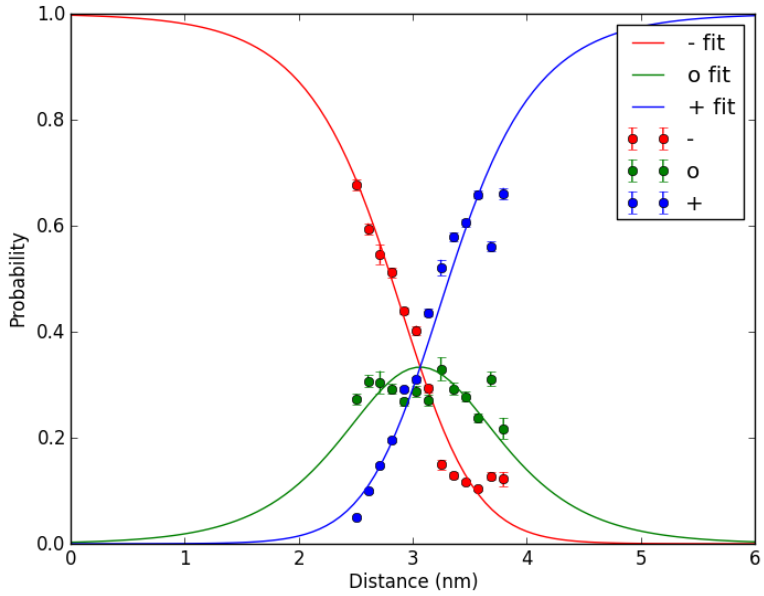

Figure 4.4: The area of each Gaussian curve fit to the histograms of telegraph data (Figure 4.2) normalized by the total number of points in the dataset, as a function of radial tip distance. The fits utilizing the fitting functions (Equations 4.15, 4.16, 4.17) are shown with solid lines. The curves were all simultaneously fit to produce only two values for the fitting parameters Q and γ.

4.2.2 Bootstrapping to Estimate Parameter Space

In order to estimate the errors of Q and γ, and visualize their likely parameter space, a bootstrapping analysis was implemented. Bootstrapping involves sampling an original dataset randomly with replacement [68,69] in order to generate many new datasets with slight variations. These new datasets can be representative of possible statistical fluctuations if an experiment were to be repeated over several trials. Again, using python, numpy, scipy, and ROOT a bootstrapping algorithm was implemented in order to generate one thousand datasets from the original dataset. The process of extracting areas and fitting the probability functions described in sections 4.1.3 and 4.2.1 was repeated for each set of bootstrapped data, generating a space of 1000 values for Q and γ. The results of the bootstrapping can be seen in figure 4.5.

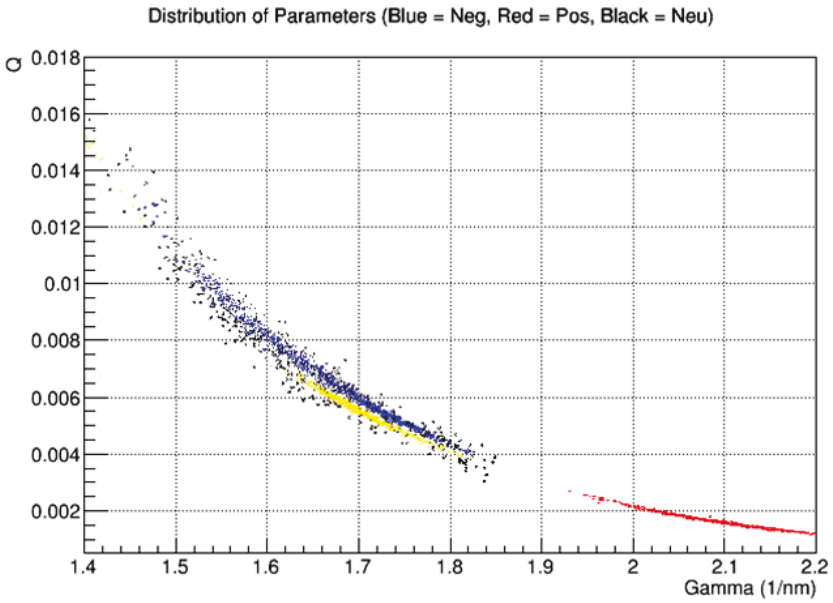

Figure 4.5: The parameter space created for Q and γ through analysis of 1000 bootstrapping simulations. The yellow curve is the parameter space when all the curves are fit simultaneously as in figure 4.4. The other regions are the parameter spaces created for Q and γ when each curve is fit individually to its respective fitting function. Blue is from the negative state, red is the positive state, and black is the neutral state.

4.3 Results and Discussion

4.3.1 The values of Q and γ

Figure 4.5 shows the parameter space of Q and γ in yellow, when all three model functions were simultaneously fit. It is a narrow distribution, which also appears to show an anti-correlation between Q and γ. The larger γ becomes, the more quickly the exponential filling rate (Equation 4.1) would decay, however, the resulting change in Q appears to be minimal for larger changes in γ. Factoring in the width of the distributions, for this dataset it was found that $Q = 0.0058 \pm 0.0004$ and $\gamma = 1.7 \pm 0.06$ (1/nm). The small value for Q gives an insight that the difference

between the rate of filling and emptying processes is quite large since it is a ratio of the assumed intrinsic emptying and filling rates. Figure 4.5 also shows the parameter space of Q and γ when all three curves were fit individually. It can be seen that there is a significantly wider spread in possible values (giving larger error bars), and that the space of parameters from fitting the positive function does not overlap with those of the other two states. This could indicate that the model assumption that Q and γ are identical for each state is incorrect.

4.3.2 Limitations of the Model and Method

While this model and method have worked better than originally anticipated, there are many limitations that prevent it from being quantitatively useful. The results of the method only give two parameters based on very simple assumptions. Neither of these parameters actually give any specific emptying or filling rates between states, and thus make it difficult to draw any substantial conclusions from their values. With these issues in mind, it was decided that different analysis techniques should be pursued in lieu of this simple analysis. As a result, only one dataset was subjected to this initial analysis.

4.3.3 Extensions and Further Work

Despite its shortcomings this model and method of analysis helped lay the ground work for the more detailed analysis to follow. Because the model worked better than expected, it gave support to some of the assumptions such as the linear charging pathway 4.2 and an exponential form of the filling rate equation 4.1, guiding the next steps. In addition, while the Q parameter did not provide any specific information, the γ parameter holds potential to describe the sharpness of the tip since it is likely related to the physical geometry of the tip. With the larger body of data now available, values of γ can be generated using this analysis from different tips. It may be possible to correlate the values of γ obtained with the imaging quality of a given tip. If there is a correlation, this method may provide a quick and dirty way to characterize the sharpness of a tip before, during, and after certain experiments

with a DB to help identify if the tip has undergone a microscopic change as a result of the experiment.

Chapter Five

Quantitative Methods for Analysis of Telegraph Noise

5.1 Method 1: Single State Dynamic Method

The method described here was implemented and utilized by Taucer, et al. [6,60] to analyse the same telegraph dataset discussed in the previous chapter (Chapter 4). It is a variant of a biophysical method developed by Hoffmann, et al. [18], initially developed to determine the specific rates of protein folding/unfolding. While the system at hand is physically very different than the wet world of proteins, the form of these telegraph data is actually quite similar. In both cases, a simple thresholding technique is insufficient to determine the transition rates between states. This is because the separation between the states is on the same order of the noise in the measurements, making it very subjective to determine where the thresholds should be set.

The actual implementation of this method was completed by Marco Taucer [6] in collaboration with myself and the Woodside group at the University of Alberta. As such it is not a very large portion of this thesis. However, it is worth outlining the method for comparison to the method implemented for analysis in this project (Section 5.2). It also allows for the addition of some details in the derivation that make the method more clear.

5.1.1 Outline of Method

The basic premise of this method is that a collection of points (in orange) in the overall histogram of a time-trace (in grey) (Figure 5.1) are selected from a given state. The values of these selected points are then tracked at each subsequent time-step from their original position. At each time-step the points move to a different value, and thus create a new distribution (histogram) as shown figure 5.1. This new distribution is then fit with Gaussian functions to each state to extract the probability of being in that state (Figure 5.2). This is an identical fitting process to the one first implemented in the simple model (Figure 4.4). The curves show an eventual decay to the steady-state probabilities given by the fits of each state in the overall grey histogram. In order to determine the rates between states fitting functions had to be created for each of these curves in figure 5.2.

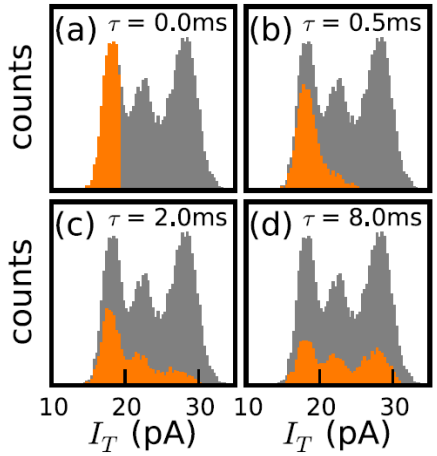

Figure 5.1: [6] The overall histogram of an entire time-trace is shown in grey. A subset of these data points in the negative charge state are selected in orange. As time moves forward the selection of points transitions into the other states, and their distribution eventually approaches a scaled down version of the overall histogram.

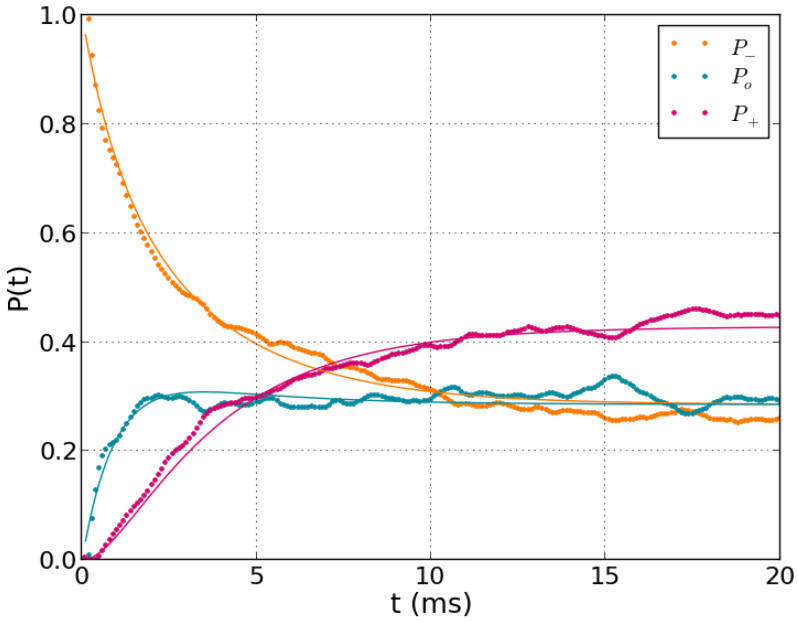

Figure 5.2: The probabilities of each state approaching their steady-state values as the system is let to evolve away from the initial selection of points (Figure 5.1). The probabilities of each state are generated from the normalized area of the Gaussian curves fit to the newly generated distributions at each time t. The values of each curve approach the probability of the corresponding peak in the overall histogram in figure 5.1.

5.1.2 Derivation

In order to create the fitting functions, the assumption that the charging follows a linear pathway still had to be maintained. However, instead of making any assumptions about the filling and emptying rates, along with their form, the rates are left as free parameters.

$$\mathrm{DB}^- \underset{r_2}{\overset{r_1}{\rightleftharpoons}} \mathrm{DB}^\mathrm{o} \underset{r_4}{\overset{r_3}{\rightleftharpoons}} \mathrm{DB}^+ \quad . \tag{5.1}$$

From scheme 5.1 a set of steady-state master equations can be written down in the same way they were in section 4.1.3 [67]:

$$\frac{d[-]}{dt} = r_2[o] - r_1[-] = 0, \tag{5.2}$$
$$\frac{d[o]}{dt} = r_1[-] + r_4[+] - r_2[o] - r_3[o] = 0, \tag{5.3}$$
$$\frac{d[+]}{dt} = r_3[o] - r_4[+] = 0. \tag{5.4}$$

Using matrix formalisms, the following matrices can be defined from equations 5.2–5.4:

$$\mathbf{C} = \begin{bmatrix} [-] \\ [o] \\ [+] \end{bmatrix}, \tag{5.5}$$

$$\mathbf{K} = \begin{bmatrix} -r_1 & r_2 & 0 \\ r_1 & -(r_2 + r_3) & r_4 \\ 0 & r_3 & -r_4 \end{bmatrix}, \tag{5.6}$$

allowing equations 5.2–5.4 to be written in the simplified form:

$$\frac{d\mathbf{C}}{dt} = \mathbf{K}\mathbf{C}. \tag{5.7}$$

Integrating equation 5.7 with respect to time gives:

$$\mathbf{C}(t) = e^{\mathbf{K}t}\mathbf{C}_o, \tag{5.8}$$

where $\mathbf{C}_o$ is the initial population of the system at $t = 0$. Using the identity

$$e^{\mathbf{K}t} = \mathbf{X}e^{\Lambda t}\mathbf{X}^{-1}, \tag{5.9}$$

where $\mathbf{X}$ is the eigenvector matrix of $\mathbf{K}$, and Λ is the eigenvalue matrix of $\mathbf{K}$, equation 5.8 can be written as:

$$\mathbf{C}(t) = \mathbf{X}e^{\Lambda t}\mathbf{X}^{-1}\mathbf{C}_o. \tag{5.10}$$

Equation 5.10 gives the fitting functions for each state depending on the initial subset of points from the overall histogram. In order to reduce the number of fitting parameters from four, the equations 5.2–5.4 can be used to relate the rates,

$$\Rightarrow r_2 = \frac{r_1[-]}{[o]}, r_4 = \frac{r_3[o]}{[+]}, \tag{5.11}$$

leaving two free parameters r_1 and r_3 for fitting.

In the case of figure 5.1, the initial population of the system was:

$$\mathbf{C}_o = \begin{bmatrix} 1 \\ 0 \\ 0 \end{bmatrix}, \tag{5.12}$$

because all of the points selected are initially in the negative state.

5.1.3 Benefits and Limitations

The method outlined here was very successful at determining the specific transition rates between DB charge states on the dataset it was applied to [6]. One of the benefits of this method is that it is able to handle selections of data with large overlap between states. Many analysis methods require pure states with minimal overlap between them. This benefit arises from the $\mathbf{C}_o$ matrix which can accommodate arbitrary selections for the initial subset of points. For instance, if a section of points was chosen in a region that contained 50 % negative state and 50 % neutral state, the entries of $\mathbf{C}_o$ would be .5, .5, 0 respectively.

The method, however, is limited by the need for repetitive peak finding, and histogram fitting. As states become less populated during the analysis the peaks become harder to detect and fit. This also limits the ability of the method to analyse datasets that contain short lived states that might only appear for a small subset

of the time-trace. One final limitation to mention for this analysis technique is that simultaneous fitting of the curves to the fitting functions only scales proportionally to the number of states. That is, for three states there are only three curves to simultaneously fit, and for a system with four states there would only be four curves to simultaneously fit. Having more curves (constraints) in this case helps reduce the potential error in the calculated rates. Adaptations have been explored to remedy this particular limitation [60].

5.2 Method 2: Signal-Pair Correlations

In order to overcome some of these limitations and implement a more versatile analysis method, another technique utilized in biophysics and fluorescent chemistry was implemented [18–20, 70], Signal-Pair Analysis. This technique overcomes many of the limitations of the first method, and also provides a unique way to visualize data in the form of signal-pair histograms. These histograms will be introduced in section 5.2.3 briefly and discussed in detail in Chapter 6. In order to test the assumption made both in scheme 4.2 and scheme 5.1 that a direct transition between the positive and negative state is negligible, this method was derived utilizing a more general scheme to determine the relevant equations, as will be shown in section 5.2.2.

5.2.1 Outline of Method

Similar to the previous method outlined, the Signal-pair method involves observing the values of groups of points as time advances. However, in this method points are chosen from within each state (regions of interest) instead of just one starting vector, so they can be analysed in pairs (Figure 5.3). The limitation of this method is that it is based on the assumption that each region selected within a state is pure, with no contributions from other states (i.e. significantly overlapping peaks). Although, in most cases it is possible to select a region with maximum signal, and minimal overlap with other states that satisfies this criterion. A signal-pair correlation value (Equation 5.24) is calculated between each pair of regions within each

state at each time-step based on the original number of points in those regions at $t = 0$, and the number of points currently in those regions [18]. Fitting functions are then derived (as will be shown below) for each signal-pair correlation plot, and all of them are simultaneously fit utilizing a similar least-squares algorithm to the one described in section 4.2.1. The rates of transition are given from the parameters of these fitting functions.

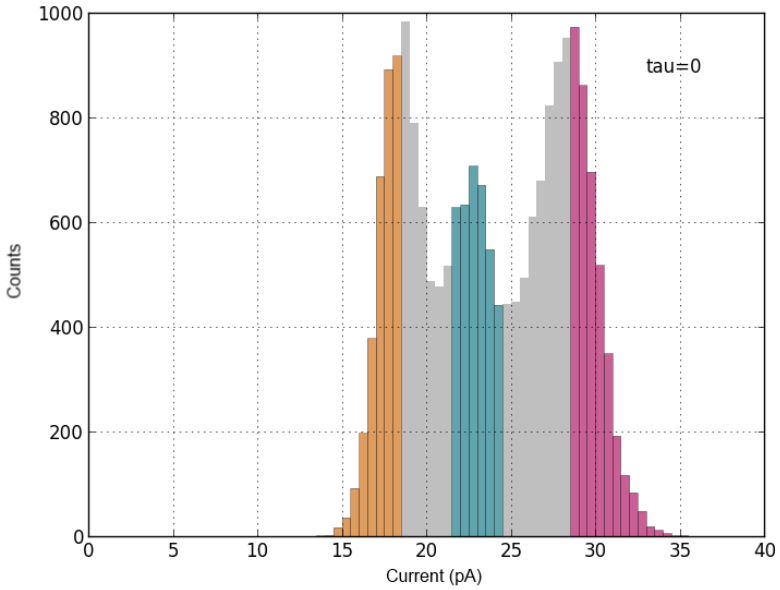

Figure 5.3: A histogram of a telegraph time-trace at a particular distance from a DB centre showing three charge states. Each coloured region is a selection of points at $\tau = t = 0$ from within each state to maximize the signal, and minimize the overlap with other states.

5.2.2 Derivation

A more general set of rate equations was used here in order to enable testing later in the analysis of the assumption that there is a linear pathway between charge states. As shown in scheme 5.13, the possibility of a transition between the negative and positive state is no longer excluded.

$$\mathrm{DB}^{-} \underset{r_2}{\overset{r_1}{\rightleftharpoons}} \mathrm{DB}^{o} \underset{r_4}{\overset{r_3}{\rightleftharpoons}} \mathrm{DB}^{+} \quad , \qquad \mathrm{DB}^{-} \underset{r_5}{\overset{r_6}{\rightleftharpoons}} \mathrm{DB}^{+} \tag{5.13}$$

From this scheme, at steady-state, the following master equations can be written:

$$\frac{d[-]}{dt} = r_2[o] + r_5[+] - (r_1 + r_6)[-] = 0, \tag{5.14}$$

$$\frac{d[o]}{dt} = r_1[-] + r_4[+] - (r_2 + r_3)[o] = 0, \tag{5.15}$$

$$\frac{d[+]}{dt} = r_3[o] + r_6[-] - (r_4 + r_5)[+] = 0. \tag{5.16}$$

In both section 4.1.3 and 5.1.2 the master equations were constructed in the same way. All of these equations when solved satisfy the constraints of detailed balance (all forward flows are balanced by the reverse flows) [61, 67, 71], however, it is extremely important to note that even though they mathematically satisfy these constraints detailed balance does not apply. Detailed balance is an equilibrium condition where there is no longer any net flux of energy or matter into or out of a system (closed system) [61, 67, 71]. Closed systems at equilibrium (with detailed balance) allow for the use of the partition function from statistical mechanics to calculate their thermodynamic quantities (entropy, free energy, etc...) [61, 71]. The DB system studied here is an open system, constantly exchanging electrons from the tip to DB to silicon substrate (Figure 3.3) that is in a steady-state away from its thermodynamic equilibrium [17]. As a result, a detailed balance interpretation would be incorrect [61]. Instead, the system can only be described by the transition rates in the scheme 5.13 along with the associated parameters that cause the steady-state (bias, radial tip position, and temperature), with no ability to calculate thermodynamic quantities [61]. The steady-state is identified because after a sufficiently long time of data acquisition, the probabilities of being in each state remains constant (the population ratio of the peaks in the histograms do not change significantly with longer acquisition times).

In order to solve these master equations and determine the relationships between rates, equations 5.14 to 5.16 can be put into matrix form:

$$\begin{bmatrix} -[-] & [o] & 0 & 0 & [+] & -[-] \\ [-] & -[o] & -[o] & [+] & 0 & 0 \\ 0 & 0 & [o] & -[+] & -[+] & [-] \end{bmatrix} \begin{bmatrix} r_1 \\ r_2 \\ r_3 \\ r_4 \\ r_5 \\ r_6 \end{bmatrix} = \begin{bmatrix} 0 \\ 0 \\ 0 \end{bmatrix}, \tag{5.17}$$

$$\Rightarrow_{rref} \begin{bmatrix} 1 & -\frac{[o]}{[-]} & 0 & 0 & -\frac{[+]}{[-]} & 1 \\ 0 & 0 & 1 & -\frac{[+]}{[o]} & -\frac{[+]}{[o]} & \frac{[-]}{[o]} \\ 0 & 0 & 0 & 0 & 0 & 0 \end{bmatrix} \begin{bmatrix} r_1 \\ r_2 \\ r_3 \\ r_4 \\ r_5 \\ r_6 \end{bmatrix} = \begin{bmatrix} 0 \\ 0 \\ 0 \end{bmatrix}, \tag{5.18}$$

giving:

$$r_1 = \frac{r_2[o]}{[-]} + \frac{r_5[+]}{[-]} - r_6, \tag{5.19}$$

$$r_3 = \frac{1}{[o]}((r_4 + r_5)[+] - r_6[-]). \tag{5.20}$$

These equations simplify to equation 5.11 in the case of a linear scheme where $r_5 = r_6 = 0$. The relations here allow for a reduction of fitting parameters from six free parameters to four.

These free parameters can then be used in the following function [19, 20, 72] to derive the cross-correlation fitting functions for each pair of regions within the states i, j (Figure 5.3):

$$g_{i,j}(t) = \frac{\mathbf{1}^{\mathrm{T}}\mathbf{V}_{i,j}e^{\mathbf{K}t}\mathbf{V}_{i,j}\mathbf{p}_{ss}}{\left(\mathbf{1}^{\mathrm{T}}\mathbf{V}_{i,j}\mathbf{p}_{ss}\right)^2}, \tag{5.21}$$

where i is the initial state, and j is the final state j. The matrix $\mathbf{K}$ is the following rate matrix (created from equations 5.14 to 5.16) where each i, j element represents the transition between state j to state i and the sum of each column is zero.

$$\mathbf{K} = \begin{bmatrix} -r_1 - r_6 & r_2 & r_5 \\ r_1 & -(r_2 + r_3) & r_4 \\ r_6 & r_3 & -r_4 - r_5 \end{bmatrix}. \tag{5.22}$$

$\mathbf{V}_{i,j}$ is the transition monitoring matrix, which has only one non-zero element of the transitions being observed, $V_{i,j} = 1$, and the matrix $\mathbf{1}$ is simply a vector of ones. In the original publication of these methods [19, 20, 72] the steady-state probabilities $\mathbf{p}_{ss}$ were derived beforehand in terms of the free-fitting parameters, however, in this implementation the steady-state probabilities were calculated directly from these datasets and the Gaussian fits of the associated histograms. Each steady-state probability was defined as the number of points in each state divided by the total number of points in the dataset, giving a numeric vector. This was done in order to reduce computational expense as it was realized that the derived functions for the steady-state probabilities reduced to the numeric vector when the relationships between parameters (Equations 5.19, 5.20) were utilized.

To calculate the experimental values of g to be fit with equation 5.21 the quantity N must be defined.

$$N(\tau, s_I, s_F) = \{s(t) \in s_I \pm \Delta s | s(t+\tau) \in s_F \pm \Delta s\}, \tag{5.23}$$

where s_I is the initial region of interest in state i, s_F is the final regions of interest in state j and Δs is half the width of the region of interest in each state [18]. Essentially, $N(\tau, s_I, s_F)$ is a count of the number of points of the total dataset $s(t)$ in the initial region of interest in state i that have transitioned to the final region of interest in

state j after a number of time-steps τ (time-step is defined as the space between data points). Figures 5.4 and 5.5 show an example of a region of interest in a particular state, and how the number of points are counted in that region. The half-width Δs in this case was selected to be 1.5 pA. With equation 5.23 the experimental cross-correlation values between the regions of interest within states i, j are given by [18]:

$$g_{i,j}(\tau, s_I, s_F) = \frac{N(\tau, s_I, s_F)T^2}{(T-\tau)N(s_I)N(s_F)}, \tag{5.24}$$

where T is the total number of data points in the time-trace, and $N(s_I)$ and $N(s_F)$ are the number of points in the defined regions of interest within each state i, j at $\tau = 0$ respectively. Equation 5.24 was derived based on the two-time correlation function [18, 70, 73],

$$g_{i,j}(\tau, s_I, s_F) = \frac{p(\{s_I, t\}|\{s_F, t+\tau\})}{p(s_I)p(s_F)}, \tag{5.25}$$

where $p(\{s_I, t\}|\{s_F, t+\tau\})$ is the joint probability of finding the system in the region of interest in state i at time t and in the region of interest in state j at time $t+\tau$, and $p(s_I)$, $p(s_F)$ are the probabilities of finding the system in each region of interest respectively. The probabilities $p(s_I)$, $p(s_F)$ are simply the total number of points in the regions at $\tau = 0$ out of the total number of points in the dataset T,

$$p(s_I) = \frac{N(s_I)}{T}, \tag{5.26}$$

$$p(s_F) = \frac{N(s_F)}{T}. \tag{5.27}$$

The joint probability $p(\{s_I, t\}|\{s_F, t+\tau\})$ is given by identifying the number of points in the dataset in region s_I that have transitioned to region s_F after a number of time-steps τ, out of the total remaining points in the dataset. The number of points remaining in the dataset changes as τ increases since the points with $t+\tau > T$ have no defined value at $t+\tau$ and can no longer be counted. So the number of data points

in the dataset is given by $T - \tau$ in this case. Equation 5.23 can be used to count the number of points in the dataset in region s_I that have transitioned to region s_F, so:

$$p(\{s_I, t\}|\{s_F, t+\tau\}) = \frac{N(\tau, s_I, s_F)}{T - \tau}. \tag{5.28}$$

Placing equations 5.26, 5.27, 5.28 into equation 5.25 gives the experimental correlation function 5.24. The joint probability by definition for independent processes is simply the product of the probability of each process [70, 73]. After the system has reached a steady-state and the transitions are largely independent (the probability of each state is now the steady-state probability) the numerator of equation 5.25 (joint probability) should match the denominator and the value of equation 5.25 will approach one. This behaviour can be observed in figure 5.6 for the experimental cross-correlation values.

The experimental cross-correlation values were first calculated at each time-step τ for each pair of regions (Figure 5.3) based on the scheme 5.1 by setting rates $r_5 = r_6 = 0$. In our case, the number of time-steps used was $\tau = 200$, giving 200 points per cross-correlation plot. For a three state system, six cross-correlation plots are generated per dataset (Figure 5.6). These six plots are then simultaneously fit together with the fitting functions given by 5.21 to determine the rates in the scheme 5.1. In order to determine error bars of these rates, each region of interest can be shifted slightly from the original choice to generate a new region, and the analysis process can be repeated. The error is then given by the standard error in the mean of all the values generated for a particular rate. Typically 27–125 signal pair combinations were utilized by varying each region 3–5 times to generate 27–125 values for each rate. The maximum shift from the centre of the original region of interest was 0.3 pA in order to maintain the criteria of minimal overlap with other states.

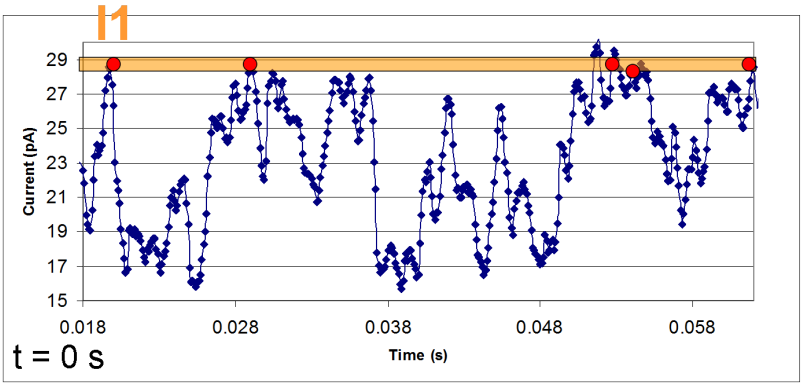

Figure 5.4: A graphical illustration of a region of interest for the signal-pair analysis. In this region at $\tau = 0$ there are a total of 5 points (shown in red).

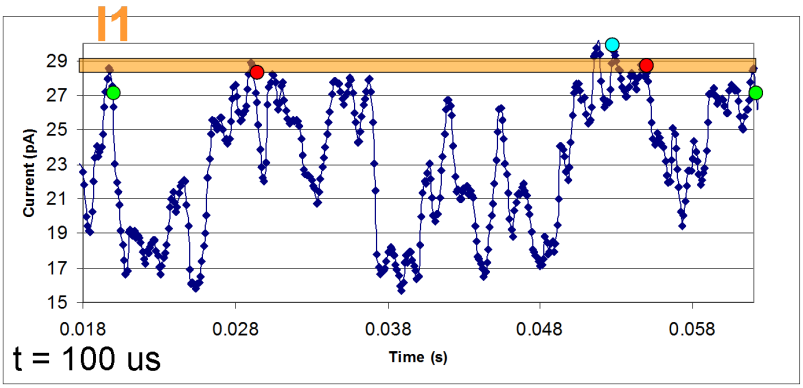

Figure 5.5: After one time-step τ the points identified in 5.4 have now moved to various different values. The number of points in the region of interest at $\tau = 1$ is now 2.

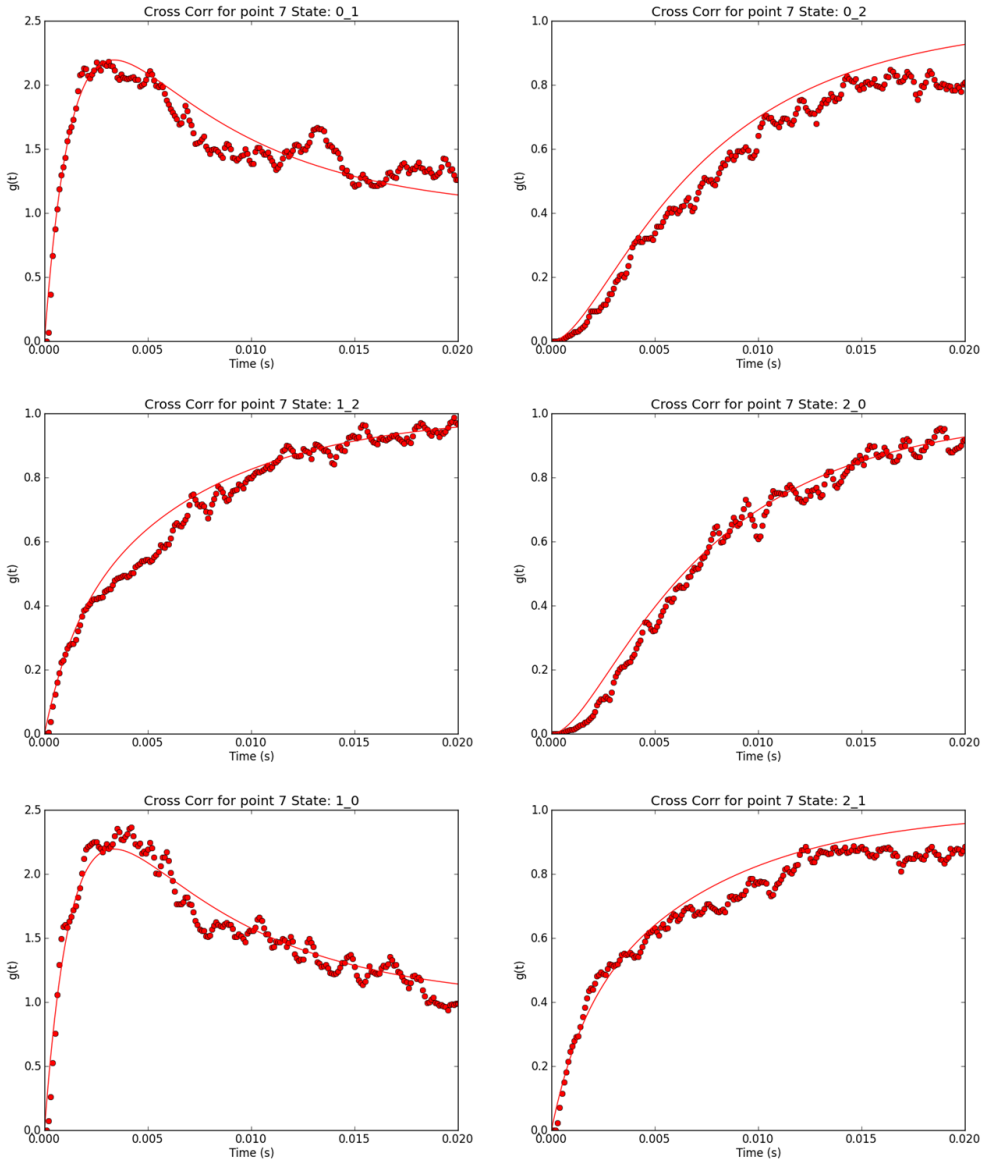

Figure 5.6: Six cross-correlation curves generated from experimental data using equation 5.24 (filled red dots). These curves were then fit simultaneously with the derived fitting functions 5.21 (solid red line). The results of these fits give the transition rates between states in scheme 5.1.

5.2.3 Signal-Pair Histograms

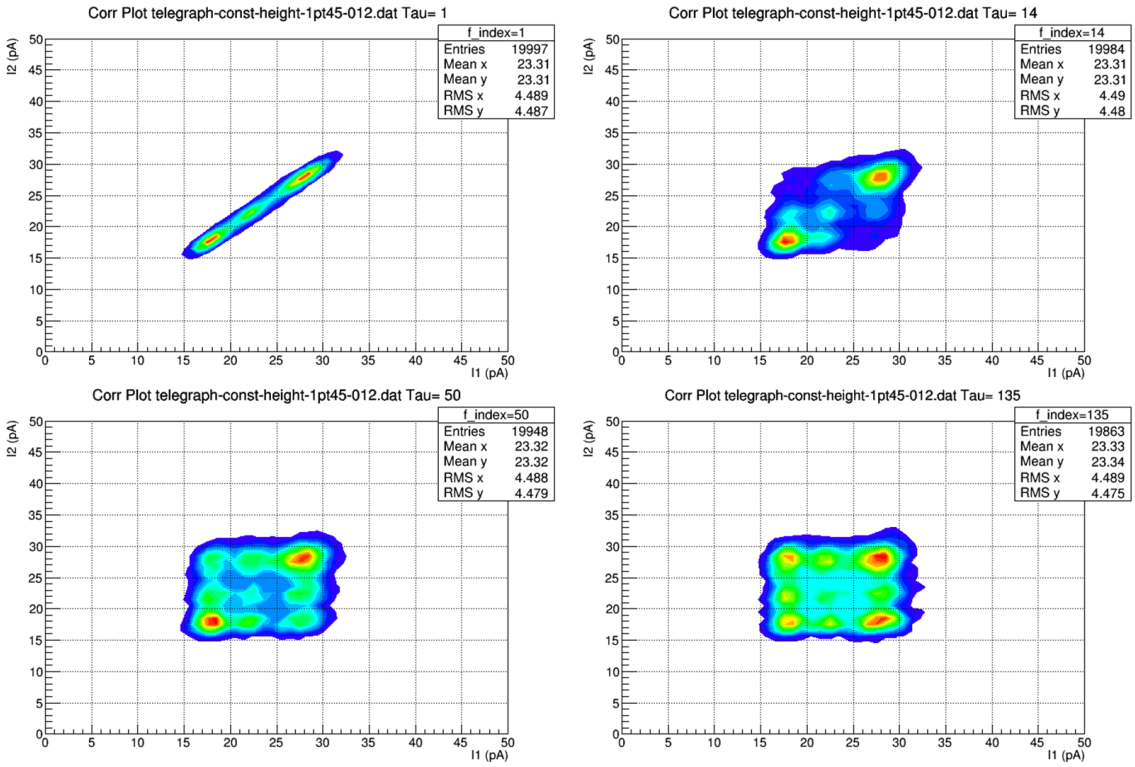

Figure 5.7: An example of signal-pair histograms created from telegraph data taken from a DB at a bias voltage of 1.45 V. The first panel corresponds to $\tau = 0$, the second panel is at $\tau = 14$, the third panel is at $\tau = 50$, and the last panel is at $\tau = 135$.

Signal-pair histograms [18,70] (Figure 5.7) provide a unique way to visualize time series data with multiple states. They are 2D maps that explore the entire space of these data, where each bin population is determined by equation 5.23. For a fixed τ for every bin along the x-axis (treated as region s_I) the value of N is calculated for every bin along the y-axis (treated as region s_F). Based on the content of the bins, it can be observed where population along the x-axis tend to end up after a given time τ. At $\tau = 0$ the histogram appears as a diagonal line (Figure 5.7 panel 1) because each value simply maps back to itself. As τ increases the diagonal spreads out and

regions of preference for the values form (Figure 5.7 panel 2), as τ increased further cross-peaks begin to manifest, indicating transitions between two regions in the data (Figure 5.7 panel 3). Since this method makes no assumption of numbers of states, or their location, it is an easy visual way to determine where states are located, and which ones might have transitions between them. Methods of how to achieve this will be discussed in the next chapter.

5.3 Results

Due to the difficult nature of the experiment, large quantities of easily interpretable data were difficult to obtain. While much of these data did tend to show the expected trends, noise and other factors hampered the resolution of multiple states in many cases, preventing the acquisition of a complete collection of datasets. The complete datasets shown here were taken with multiple tip and sample combinations for different DBs. Aside from datasets taken on the same DBs, because of the different tip and sample combinations these datasets can be considered independent of each other.

5.3.1 Rates as a Function of Radial Tip Distance

Using the procedure to measure and record telegraph noise described in Chapter 3, telegraph noise data were collected for many DBs (Figure 5.8). The principal goal of this investigation was to determine the relationship between the radial distance of the tip from the DB centre and the transition rates between charge states. The signal-pair analysis method was utilized to analyse these data based on the linear scheme 5.1.

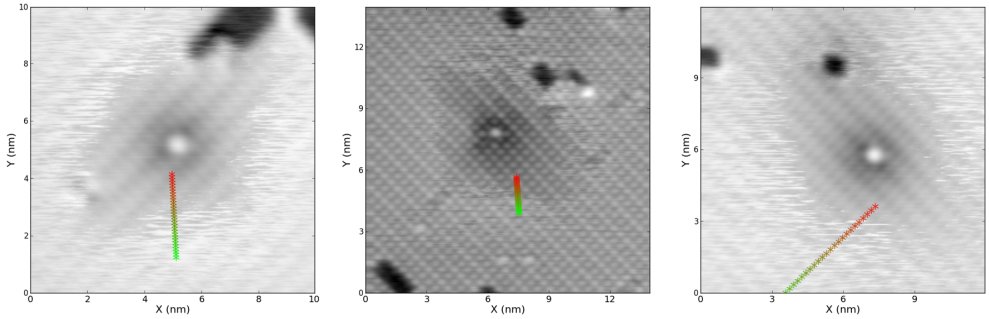

Figure 5.8: STM images taken of some of the DBs studied. All the images are at a bias of 1.40 V and a constant current of 30 pA. The halo and speckle regions are visible in each image indicating fluctuations of the DB charge state due to influence of the tip. The locations where datasets were recorded are marked with stars along the coloured line, the direction of approach of the experiment is indicated from green to red.

It was found that a sample bias of 1.40 V provided the best signal to noise ratio and resolution between peaks in the histograms. Because of this, the majority of these data were collected at this bias. Other biases ranging from 1.20 V to 1.70 V were also explored. Lower biases (below ∼1.30 V) did not end up providing a significant change in signal for each state transition, and as a result the separation between peaks was too small to be resolved in many cases (Figure 5.9). Higher biases (above ∼1.50 V) resulted in too much signal and as a consequence too much noise (Section 3.2.2), so the states became overlapping despite their separation, which also made them impossible to resolve. It is also possible that at these higher biases the transition rates increased to well beyond the bandwidth of the STM pre-amplifier, which would also make it impossible to resolve individual states (Figure 5.10).

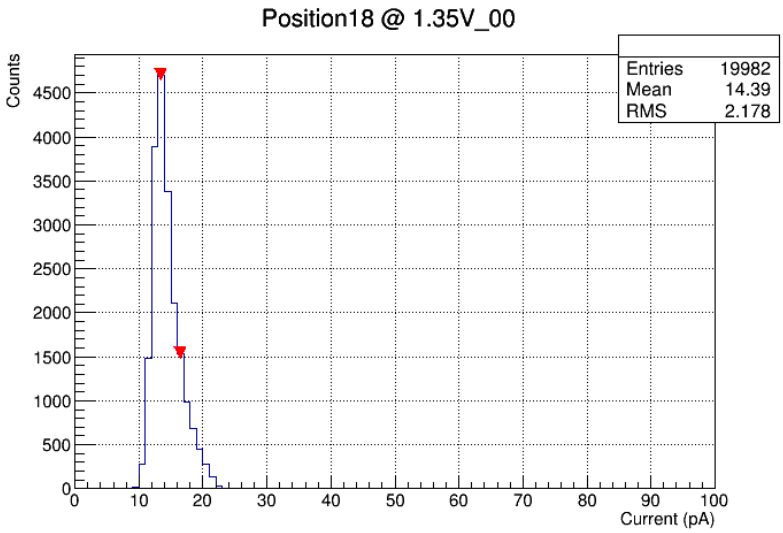

Figure 5.9: A histogram of data collected at 1.35 V. At lower biases there is less separation between peaks, making these data difficult or impossible to analyse with the current methods. In this case, only two of the three states were detected.

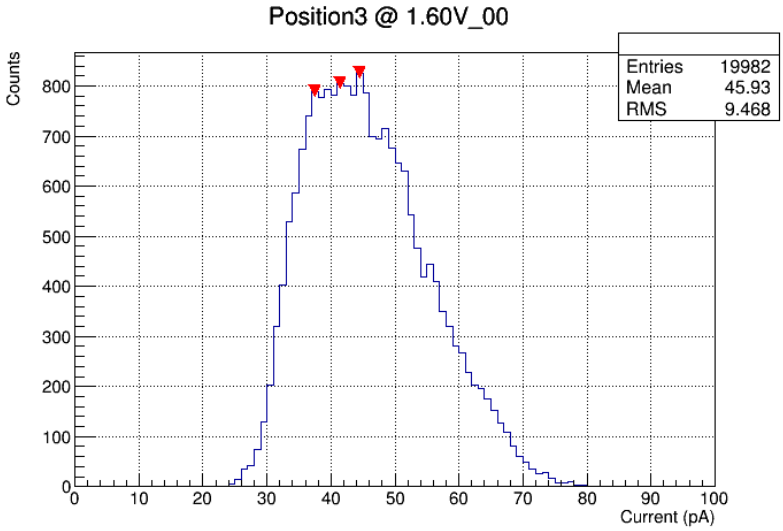

Figure 5.10: A histogram of data collected at 1.60 V. At higher biases the transition rates between states increases beyond the bandwidth of the STM pre-amplifier making it impossible to resolve individual states. This problem is compounded with the higher noise levels with stronger currents. These type of data are also impossible to analyse with the current methods.

A summary of rates obtained at a sample bias of 1.35 V for many DB, tip, and sample combinations is shown in figure 5.11. The results for a bias of 1.40 V are shown in figure 5.12. The results for a sample bias of 1.45 V are shown in figure 5.13. Other biases unfortunately could not be analysed due to the inability to resolve multiple peaks over an entire experiment. Analysis code was created to do a weighted-least squares fitting to account for error bars in the rates of all of these plots. For the emptying rates a mean value was then calculated from these data, and the filling rates were fit to an exponential of the form:

$$r_{filling}(d) = R_o + Re^{-d\alpha}, \tag{5.29}$$

where d is the radial distance from the tip and R_o, R, and α are fitting parameters. Examples of the results of the fits for each rate can be seen in figure 5.14.

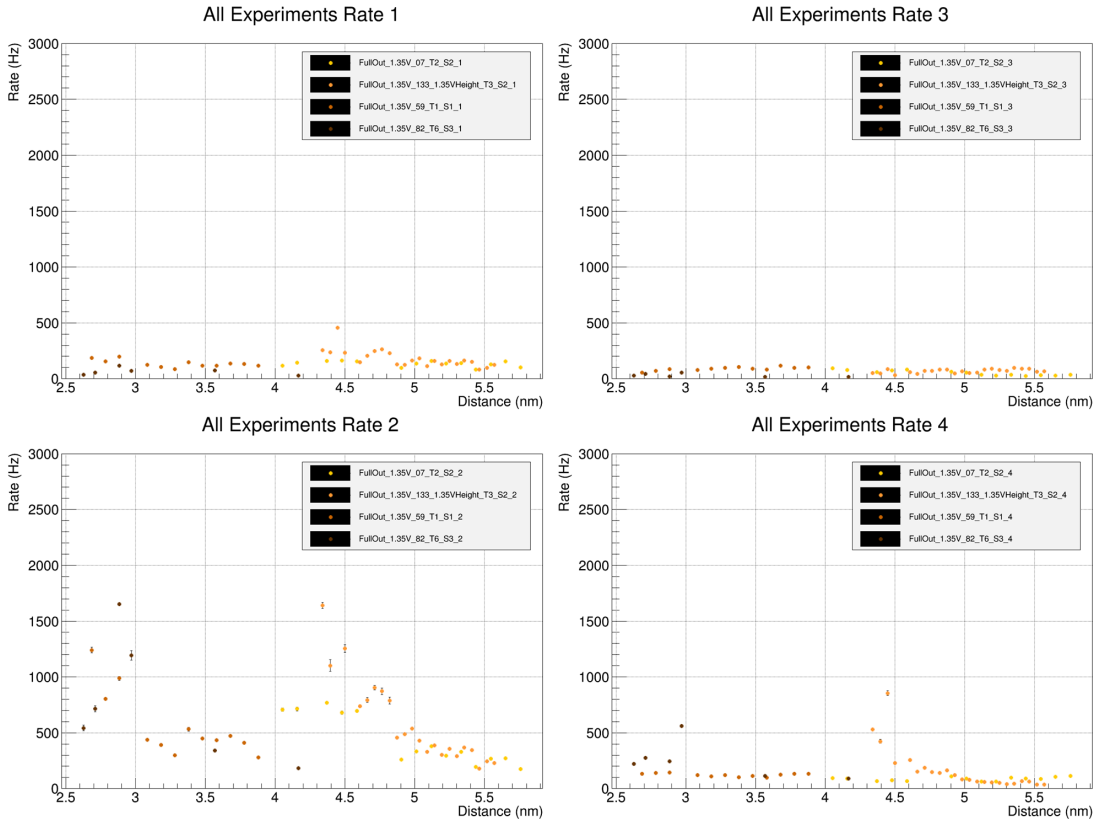

Figure 5.11: A summary of all the rates calculated at various radial tip distances with multiple tip, DB, and sample combinations at a bias of 1.35 V. The rates correspond to the linear scheme 5.1. The error bars were generated by varying the selection of points in each state to create five different regions for a total of 125 different possible signal-pairs. The standard deviation of the 125 values obtained for each rate give the errors. A larger version of these plots is given in figure A.5.

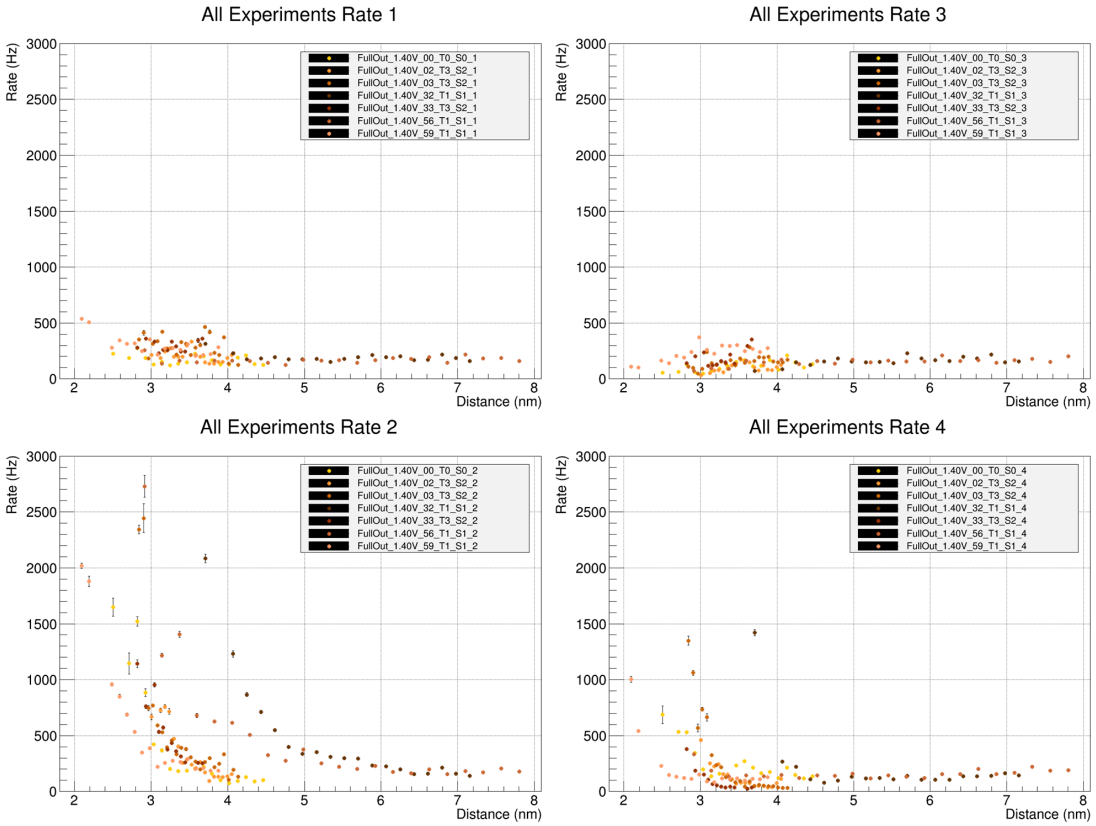

Figure 5.12: A summary of all the rates calculated at various radial tip distances with multiple tip, DB, and sample combinations at a bias of 1.40 V. The rates correspond to the linear scheme 5.1. The error bars were generated by varying the selection of points in each state to create five different regions for a total of 125 different possible signal-pairs. The standard deviation of the 125 values obtained for each rate give the errors. A larger version of these plots is given in figure A.6.

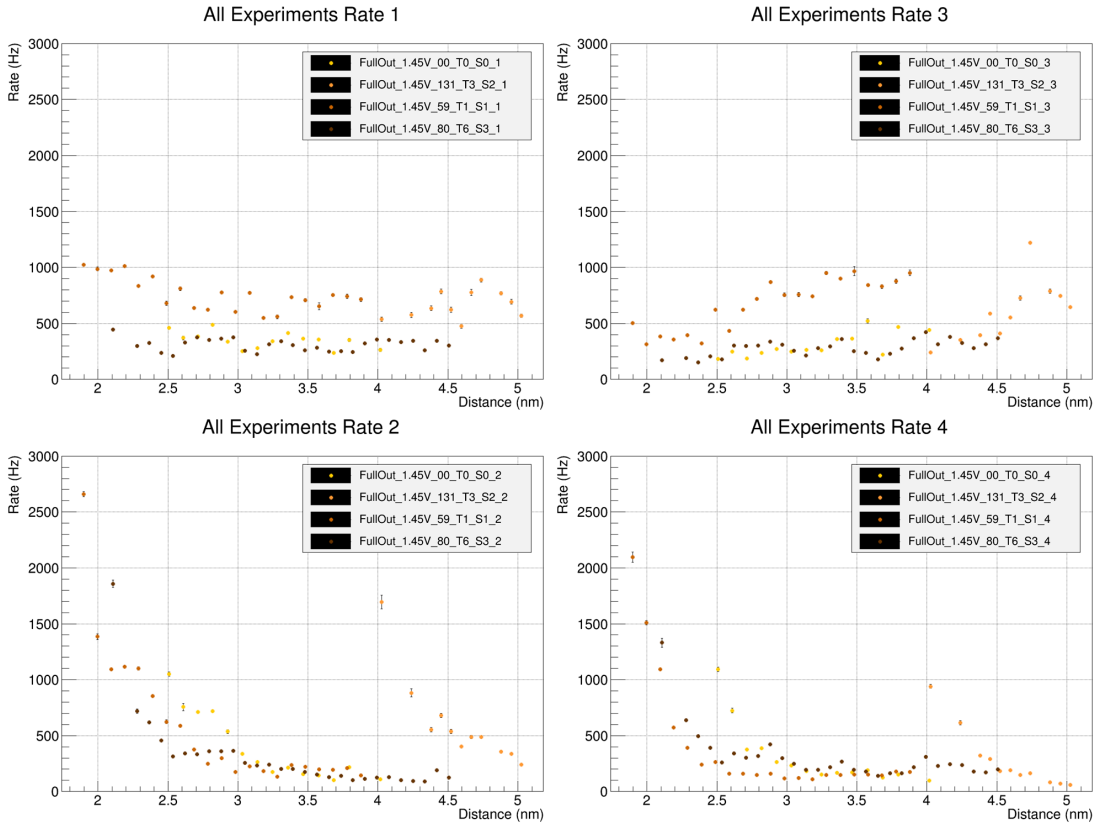

Figure 5.13: A summary of all the rates calculated at various radial tip distances with multiple tip, DB, and sample combinations at a bias of 1.45 V. The rates correspond to the linear scheme 5.1. The error bars were generated by varying the selection of points in each state to create five different regions for a total of 125 different possible signal-pairs. The standard deviation of the 125 values obtained for each rate give the errors. A larger version of these plots is given in figure A.7.

In figures 5.11 to 5.13 the emptying rates (r_1 and r_3) appear to be effectively flat, while the filling rates (r_2 and r_4) appear to be exponentially dependant on radial tip distance. It also appears that the exponential trend is independent of bias, while the flat emptying rates seem to change in magnitude with bias. Between all three biases, the emptying rates were found to be within the range of 50 Hz to 1000 Hz, while the filling rates were found to be within the range of 50 Hz to 3000 Hz.

Another interesting feature to note is that all of the filling rates do not appear to

drop to zero at the farthest tip-DB separation recorded (Figure 5.14). Instead they seem to approach a constant non-zero value.

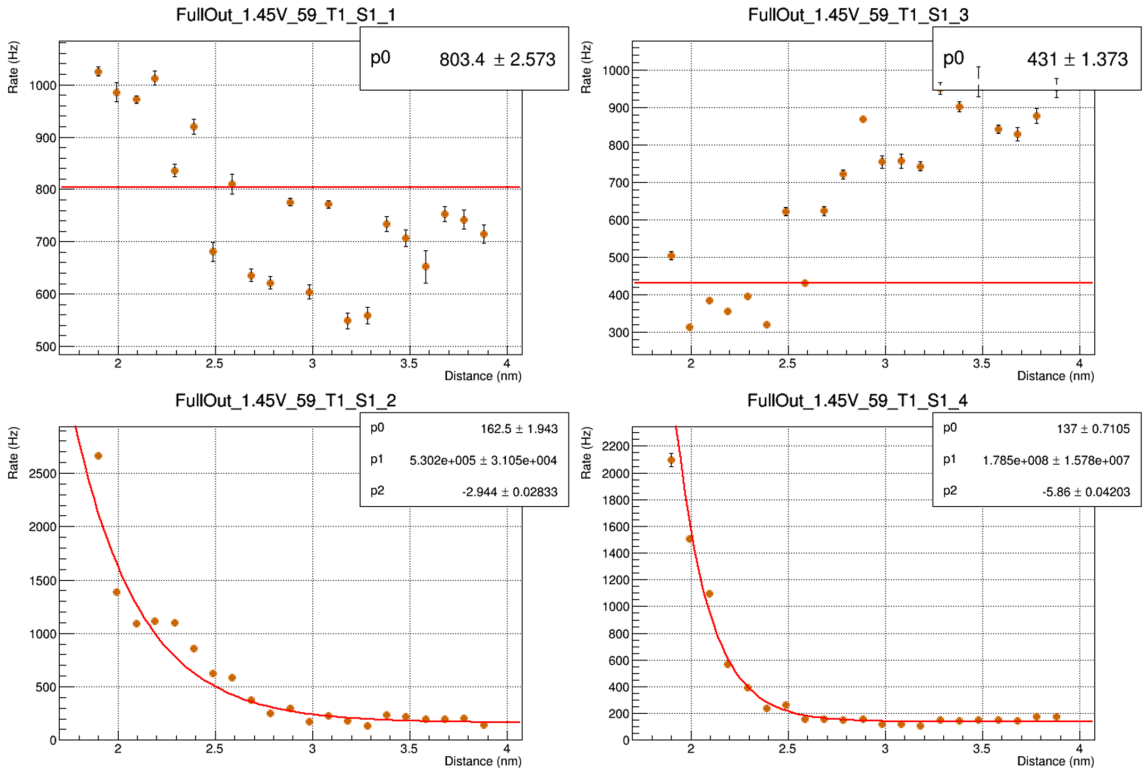

Figure 5.14: An example of how these data in figures 5.11 to 5.13 are fit. The emptying rates are fit with a mean value of all the points, based on weights of the error bars. The filling rates are fit with a generic exponential function 5.29. This particular dataset was recorded at a bias of 1.45 V. The corresponding rates in scheme 5.13 are indicated by the last digit in the title of each panel. Rate 4 (the filling rate from the tip to the positive DB) approaches approximately the rate expected for the set tunnelling current if the tip was directly over the DB ($d = 0$). The fits of the filling rates also appear to not vanish to zero as the radial tip distance is increased.

The analysis was also redone on all of these datasets with the scheme 5.13 implemented, allowing for the possibility of a direct transition between negative and positive charge states. The results of this analysis gave rates that were almost zero or negative in many cases for both rates r_5 and r_6, while giving approximately the

same values for the other rates as obtained from the linear scheme (no statistical difference).

5.3.2 Rates as a Function of Bias

In order to explore how the bias voltage could change the transition rates between states, an experiment was carried out to record the telegraph noise at five distances from a DB with varying biases for each pass. The tip height was set at each bias voltage for each acquisition. The bias voltage was varied between 1.35 V to 1.40 V with 0.005 V spacings. At three of the five distances from the DB, three charge states could be resolved in these data for each bias. Figures 5.15 to 5.17 show the histograms of these data generated at each respective point for varying bias voltage.

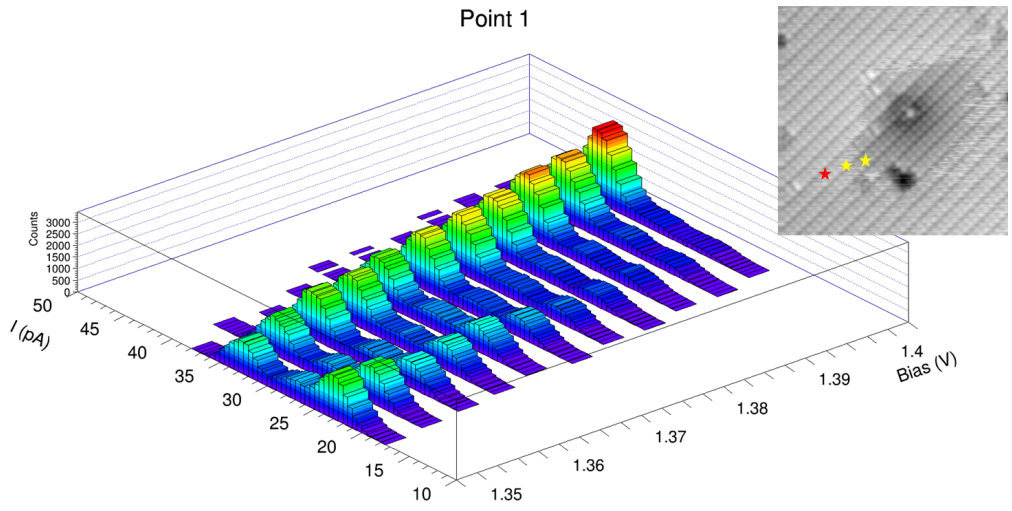

Figure 5.15: The series of histograms from the first point of the bias experiment. Distance from DB centre: 5.5340 nm. The DB starts in a mix of the states at 1.35 V, then becomes mostly positive at 1.40 V.

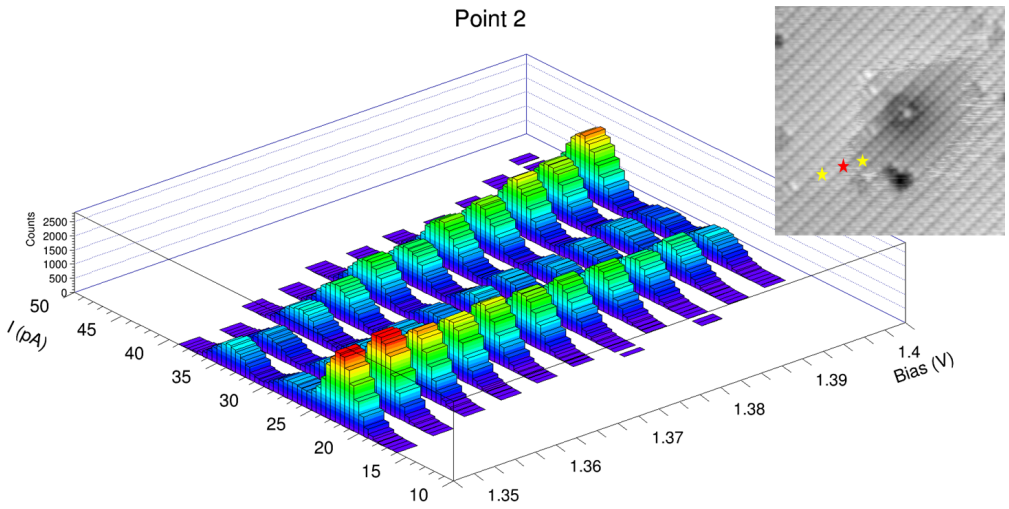

Figure 5.16: The series of histograms from the second point of the bias experiment. Distance from DB centre: 5.0098 nm. The DB is still a mix of states at 1.35 V, but tends to be more negative. The DB still becomes increasingly positive at 1.40 V.

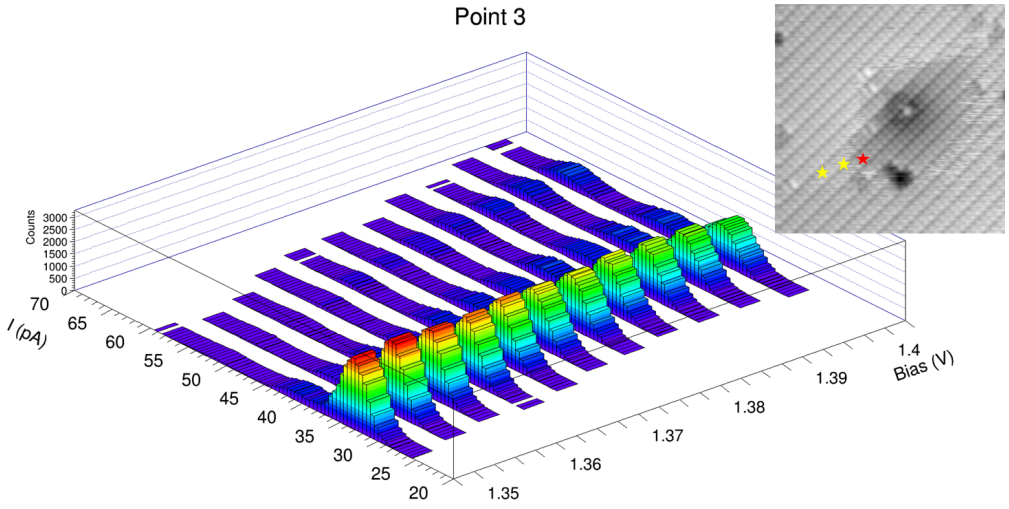

Figure 5.17: The series of histograms from the third point of the bias experiment. Distance from DB centre: 4.4886 nm. The DB is very negative at 1.35 V, and only becomes slightly less negative at 1.40 V.

The rates calculated from these data for each point can be seen in figures 5.18 to

5.20. The emptying rates show a linear increase with increasing bias, while the filling rates show almost no dependence on bias. A very interesting feature in these figures is that there always seems to be a difference in magnitude between the filling rates. This type of gap between the values of the rates also manifests in the emptying rates as the radial tip-DB separation is decreased (Figure 5.20).

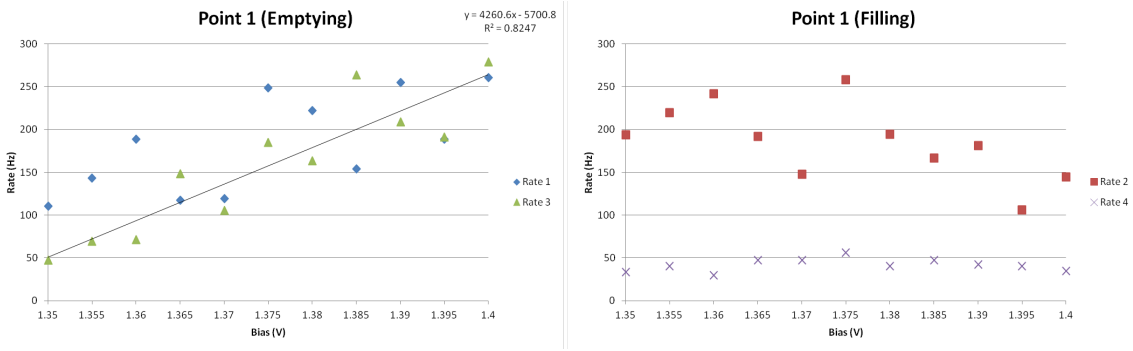

Figure 5.18: The rates calculated for each histogram in figure 5.15 representing the same spatial location, but different bias. The filling rates all appear to be flat with increasing bias. This agrees well with the ideas put forward that the radial tip distance is the most important factor in determining the filling rate. The emptying rates appear to increase linearly with bias. Their dependence on bias also follows from the assumption that the emptying rate is closely related to TIBB.

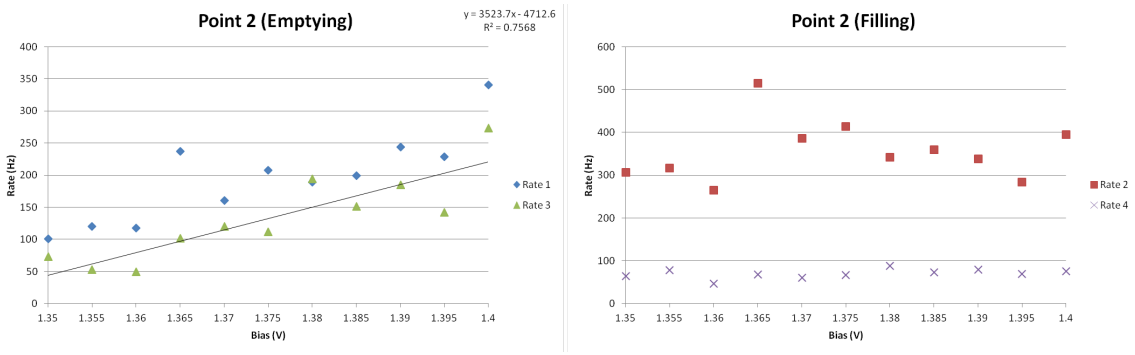

Figure 5.19: The rates calculated for each histogram in figure 5.16 representing the same spatial location, but different bias. The filling rates all appear to be flat with increasing bias still as the tip moves closer to the DB. The emptying rates still also appear to follow a linear trend with increasing bias, though the slope of the line is reduced.

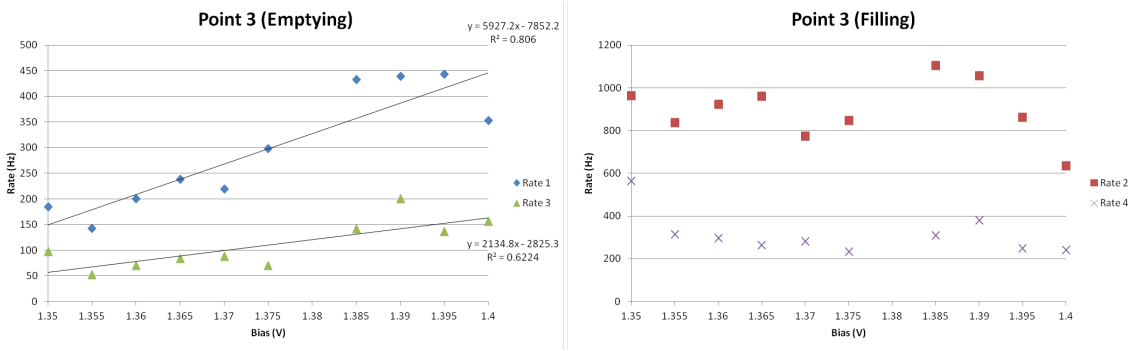

Figure 5.20: The rates calculated for each histogram in figure 5.17 representing the same spatial location, but different bias. The filling rates all appear to be flat with increasing bias still as the tip moves even closer to the DB. The emptying rates still also appear to follow a linear trend with increasing bias. There is a split between the rates now as $r_1 >> r_3$. This could be due to increased band bending as the tip is at the closest approach to the DB of the three distances discussed here.

5.3.3 Rates as a Function of Set-Point

When acquiring telegraph data at different bias voltages for a particular DB, there were two methods to run the experiment. The first method was to lock the tip

at a constant height (an arbitrary decision) and leave the tip at this height for the duration of the experiment while varying radial tip distance and bias voltage. The benefit of this method is that all datasets that were taken at the same height can be readily compared since there was no additional change in parameters. This allows for the isolation of the effect of bias voltage without convolving it with a change in tip-sample distance. The drawback to this method, however, is that if the tip height is set too high, the tunnelling current for lower biases becomes too weak to record any meaningful data. The converse is also a problem; if the tip height is set too low, at higher biases the tunnelling current can become too large, giving useless data and endangering the tip.

The second method involves setting the tip height for each bias before performing the experiment. The drawback to this method is that it potentially adds an additional variable when considering the effects of varying bias voltage. The benefit of this method is that it allows for lower biases to be explored since there is sufficient tunnelling current to be recorded. It also allows for higher biases to be explored because it ensures that the tunnelling current doesn't initially become too large and endanger the tip.

In order to test if there is a significant difference between the results obtained from the two methods in the range of biases typically explored (1.30 V–1.60 V) a dataset was taken at a bias of 1.35 V with tip heights set at various values (determined by the set-points for the tunnelling current of 1.45 V, 1.40 V and 1.35 V). The results are shown in figure 5.21. The datasets obtained with the tip height set at 1.45 V were only able to produce two data points in these figures because of the lack of tunnelling current (mentioned as a drawback in the first method), which made it difficult to obtain data with three resolvable peaks.

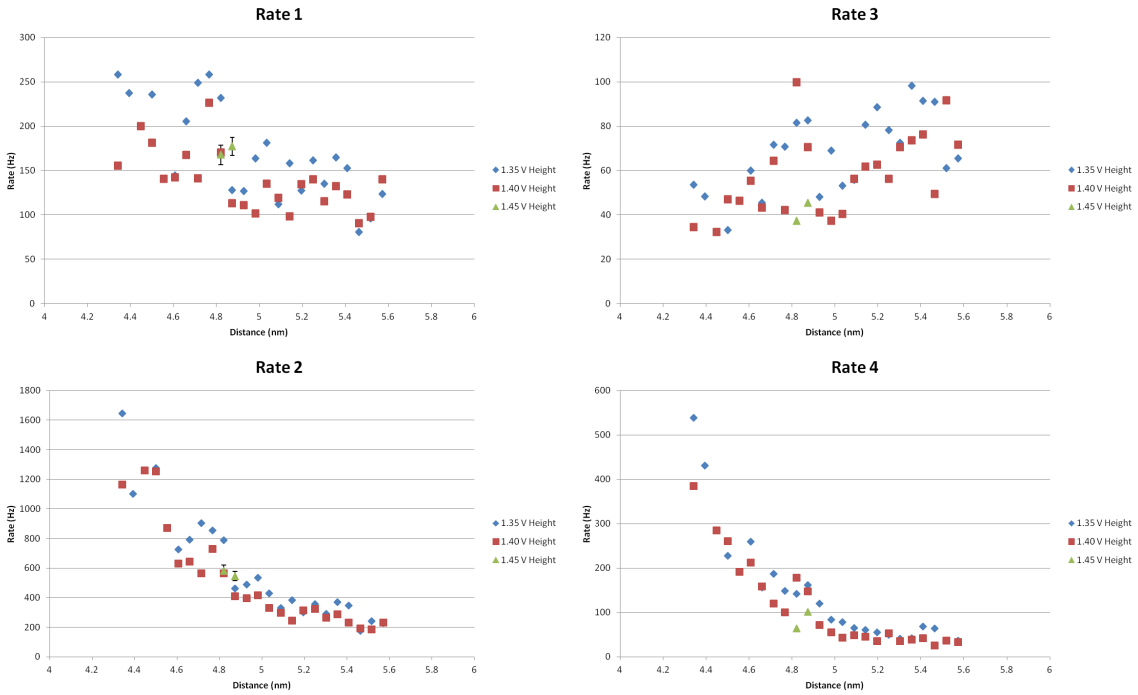

Figure 5.21: The results of a telegraph experiment where the tip height was set according to particular bias voltages before the beginning of each experiment. Over the range of bias voltages explored, setting the tip height at different bias voltages (1.35 V–1.45 V) did not significantly change the rates calculated at each radial tip distance. At a tip height set at 1.45 V, only two data points had three resolvable states due to the low signal due to the largest tip sample distance. The blue points correspond to the first method of data acquisition, while the other two (red and green) correspond to the second method.

5.4 Discussion of Quantitative Results

5.4.1 Flat and Exponential Trend, Expected?

The very first assumptions made in the simple toy model described in Chapter 4 were that the charging followed a linear pathway and that there were constant emptying rates, along with exponentially dependent filling rates on radial tip distance. While these assumptions were based on sound physical grounds, it was not expected

that the experimental results would follow so closely.

The emptying rates found in section 5.3.1 indeed show almost no dependence on the radial distance of the tip from the DB centre. The rates are the lowest for the lowest bias of 1.35 V, and increase with increasing bias. This behaviour was also observed in [6]. The main mechanism of the emptying process that has been proposed for the low temperatures utilized in the experiment (unlike the many other possible processes at standard temperatures [17]) is that electrons can tunnel into the conduction band from the DB levels inside the gap (Figure 3.3). For degenerately doped silicon of the kind used, the Fermi-level is generally inside the conduction band itself, but it is known that the heating of the sample during preparation can cause a dopant depletion layer near the surface that brings this level back down into the band gap [59] (Section 3.1.3). The tunneling to conduction band mechanism can be used to explain the dependence of these emptying rates on the applied bias voltage. As the bias voltage increases, the TIBB becomes more severe, lowering the barrier for the electrons to escape into the conduction band (Figure 3.1 and 3.3). With lower barriers for electrons to escape, the emptying rates increase as has been observed in figures 5.11 to 5.13 along with these data shown in figures 5.18 to 5.20. The linear trend of this increase however needs to be studied further, with a larger bias range as well.

The insensitivity of the emptying rates to the radial tip distance from the DB centre can be attributed to the fact that the TIBB is effectively constant over the length scales of the experiment [6, 17, 74–76] for a very sharp tip. The fluctuations of the rates about a mean as the tip is moved radially closer are likely due to other random nearby processes or defects (that are influenced by the presence of the tip), which can instantaneously affect the local band bending, and therefore the emptying rates. In order to verify this, many trials should be taken with identical conditions in fixed locations to see if the fluctuations are constant, or vary randomly with each data acquisition. Some observations have also been made where the emptying rates do not show a flat trend. This could be due to dull or asymmetric tips for which the assumption of uniform band bending over the length of the experiment breaks down, and also merits further study.

The filling rates found in section 5.3.1 also agree with the early assumption that electrons tunneling from the tip was the dominant mechanism for filling, and so should vary exponentially with radial tip distance. The exponential fitting of equation 5.29 to the curves agree very well with these data (Figure 5.14 for example). Despite the sensitivity to radial tip distance, the filling rates showed little to no dependence on the bias voltage (Figures 5.18 to 5.20). This is expected if tunneling of electrons from the tip is the main filling process. The tip Fermi-level is always well above the DB levels inside the band-gap (Figure 3.3) for the biases considered here. Because of this there is always a vast sea of electrons to supply either state (constant density of states) regardless of the bias voltage used. Since changing the bias voltage does not change the number of available electrons to fill the DB, the filling rates should not be influenced.

Strong support has also been found that the DB follows a linear charging scheme (scheme 5.1). When the general scheme 5.13 was tested, allowing for the possibility of transitions directly between positive and negative DB charge states, the values found for the rates r_5 and r_6 were either negligible ($\sim$0 Hz) or negative (not physical). While these results do no rule out the possibility of a direct transition, they do show that they do not play a significant role in the observed dynamics. This is especially true since the values originally found for r_1 to r_4 with the linear scheme did not differ significantly from the values found with r_5 and r_6 included.

The most interesting result to come about from these experiments, however, is the fact that the exponential filling rates don't appear to approach zero as the tip moves further away, but instead approach a non-zero value. This can be seen explicitly in fitting parameters in figure 5.14, with all the fits of these data in figures 5.11 to 5.13 following a similar trend. Typically it is expected that if the source of electrons (the tip) has moved away far enough from the DB filling events should not occur and the exponential would approach zero as the radial distance $d \to \infty$. Since this does not occur, these trends may be indicative of an intrinsic filling process that occurs even in the absence of the tip. It is entirely possible that the random thermal fluctuations still present at 4 K are sufficient to excite the motion of electrons to and from various defects (or dopants, or other DBs, etc...), causing local band bending changes and

charging events. Further investigation of this phenomenon is required in order to potentially uncover more detail of this complex symphony of moving charges, and local bending of bands.

5.4.2 Radial Tip Symmetry and Relation to Rates

One of the features that stands out when looking at figures 5.11 to 5.13 is that the exponential curves are sometimes offset from each other. Since DBs are physically indistinguishable from one another, this can only be a result of the microscopic geometry and symmetry of the tip. Microscopic differences in tip structure are known to change the shape of the halo observed while imaging [5, 8, 17]. From a non-equilibrium charging perspective [17] the onset of the DB halo is indicative of when electrons are able to begin tunneling from the tip to the DB. With increasing tip radius the halos would therefore become larger. It has been observed on many occasions after a severe tip crash (which dulls the tip) that halos can disappear entirely (Figure 5.22) at biases where they would normally be present. This is because the tip has a large enough radius that electrons are always able to tunnel from the tip, regardless of the location of the tip apex. If the tip has a strange non-symmetric geometry, the halos can appear very asymmetric as well.

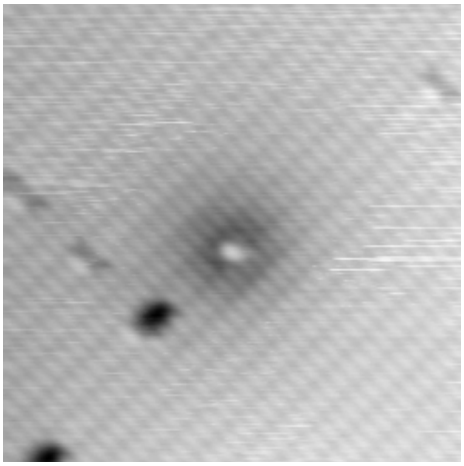

Figure 5.22: An STM image of a DB taken at 1.40 V and a constant current of 30 pA after a severe tip crash, and subsequent tip reforming. Normally at 1.40 V with a narrow tip there is a clear halo as in figure 5.8. Here there is a faint halo at best, as electrons are able to tunnel into the DB from far away due to the large tip radius.

Depending on the direction the DB was approached in an experiment, different geometries of the tip are facing the DB and injecting electrons. Figure 5.23 shows the path of two different experiments on the same DB, with the same tip. The calculated rates resulting from these experiments are shown in figure 5.24. It can be seen that the shape of the curves are very close to each other, other than being offset. This indicates that while the microscopic geometry may change where the onset of the halo (and rates) begin, it does not change how the rates physically behave as a function of radial tip distance.

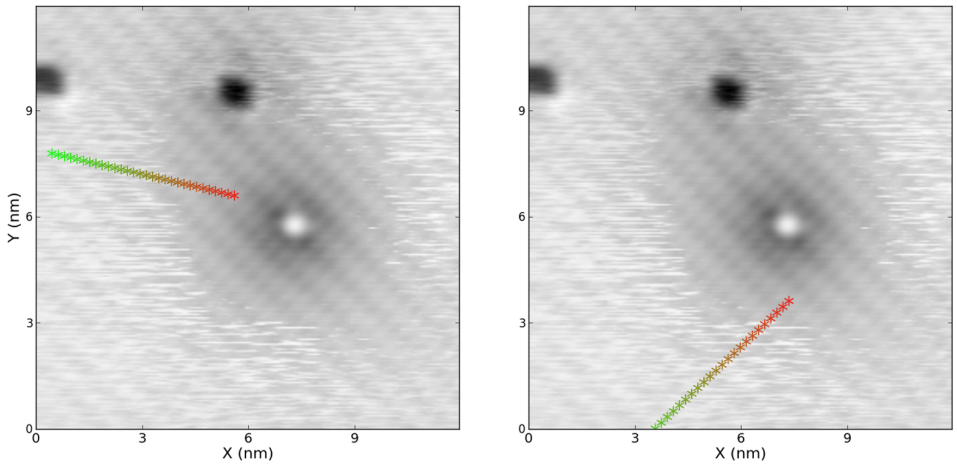

Figure 5.23: STM images of a DB at 1.40 V and constant current of 30 pA. The lines indicate where these telegraph data were recorded in each respective experiment. The experiments begin at the green points and end at the red points.

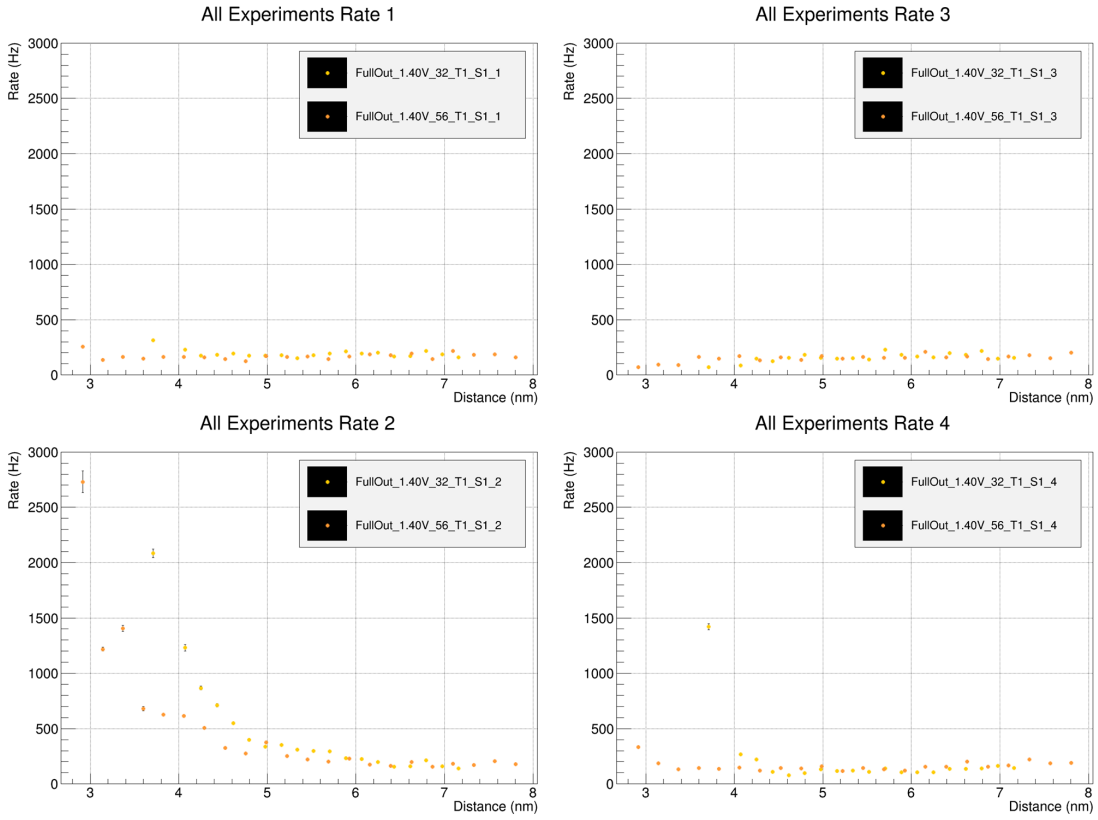

Figure 5.24: The rates calculated for each experiment shown in figure 5.23 for the same DB with the same tip. The emptying rates appear to be identical; however, the filling rates both appear to be offset from each other. A larger version of these plots is given in figure A.8.

The exponential fits to the curves for r_4 (filling from the tip to the positive DB) in general show that as the radial tip distance $d \to 0$ (the tip right over the DB) the filling rate approaches a value on the same order of magnitude as the tunneling current set-point as in figure 5.14. A 30 pA current set-point gives an electron tunneling rate of $\sim 10^8$ Hz (when the tip is over the DB, the DB is the current carrying state in this case). The correct magnitude of this value from the experimental fits gives confidence that they are correctly representing the physical system. One conclusion that can be drawn from this result is that the directions of approach for which the tip has asymmetries tend to incorrectly predict the filling rate when the tip is directly

over the DB. One reason for this could be the fact that the assumption of uniform band bending likely breaks down for dull tips. More investigation needs to be carried out to determine if the uniform band bending assumption is valid when the tip is directly over the DB for a very sharp tip as well.

The radial symmetry of the tip is extremely important for reliable and accurate measurement of telegraph noise. Once a tip has crashed, or become double or asymmetric, it may no longer be sufficiently sharp for telegraph experiments (Appendix A). Because of this, the best data were typically collected right after changing to a freshly etched single atom tungsten tip.

5.4.3 Differences Between Rates ($r_1 > r_3$, $r_2 > r_4$)

It was proposed by Taucer, et al. and in Chapter 4 that the emptying rates were of similar magnitude [6, 60], however, after this more detailed investigation was carried out there is strong evidence this is not the case. In addition to TIBB, the DB level also causes charge induced band bending (CIBB) from the electrons contained within the level (Figures 3.1, 3.3). The neutral DB level causes no CIBB because the DB is electrostatically neutral, but the negative DB level with an excess electron causes upward band bending. Based on the emptying mechanism that is sensitive to band bending effects, it should logically follow that the emptying rate from a negative DB should be faster than from a neutral DB. Figures 5.11 to 5.14 show that on average $r_1 > r_3$. Figures 5.18 to 5.20 show that the differences between these two rates becomes even more pronounced the closer the tip is to the DB. The exact reason for this requires further investigation.

It was also proposed that the filling rates were of similar magnitudes. Again, this more detailed investigation has shown that this is likely not the case. Livadaru et al. [17] have calculated the wave functions of a negative and neutral DB orbital, which can help explain the difference between the rates r_2 and r_4, based on some simplifying assumptions. One of the major simplifications is considering the DB orbital as a p orbital (Slater-type) instead of an sp^3 hybrid orbital [17]. This simplification was justified because the DB orbital has a strong p-type characteristic [17]. The results

of their calculations show that the negative DB wave function actually decays more slowly into vacuum than the neutral equivalent, though it has less weight in vacuum overall. The slower decay of the negative DB orbital allows for the possibility of a greater overlap with the tip wave function at larger radial separations [60]. With a greater overlap the negative DB orbital is more readily filled, so a greater filling rate (r_2) should be observed (Figures 5.18 to 5.20). However, this appears to only be valid over the length scale of the experiments performed. Based on the exponential fits (Figure 5.14), there is a point closer to the DB centre where $r_4 > r_2$. One possible explanation for this would be that the neutral DB wave function has a greater weight in this region and therefore a greater overlap with the tip resulting in a faster filling rate. Ideally with a faster pre-amplifier it will be possible to experimentally measure rates within this region in the future to verify this claim as well.

5.4.4 Rates as a Function of Set-Point

As a control experiment, the two methods of data acquisition discussed in section 5.3.3 were tested on a single DB. This was to ensure that there was no significant difference between the results obtained from the two methods in the range of biases typically explored. In figure 5.21 the first method (in blue) and the second method (red and green) all gave nearly identical rates. The differences in the emptying rates are likely due to the same statistical fluctuations that occur between measurements that have been observed in all datasets where the emptying rates fluctuate about a mean value (Section 5.4.1). Again for a sharp tip, the slight changes in tip height ($\sim$0.1 nm) due to changing the bias voltage between 1.30 V–1.50 V while maintaining the same tunnelling current are not expected to change the band bending significantly [6, 17, 74–76]. As a result, the second method of data acquisition was found to be superior because of the better signal to noise ratio it provided while not altering the results of the experiment. The second method has been implemented as the standard procedure for the collection of telegraph data.

5.5 Extensions and Further Work

All of the work and results discussed in this Chapter have only opened the door for extremely detailed investigations into many of the fundamental properties of DBs and their ability to store and release charge. Many open questions have been left, including if there are intrinsic filling and emptying process in the absence of the tip that are thermally activated? And whether or not a true mean value can be found for the emptying rates, or if it has some type of functional dependence on radial distance of the tip as well?

This work has shown that there is certainly an exponential dependence of the filling rates of the DBs on the radial distance of the tip, while they are insensitive to increases in bias voltage. It was found that these rates could range from ~ 50 Hz to over 3000 Hz. It will be essential in the future to find a current pre-amplifier with sufficient bandwidth to allow the resolution of greater and faster rates in order to better understand the DB charging dynamics.

This work has also shown that the emptying rates of electrons from a DB are generally independent of radial tip position, and on the order of 50 Hz to 1000 Hz depending on the applied bias voltage. It appears that these rates increase proportionally with the applied bias voltage. However, a definitive conclusion about this cannot be drawn and moving forward it is necessary to uncover the dependence of these emptying rates on the bias voltage over a much wider voltage range.

One major conclusion that can be taken away from these results is that the DB follows a linear charging pathway (scheme 5.1) with the direct transitions between the negative and positive state playing no significant role on the time scales of the experiment.

An analogous set of experiments has also begun utilizing boron doped silicon (p-type) instead of the n-type described in these experiments. DBs on p-type hydrogen-terminated silicon have shown telegraph behaviour as well [77,78]. In the future, work on both types of crystals will be pursued simultaneously. In addition to this, since it is known that the doping (the position of the Fermi-level) is dependent on sample preparation [59] the experiments should be repeated with samples prepared with

different flashing conditions (Section 2.2.2) such as 1050 °C.

A unique and possible experiment that can be done with the current STM apparatus is to explore the temperature dependence of these rates to see if a trend can be obtained. The STM temperature can be elevated from 4 K using an internal heater. Since the system is not at equilibrium the free energy associated with each transition cannot be calculated from the rates using simple detailed balance procedures [61, 79]. The field of non-equilibrium steady-states (NESS) is rapidly growing since many interesting processes (biological or otherwise) are not at equilibrium, so in the future it may actually be possible to calculate quantities such as free energies from data such as these [80–82].

5.5.1 Extension of Method to N-states

The analytical framework built throughout this project has the potential to be extremely versatile with application to many other systems. The general pathway scheme 5.13 once implemented allowed for quick testing of many possible theories by setting certain rates to zero. It was also cornerstone in helping confirm that the DB did indeed follow a linear charging pathway. By altering the fitting function equation 5.21 and taking the steady-state probabilities directly from these data it has reduced computational expense. These changes have also allowed for the possibility to remove the need to derive complicated equations for the probabilities before hand. The master equations, and the relationships between variables need to be calculated before any analysis can be done. By taking steady-state probabilities directly from these experimental data, it constrains the analysis to obey whatever steady-state conditions are present in nature. Removing the need to calculate parameter (rate) relations can be of great use in cases where the master equations might be too complex to easily solve. The analysis was tested by leaving all parameters free (not using equations 5.19, 5.20); the calculated rates were not significantly different from when they were originally calculated using two free parameters. This versatility and adaptability has led to the initial development of analytical code that is able to handle N-states with N-rates simply by changing the rate matrix $\mathbf{K}$ without need to

derive any additional equations. Further tests of this code need to be completed with simulated data of other multi-state systems that may be in more complex steady-states (such as scheme 5.30 without backward pathways) in order to fully assess the strengths and weaknesses of this new adapted method, and its potential application to analyse other processes.

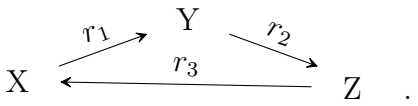

(5.30)

5.5.2 Coupled DB Experiment

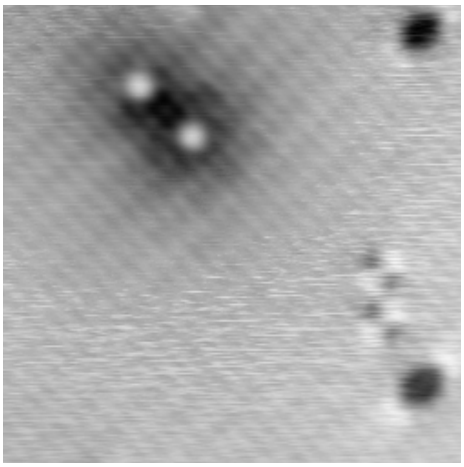

Figure 5.25: An STM image taken at 1.40 V of two tunnel-coupled DBs. The halo region still remains with two DBs, and telegraph noise can be recorded. There have been hints of other charge states in the telegraph signals that can be resolved when two DBs are coupled.

The extension of the analytical method to N-states was in part driven by the progression of experiments from telegraph measurements on a single DB to a pair of coupled DBs (Figure 5.25). Early experiments have shown that there may be more than three charge states that can be resolved within these data from this system.

In order to complete this study, the experimental techniques and analysis tools still require significant refinement in the future. However, they both hold a lot

of promise in revealing detailed insight into the coupled dynamics of a simple DB system. Understanding the behaviour of coupled systems is paramount on the road to DBs becoming part of practical devices.

Chapter Six

Simulation of Telegraph Dynamics

In order to better understand the relationship between the observed telegraph noise dynamics, and the physical filling and emptying rates it was necessary to create simulations where all the parameters could be varied or set in a known fashion. With these simulations, the effect of noise, the magnitude of rates, and the different charging schemes could all be tested and analysed using the methods described in the previous Chapter. These simulations also allowed for a basic evaluation of the analysis methods. All of the rates in the simulation were set to known values and data were simulated. By analysing these simulated data, discrepancies between the input rates and the determined rates were evaluated.

6.1 Roulette Wheel Selection

The charging of the DB is considered to be a stochastic process, so a simple stochastic algorithm was created to simulate the observed dynamics based on roulette wheel selection [83]. In this algorithm the probabilities of an event for each state are used to divide the interval between 0 and 1 (inclusive) into subintervals proportional to the probability of that event (Figure 6.1). Once the interval is divided, a pseudo-random number generator is used to randomly draw a number from a uniform distribution between 0 and 1 (inclusive). The value of the number will fall into a subinterval corresponding to a particular event thus selecting for that event. Events with larger probabilities will be selected more often since they take up larger portions of the number line.

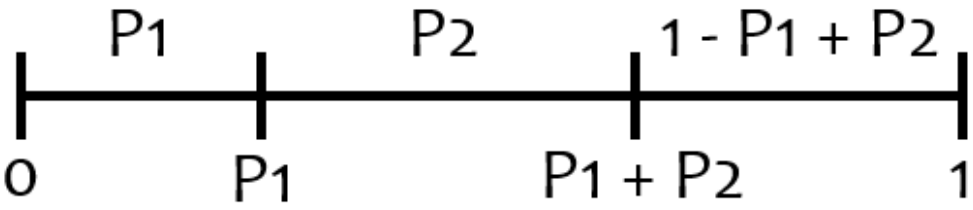

Figure 6.1: The number line between 0 and 1 divided into regions proportional to the probability of selection of each outcome.

For a general three state system (Scheme 6.1) similar to scheme 5.13 there are three possible events for each state. In order to remain completely general, in this scheme there is no reference to charge state or a filling/emptying rate in any particular case. There are simply three possible states X, Y, Z with corresponding alphabetical rates defined in scheme 6.1.

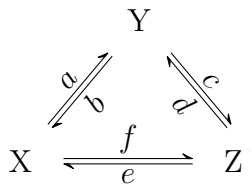

. (6.1)

If the system begins in state X for example, for a given time-step dt the possible outcomes are: transitioning to state Y, transitioning to state Z, or remaining in state X. The probability for transitioning from state X to state Y is given by [83]:

$$P_{T_{X\Rightarrow Y}} = a\ dt, \tag{6.2}$$

and similarly the probability of transition for X to Z is given by:

$$P_{T_{X\Rightarrow Z}} = f\ dt. \tag{6.3}$$

The remaining probability of the system not transitioning from state X is given by:

$$P_{T_{X\Rightarrow X}} = 1 - P_{T_{X\Rightarrow Y}} - P_{T_{X\Rightarrow Z}}, \tag{6.4}$$

ensuring that $\sum_j P_{T_{X\Rightarrow j}} = 1$. These equations can be generalized for any state i (X,

Y, Z in this case) as follows:

$$P_{T_{i\Rightarrow j}} = \mathbf{K}_{j,i}\, dt, \tag{6.5}$$

$$P_{T_{i\Rightarrow i}} = 1 - \sum_{j\neq i} P_{T_{i\Rightarrow j}}, \tag{6.6}$$

where j runs over the possible states for the system to transition to, and the matrix $\mathbf{K}$ is the rate matrix where each i, j element represents the transition between state j and state i constructed in the same way as equation 5.22. Equations 6.5 and 6.6 can be utilized to describe more complex schemes by creating the corresponding matrix $\mathbf{K}$ for the particular scheme.

In our system the time-step dt is determined by the speed of data acquisition. Our measurements are taken at a sampling rate of 10 kHz, so the time-step utilized in the simulations is $dt = \frac{1}{\text{sample rate}} = 10^{-4}$ s. The time-step dt needs to be sufficiently small such that $P_{T_{i\Rightarrow j}} < 1$ and $\sum_{j\neq i} P_{T_{i\Rightarrow j}} < 1$ [83] to ensure that there is at most one possible transition during a time-step. Since the maximum transition rate found experimentally in the previous chapter was ∼3000 Hz, the choice of dt meets these criteria.

In the implementation of this algorithm each rate in scheme 6.1 can be set individually along with tunnelling current value of each state, the sampling rate, and the length of the experiment. Gaussian noise can also be added to each state to make the simulation more realistic.

6.2 Variations in Current Noise with Current

In the section 3.2.2 it was shown that the noise associated with each state varies with the value of the tunnelling current signal. That is, the noise associated with measuring a value of 10 pA is different than that for 20 pA. Both experimentally and theoretically it was also shown that in the typical regime of the experiment, the tunnelling current noise varies linearly with tunnelling current. Experimental fits of

the linear function to describe the tunnelling current noise as a function of tunnelling current can be included in the code. These fits adjust the standard deviation of the Gaussian noise added to each state. If experimental fits are not possible, a constant value can be set instead in the code.

6.3 Comparison to Real Data

The derived rates from the experimental fits of telegraph noise datasets were utilized to set the parameters a, b, c, d, e, f in the simulation with $dt = 10^{-4}$ s and an experiment length of 3 s, giving a total of 30000 points for each simulation. The noise was set according to the equation of fit found experimentally from figure 3.10:

$$\Delta\sigma_{\mathrm{I}} = 0.0486 \text{ pA} \cdot \mathrm{x} + 0.7712 \text{ pA}, \tag{6.7}$$

where x is the mean tunnelling current value of the current charge state of the system (location of the peak of the Gaussian fit). The charge states were defined as $\mathrm{X} = \mathrm{DB}^{-}, \mathrm{Y} = \mathrm{DB}^{\mathrm{o}}, \mathrm{Z} = \mathrm{DB}^{+}$. Since the analysis was based off of a linear pathway, $e = f = 0$. Figure 6.2 shows the histograms recorded experimentally for a DB at various radial tip distances. As an example, using the analysis of Chapter 5 on this experimental dataset, the rates were found at each radial distance, along with the mean tunnelling current values for each state, and used as the parameters a, b, c, d in the simulations. The results of the simulations are shown in figure 6.3. The histograms are almost indistinguishable from the experimental results. The peaks are slightly sharper in these simulated data because the linear function found to calculate the noise in the signal appears to underestimate the true experimental noise. Also, the simulations and experiment are both stochastic so minor differences are expected. The similarities in trends, however, provide strong evidence that the signal-pair analysis method returns rates that are representative of the system dynamics and when utilized to simulate the system show a degree of self-consistency.

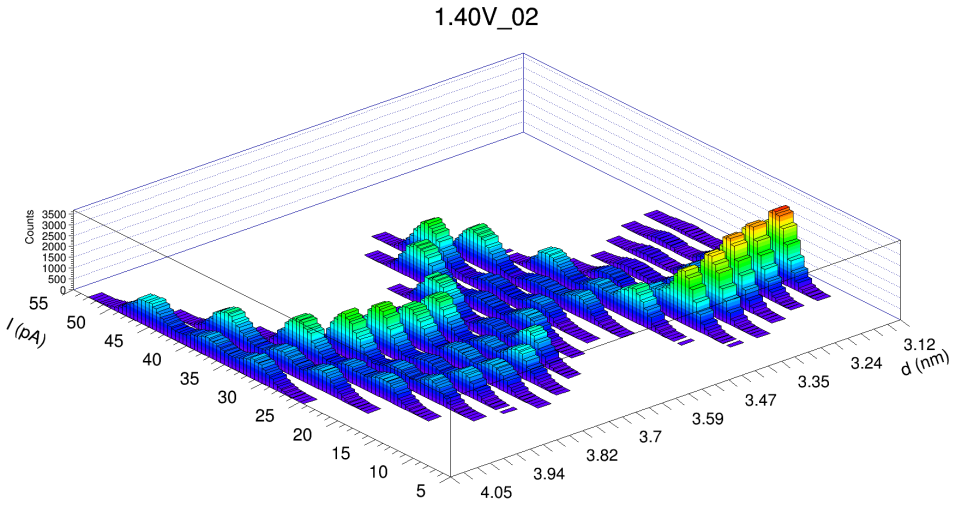

Figure 6.2: The series of 1D histograms created from telegraph data recorded at various distances from a DB centre. The mean of each histogram is shifted due to the atomic corrugation of the hydrogen-terminated surface.

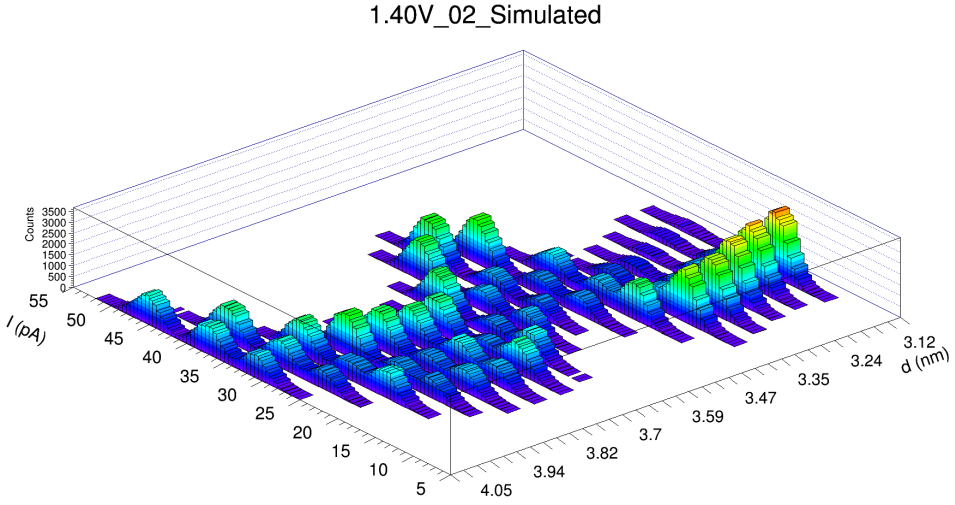

Figure 6.3: The series of 1D histograms created from telegraph data simulated with the rates calculated in the analysis of the these data in figure 6.2. The calculated rates when utilized in the simulations generate data which looks almost identical to these original experimental data.

As a further test, since these simulated data were created with known rates the

signal-pair analysis was repeated on these data. If the simulations were perfect, and the analysis method was also perfect, one would expect there to be negligible difference between the input rates in the simulations and the rates returned by the analysis of these simulated datasets. An average percentage difference for each rate a, b, c, d was calculated between the set rates in the simulation and the results of the analysis at each radial distance. It was found that each rate on average differed by 10–15 % from the known values in the simulation. While this is not an unacceptable difference when the stochastic nature of the system and simulations are considered, along with the simulation of noise not accurately representing these experimental data, it raises some doubt of whether the analysis is sufficient to accurately calculate physical rates from real experimental data. With the prior use of variants of the signal-pair analysis [18–20] illustrating that the method is reliable at reproducing known experimental rates, along with the reproduction of trends mentioned above, it is unlikely that the method itself is the major contributor to these differences. A control experiment still needs to be designed such that the STM is able to record tunnelling current data from a system with known transition rates to test the ability of the analysis method more rigorously.

The major cause of the differences between the set rates in the simulations and the rates found by the analysis of the simulated datasets is likely the simulations themselves. Only a basic simulation algorithm was implemented, which was reliant on a pseudo-random number generator [83]. More complex and computationally expensive algorithms exist [84] to model chemical transitions with improved accuracy [83]. In future work, it would be ideal to implement one of these algorithms instead and repeat the simulations and analysis tests. Another step before the roulette wheel algorithm is dismissed entirely would be to improve the simulation of the experimental noise, since the simulations overall are able to reproduce the experimental results well (Figures 6.2 and 6.3). It was seen in Figure 6.3 that the noise was underestimated by equation 6.7. The reason for the underestimation is in part due to the dependence of noise on the geometry of the tip, and local environment of the DB. Equation 6.7 was found in a different spatial location where there were no DBs around for several nanometers in all directions. A procedure needs to be implemented to characterize

the local noise in the tunnelling current in the neighbourhood of the DB under study before a telegraph experiment. This would give more representative equations to calculate noise in these simulations on a per-dataset basis.

6.4 Signal Pair Histogram Library

Despite the limitations of these simulated datasets to perfectly reproduce experimental results, they accurately capture the overall dynamics of a system based on scheme 6.1. With the ability to set each rate to arbitrary values, many variations in the general scheme can be achieved. In the previous section the states X, Y, and Z were associated with charge states, and e and f were both set to zero to eliminate the possibility of a direct transition between the negative and positive state. Returning to the general scheme (scheme 6.1), where there are no associated charge states (which bring physical limitations on possible schemes), any number of these rates can be set to zero. For instance, if a and b were set to zero, there would be no direct transition between state X and Y. These variations in pathways were found to manifest themselves in characteristic ways when looking at the signal-pair histograms originally introduced in section 5.2.3. These signal-pair histograms can provide a great deal of qualitative information about a system without any assumptions or detailed analysis. A library of histograms was created from simulations of many variations of scheme 6.1 in order to help develop an intuitive understanding when looking at signal-pair histograms of real experimental data.

6.4.1 Understanding the Signal Pair Histogram

Signal-pair histograms are 2D maps representing the entire space of these data. The population of each bin of the 2D plot is determined by equation 5.23 from section 5.2.3.

$$N(\tau, s_I, s_F) = \{s(t) \in s_I \pm \Delta s | s(t+\tau) \in s_F \pm \Delta s\}, \tag{5.23}$$

where s_I is the current bin value along the x-axis and s_F is bin value along the

y-axis. Δs is half of the width of the bin (identical bin sizes should be used for each axis) [18, 70]. τ does not represent time directly, but instead is the number of time-steps from $\tau = 0$. In order to convert τ to time it must be multiplied by $dt = \frac{1}{\text{sample rate}}$ where the sample rate is the speed of data acquisition. Again, in this case data were acquired at a rate of 10 kHz, so if $\tau = 2$ the corresponding time would be 200 μs. Each signal-pair histogram is generated at a fixed τ. When a series of histograms is generated for a range of τ the time evolution of the system can be observed.

The content of each 2D bin is calculated by starting at the lowest bin value along the x-axis. This bin value (s_I) is held fixed while $N(\tau, s_I, s_F)$ is calculated for each bin value (s_F) along the y-axis beginning from the lowest value. Once the range of y-bins has been spanned, the value of s_I increments to the next bin along the x-axis until the entire space of the dataset has been explored. The value of each 2D bin is the number of points in the dataset that started at the bin value along the x-axis at $\tau = 0$ that now have the associated bin value along the y-axis after a number of time-steps τ. Figure 5.4 from section 5.2.3 shows that at $\tau = 0$ there are 5 data points (shown in red) in the region of interest I1. This region represents a bin along the x-axis (I1=29 pA). After a time-step $\tau = 1$ (Figure 5.5) many of the data points have moved to different values outside of the region. The new values (I2) correspond to bins along the y-axis, so the bin (I1=29 pA, I2=27 pA) would have a value of 2 since two data points originally in I1 now have a value of 27 pA (I2) (shown in green). The bin (I1=29 pA, I2=29 pA) would have a value of 2, and the bin (I1=29 pA, I2=30 pA) would have a value of 1. This process is repeated for various values of τ to give snapshots of the system as shown in figure 5.7.

6.4.2 Qualitative Information from Signal-Pair Histograms

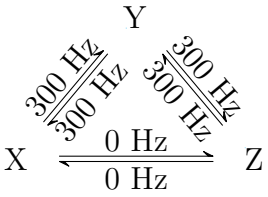

(6.8)

The scheme 6.8 was used to simulate a telegraph noise dataset with state X set at 10 pA, state Y set at 20 pA and state Z set at 30 pA. The signal-pair histogram for this dataset at $\tau = 0$ is shown below.

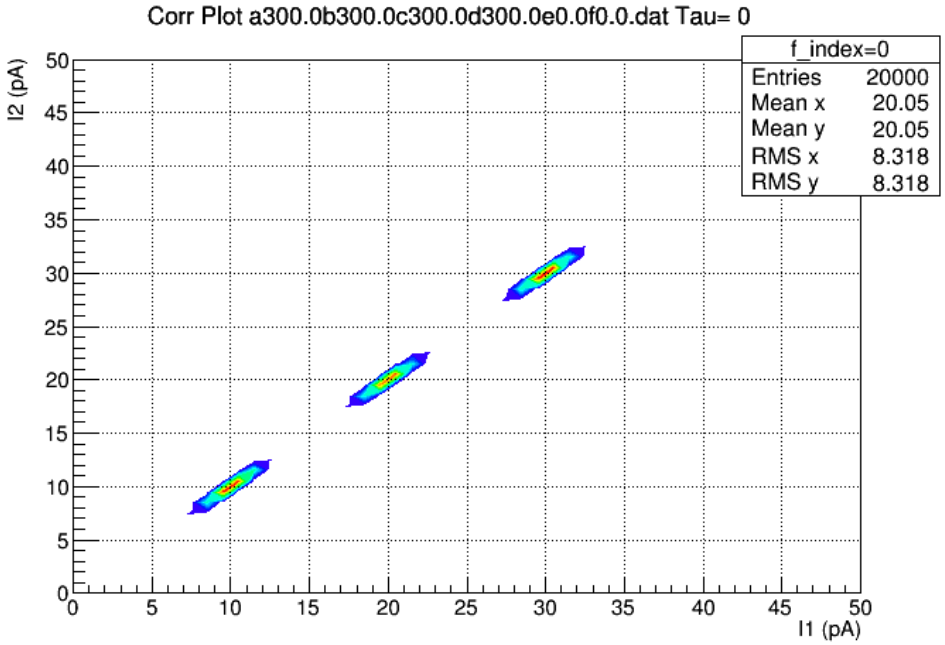

Figure 6.4: The signal-pair histogram corresponding to scheme 6.8 with simulated data. At $\tau = 0$ a diagonal is observed because all points map back to themselves since no transitions have occurred. Three distinct states can be observed travelling up along the diagonal corresponding to state X, Y, and Z respectively.

At $\tau = 0$ a diagonal line can be observed on the signal-pair histogram because no time-steps have occurred, so all points map back to themselves. The width of each region is due to the added noise in the simulation. If there were no noise, only the bin right at the centre of each region would be filled. Right away it can be seen there are three places in the histogram where the signal tends to be. Knowing nothing about the settings utilized to simulate this dataset, just by looking at the histogram it could be inferred that there are three states in the system located at 10 pA, 20 pA, and 30 pA respectively. It is easy to do so in this case because there is large separation between states and low noise. This identification can prove more difficult with real

data if the separation between states is small, and there are lots of noise contributions. The height of each peak (colour intensity) also gives an indication of more populous states. In this case since all of the rates are the same, none of the states have a significant bias towards them. Though the peak for state Y is slightly lower because there are two ways to leave state Y, as opposed to both X and Z which have one exit pathway, leaving Y less likely to be populated. Due to the random nature of the processes though, slight variations in peak heights can just be statistical, so extreme differences in peak height are generally a more reliable indication of a preference in the system. The next figure shows a signal-pair histogram for the same system at $\tau = 5$.

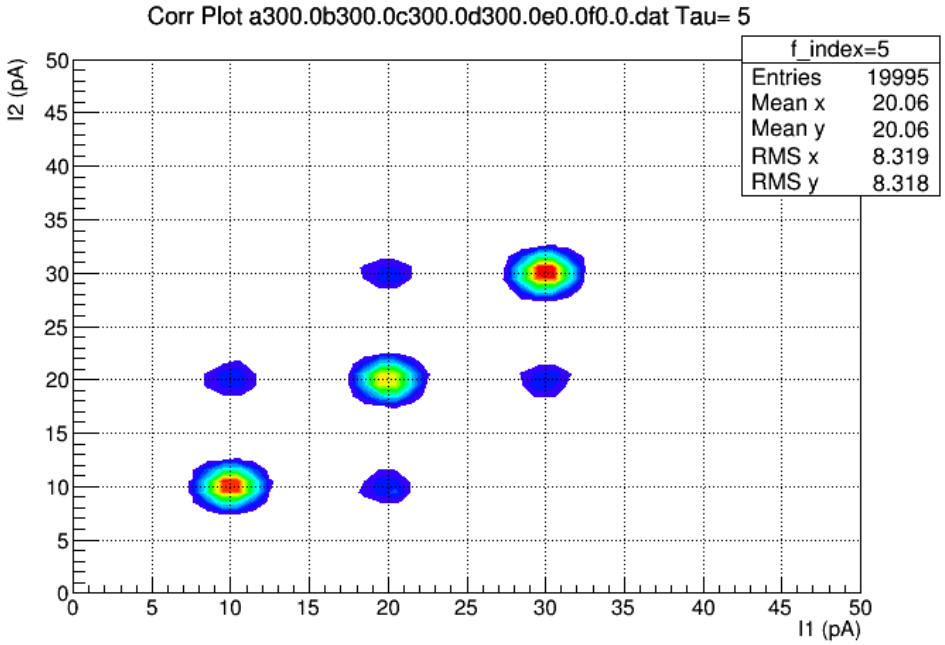

Figure 6.5: The signal-pair histogram corresponding to scheme 6.8 with simulated data. At $\tau = 5$ cross-peaks appear for all interior rates of similar magnitude, indicating transitions between those states.

After 5 time-steps other peaks begin to appear on the histogram between state X and Y and between state Y and Z. These cross-peaks represent transitions between these states. For instance the peak located at (I1=10 pA, I2=20 pA) indicates that after

5 time-steps a large number of data points that were originally at 10 pA at $\tau = 0$ are now at 20 pA, and vice-versa for the complementary cross peak at (I1=20 pA, I2=10 pA). The next figure shows the system at $\tau = 15$.

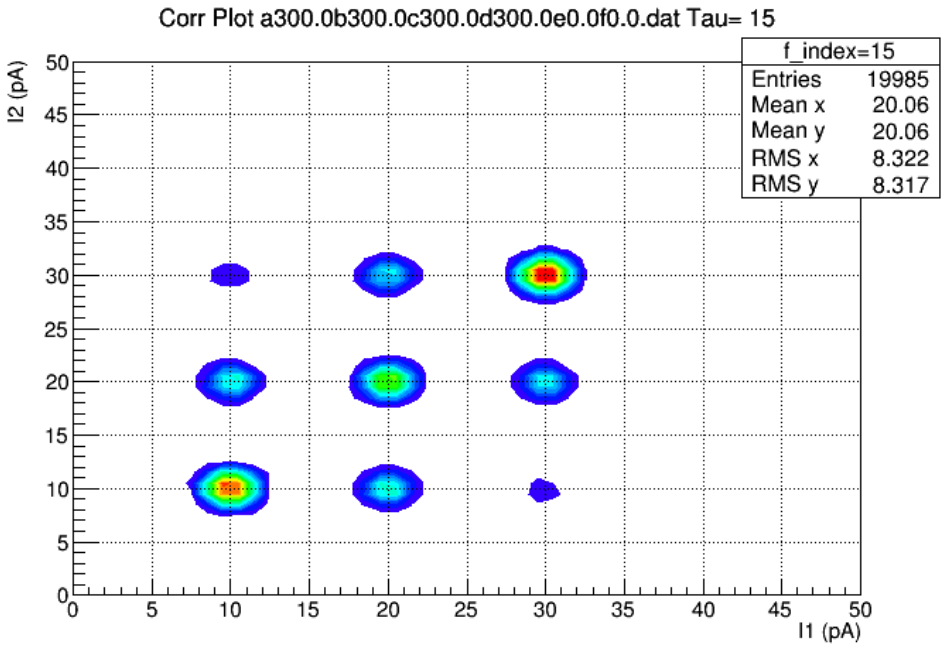

Figure 6.6: The signal-pair histogram corresponding to scheme 6.8 with simulated data. At $\tau = 15$ cross-peaks between X and Z appear. They appear much later because there is no direct transition between the two states in the scheme.

After 10 more time-steps cross-peaks appear between state X and state Z. This is counter-intuitive since cross-peaks represent transitions between states, and according to scheme 6.8 there are no possible transitions. The reason these cross-peaks appear is because a sufficient number of time-steps have elapsed such that points that were in state X transitioned to state Y and have now transitioned to state Z, and vice-versa. These cross-peaks actually represent transitions between state X and Z mediated through state Y in this particular example. The next figure shows the system at $\tau = 30$.

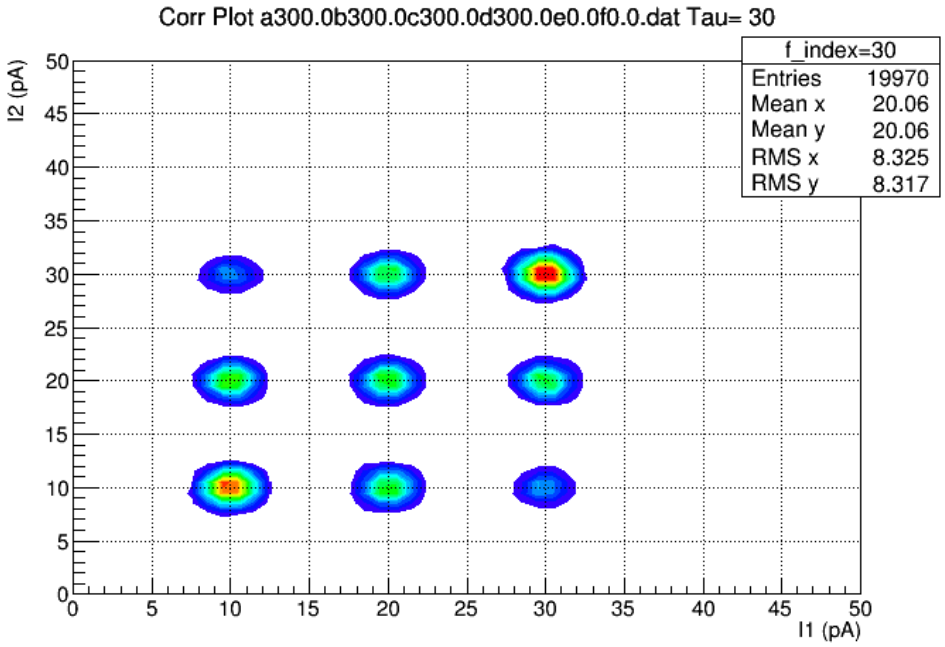

Figure 6.7: The signal-pair histogram corresponding to scheme 6.8 with simulated data. At $\sim \tau = 30$ the system has reached a steady-state; the subsequent histograms for increasing τ do not deviate much from what is observed here.

In this figure, the system has reached a steady-state. As τ increases no more cross-peaks appear and the relative heights of the peaks do not change significantly. The population of state Y appears to be lower than state X and Z. Again, this could be because Y has two leaving and entering processes, so the system doesn't have as much of a probability to stay in state Y, or simply just a consequence of the statistical nature of the transitions. It would be difficult to draw any conclusions based on peak heights in this plot because the differences are not very extreme. Looking solely at Figures 6.4 to 6.7 a number of qualitative aspects of the system can be deduced about the system. The first aspect was that there are three states in the system. The next aspect is the likely values of these states given their locations on the plot. Finally it could be deduced that cross-peaks first appear between X and Y and Y and Z before they appear much later between X and Z. The order at which the cross-peaks appear, and how long it takes the system to reach a steady-state strongly hints at

the fact that there is a linear pathway between X, Y, and Z.

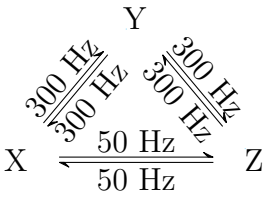

(6.9)

By allowing for a slow transition between X and Z (Scheme 6.9), the intuition gained in the first example was put to the test. In figure 6.8 it can be seen that the cross-peaks between states show up in the same order as when there was no direct transition between X and Z. The difference, however, is that with slow direct transitions allowed, the cross-peaks between X and Z show up almost two times faster at $\tau = 7$ as opposed to $\tau = 15$ in the previous example. The system also reaches a steady-state much more quickly at $\tau = 20$ compared to $\tau = 30$.

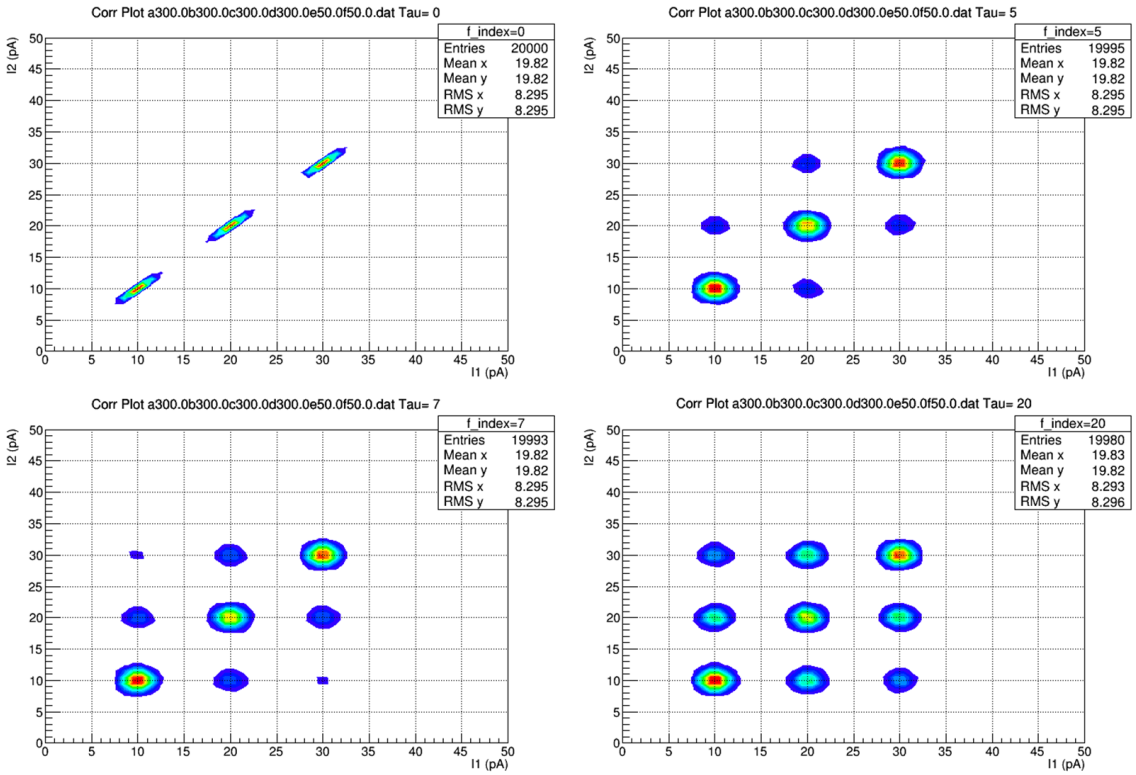

Figure 6.8: Signal-pair histograms corresponding to scheme 6.9 at various values of τ. A slow direct transition is now allowed between states X and Z in this scheme. Appearance of cross-peaks follows the same order as the purely linear scheme, however, they appear at much earlier times.

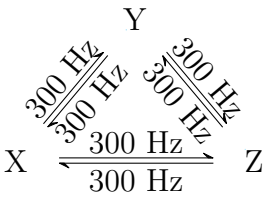

(6.10)

Making all rates have the same value, and allowing all possible transitions (Scheme 6.10), it can be seen in figure 6.9 that all of the cross-peaks appear at the same time. The system also reaches steady state very quickly at $\tau = 15$

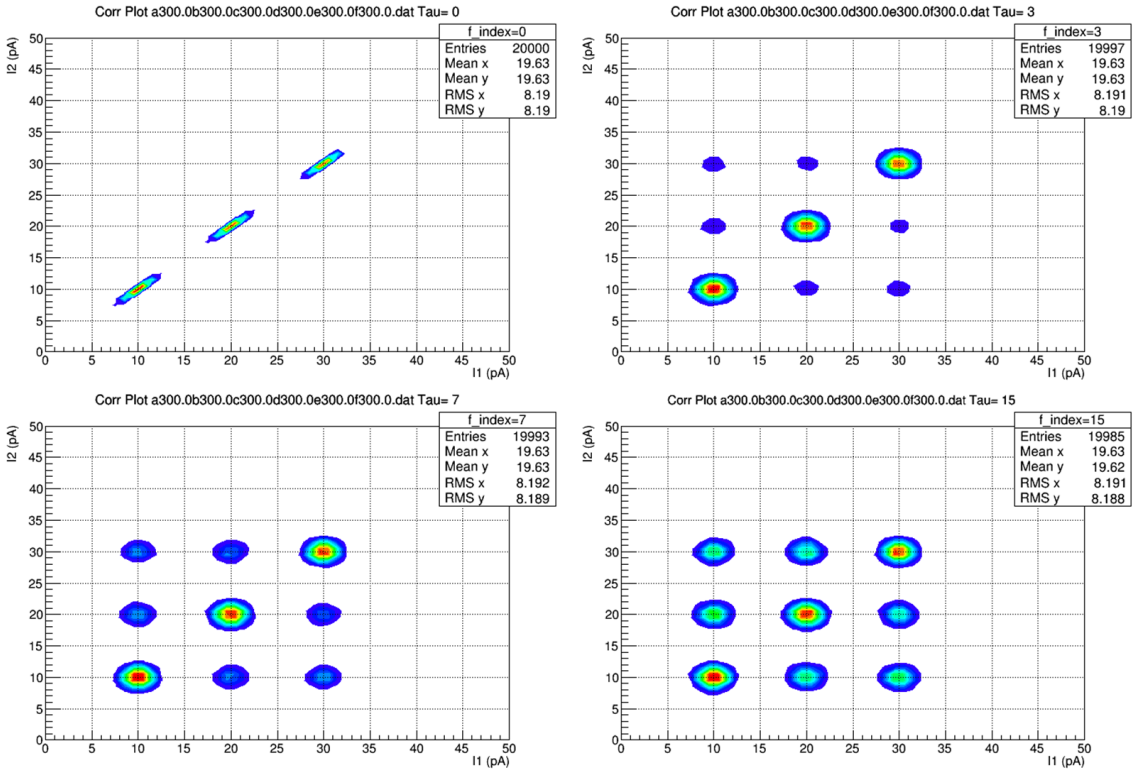

Figure 6.9: Signal-pair histograms corresponding to scheme 6.10 at various values of τ. A transition of equal magnitude to the other rates is now allowed between states X and Z in this scheme. In this case all the cross-peaks appear at the same time, which is expected since all rates are equal, and all states are directly connected. This system reaches a steady-state very quickly.

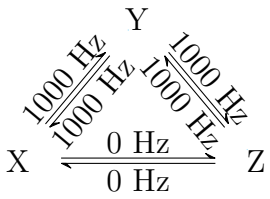

(6.11)

A linear pathway with very fast rates between states (Scheme 6.11) could possibly resemble the previous scheme 6.10 with all allowed transitions. However, figure 6.10 shows that even with very fast transitions, the order at which the cross-peaks show up is the same as for scheme 6.8. It also shows that it still takes the system until

approximately $\tau = 22$ to reach a steady-state. The reason it takes the system so long to reach a steady state in these plots is due to the lack of a direct transition between X and Z. Even with the faster rates between X and Y and Y and Z, the cross-peaks are still mediated through the middle state which limits the frequency of the system travelling all the way from X to Y to Z and vice-versa. Based on these examples, it seems that the signature of a linear pathway is the order in which the cross-peaks appear, and the time it takes to reach a steady-state.

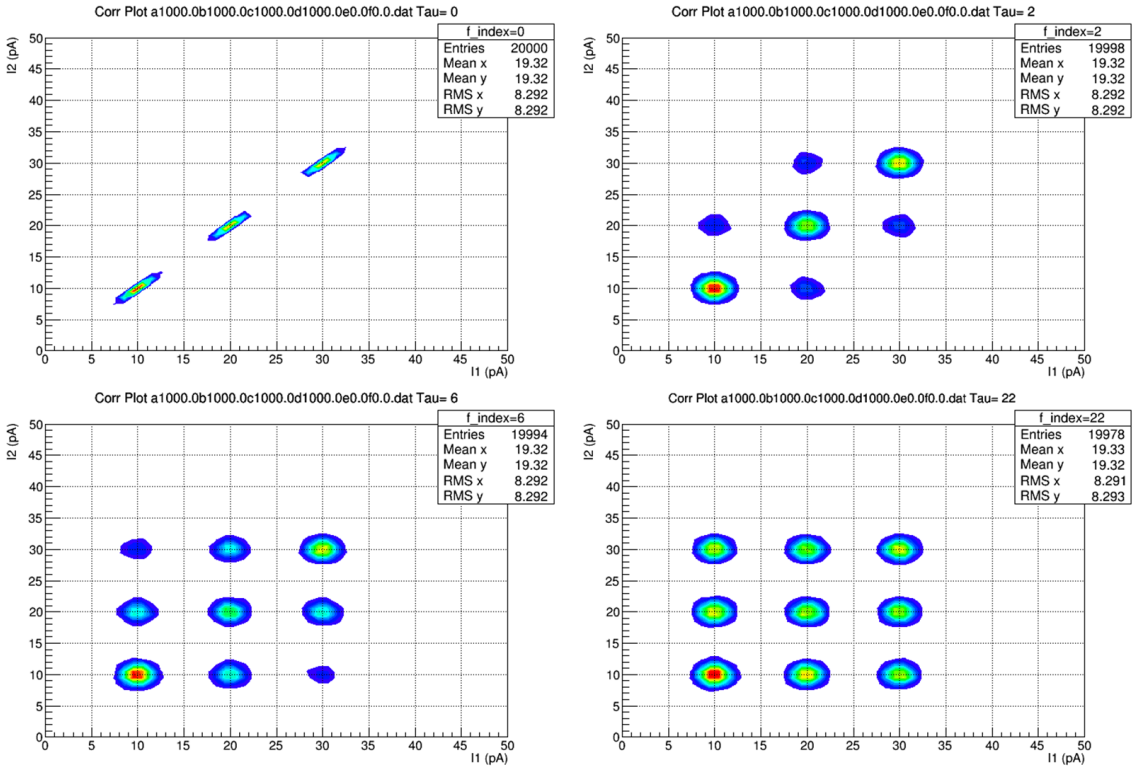

Figure 6.10: Signal-pair histograms corresponding to scheme 6.11 at various values of τ. In this scheme, the notion that very fast rates will dramatically change the speed and order in which the cross-peaks appear is tested. The system reaches steady-state extremely quickly, but the order of appearance of the cross-peaks still remains true for a linear pathway.

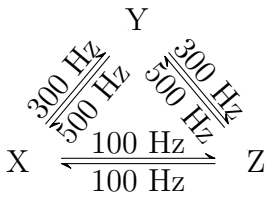

(6.12)

It is worth mentioning though that it is impossible to conclusively determine whether a system follows a linear scheme or not based only on signal-pair histograms. There are many conceivable combinations of rates that could mimic the order the peaks appear, along with the time it takes the system to reach steady-state. The scheme 6.12 is one such example. Figure 6.11 shows that the cross peaks appear in the same order as in the previous linear scheme 6.11, around the same τ. It also shows that steady-state is reached in almost the same τ. While all of those aspects are similar, the steady-state images in both figures 6.10 and 6.11 are quite different. Looking at the last panel in figure 6.10 it could be guessed that the rates are all of a similar magnitude (which they are) since all of the state peaks have similar heights. In comparison, looking at figure 6.11 the peak height of state X is significantly higher than all the other state peaks in the last panel. It could be guessed that state X has the largest difference between rates entering and leaving the state, with slower leaving rates than entering rates causing a pooling of the system in state X. An inspection of scheme 6.12 reveals that this is indeed the case. The system has a net rate of 400 Hz to leave state X while it has a net rate of entering state X of 600 Hz.

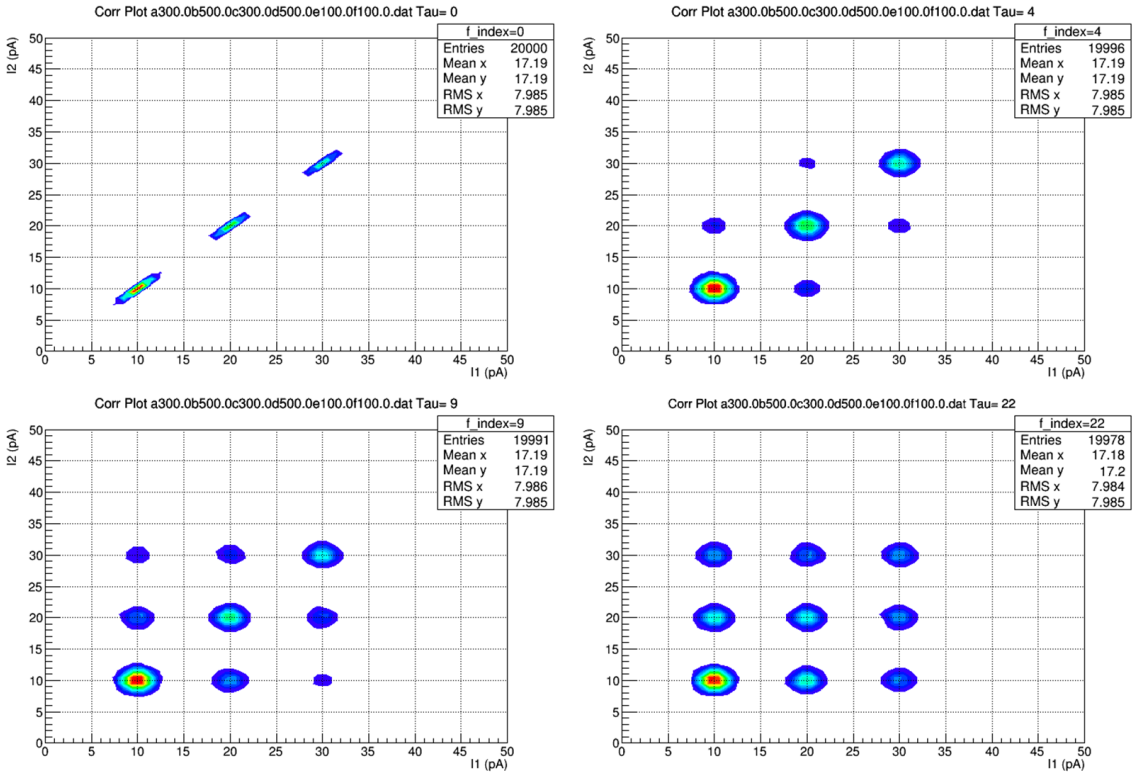

Figure 6.11: Signal-pair histograms corresponding to scheme 6.12 at various values of τ. The signal-pair histograms show a similar evolution and appearance of cross-peaks as the linear scheme 6.11, however, the steady-state histograms are not the same.

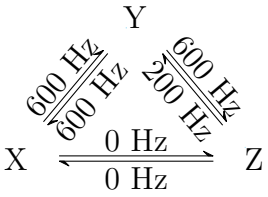

(6.13)

These net rates into and out of states can manifest themselves with fairly distinct signatures in many cases. The scheme 6.13 has a much slower step for leaving state Z than entering it. Intuitively one would expect then that the system would spend the majority of its time in state Z since it enters fast and leaves slowly. Figure 6.12 shows the signal-pair plots as the system evolves in time. Once the system has reached a

steady-state it is very obvious that the system tends to stay in state Z since the height of the Z peak is significantly higher than the others.

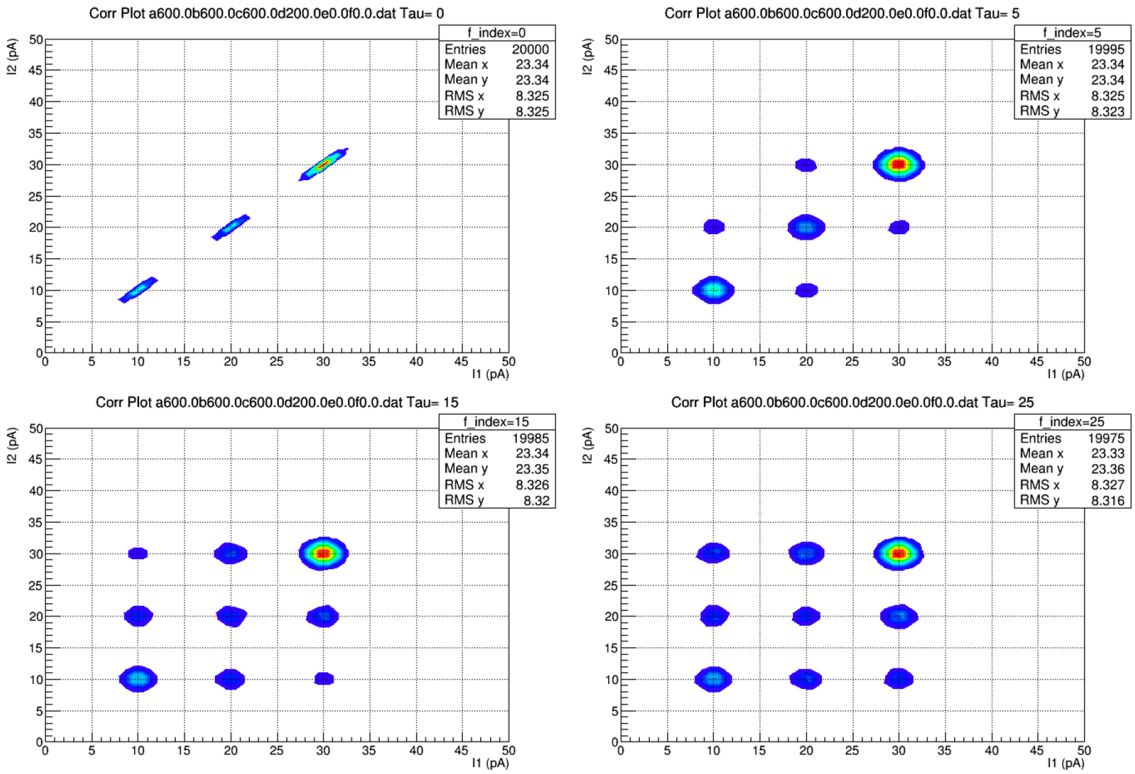

Figure 6.12: Signal-pair histograms corresponding to scheme 6.13 at various values of τ. These histograms follow the expected evolution with time for a linear scheme. At steady-state the histogram reveals a potential state with the largest difference between the rates into and out of the state, with the entering rate being larger than the leaving rate.

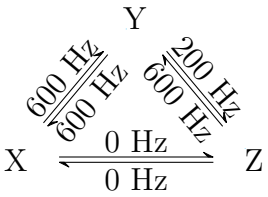

(6.14)

With only a minor change to scheme 6.13, a remarkably different behaviour can be observed in the signal-pair histograms. This time scheme 6.14 has a slow rate

entering the Z state, and a much faster rate leaving the state. In this case it would be a fair assumption that the Z state would be the least populated since it enters slowly and leaves fast now. Again, this intuition proves correct as figure 6.13 shows that once a steady-state has been reached that the height of the Z state is significantly lower than the others. From these two examples (Figures 6.12 and 6.13) it seems as if signal-pair histograms can be useful in assessing where the largest differences between the rates into and out of a state exist within a system, as they tend to have unique signatures once a steady-state is reached.

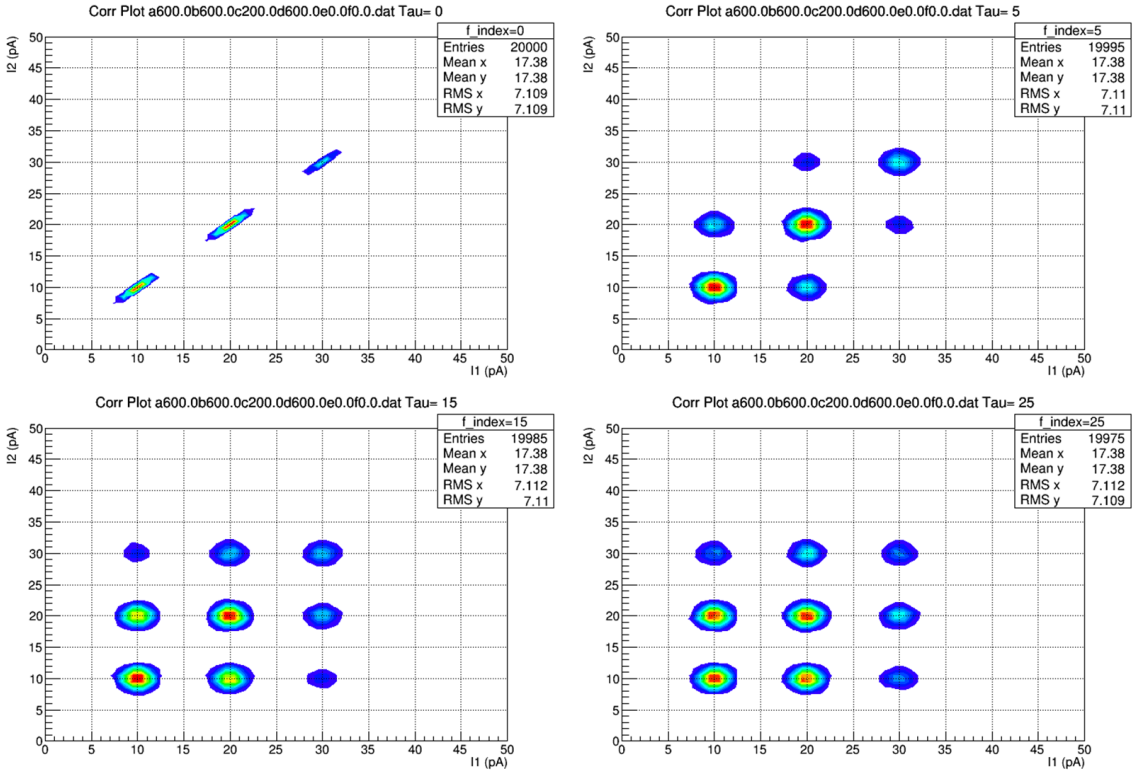

Figure 6.13: Signal-pair histograms corresponding to scheme 6.14 at various values of τ. This scheme is exactly the same as the previous scheme, with only two rates switched. The switch has a large effect on how the histogram looks at steady-state. At steady-state the histogram reveals that state Z likely has a much faster rate leaving the state than entering it.

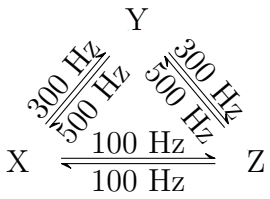

(6.15)

All of the examples so far have dealt with a linear pathway from state X to Y to Z as the backbone of the scheme (with the occasional direct transitions allowed between X and Z). It was shown in figures 6.4 to 6.7 that linear schemes such as scheme 5.1 have characteristic dynamics when datasets are viewed as signal-pair histograms. The scheme 6.15 is still a linear pathway, however it does not take the conventional path with the state Y as the middle state. Figure 6.14 shows a very different sequence of events when compared to figures 6.4 to 6.7 for instance. Here cross-peaks first appear between X and Y and X and Z, with nothing between Y and Z around the same time cross peaks appear in these data generated from scheme 6.8. Finally after sufficient time, cross peaks appear between state Y and Z, as they did between X and Z for scheme 6.8. Utilizing the signal-pair histograms it is possible to predict the pathway that a system might be taking between states.

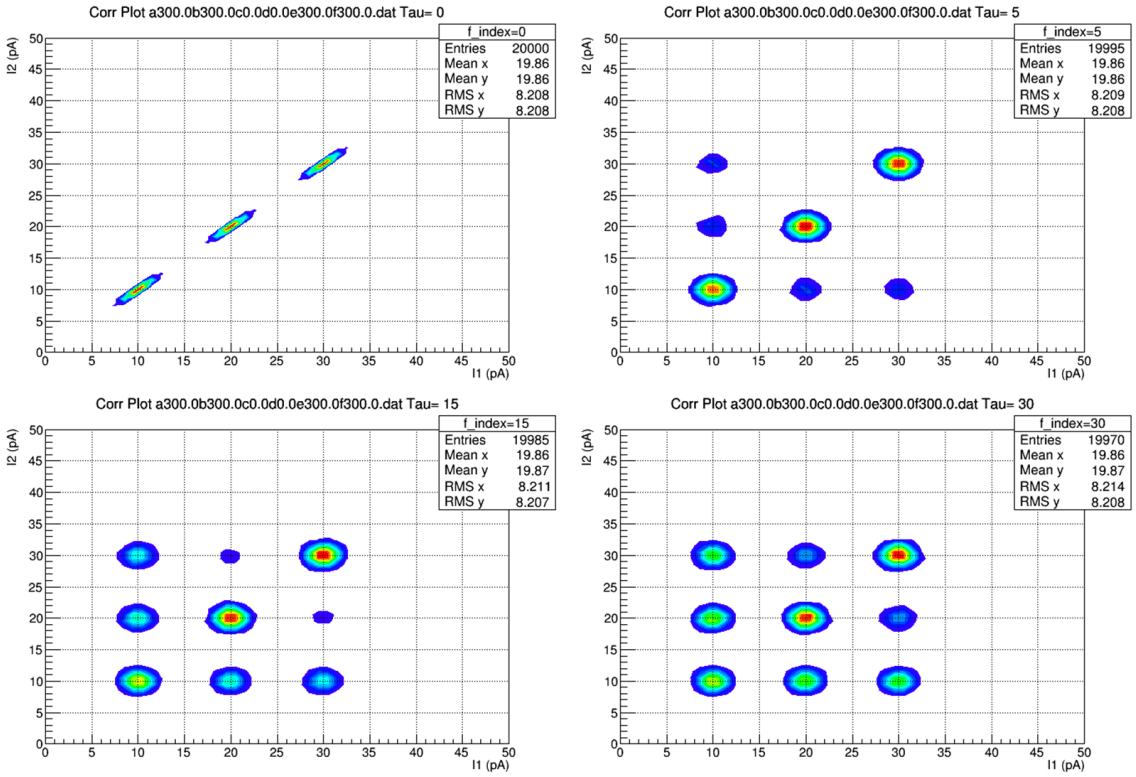

Figure 6.14: Signal-pair histograms corresponding to scheme 6.15 at various values of τ. This scheme still follows a linear pathway, however, now state X is the middle state instead of state Y. The evolution of the histograms shows that cross peaks appear in a very different order than when Y was the middle state, allowing one to differentiate between the two cases just by observing the signal-pair histograms.

6.4.3 Conclusions and Application to Real Data

Signal-pair histograms are useful tools to help visualize time-traces of data which contain dynamic information about multi-state systems. The real power, however, is the ability to quickly and easily simulate many schemes and then observe how the histograms behave. A subset of simulations were presented here in order to help illustrate how qualitative information can be gained through these plots. With the signal-pair histograms it is possible to determine how many states are in a system, and what values they correspond to. It is also possible to predict the type of pathway

between states in the system, and determine where the largest difference between ingoing and outgoing rates may be present. Returning to some experimental data first presented in section 5.2.3, many of the observations made through detailed analysis could have been predicted directly from figures such as figure 5.7. Looking at this figure, it can be seen that there are three distinct states, and the evolution of the system has features of a linear pathway, where the middle state is the intermediate state. At the particular location where these data were collected it can also be predicted that there is a slower rate leaving the positive state (filling of an electron to a neutral DB) than entering it (emptying of an electron from the neutral DB). Indeed this is actually the case, as it was found experimentally that all of the rates r_1 to r_3 are ~ 300 Hz while the filling rate r_4 is ~ 200 Hz!

Chapter Seven

Conclusions and Outlook

7.1 Summary of Experiments

The main goal of this project was to study in detail the charging dynamics of a silicon dangling bond (DB) on the surface of a hydrogen-terminated n-type silicon (100)–2×1 sample with a positive sample bias. DBs have many potential applications in the realm of ultra-low power electronics [2, 12–16], including binary wires based on a quantum cellular automata (QCA) architecture [10, 11]. These applications require a deep understanding of the fundamental properties of DBs to ensure that functional and reliable devices can be developed. DBs have the ability to contain zero, one, and two electrons, corresponding to positive, neutral, and negative charge states. When a scanning tunneling microscope (STM) tip was brought within a certain radial proximity of the DB it was observed that the tip influenced its charge state. The STM tip drove transitions between these states that could be recorded as a form of telegraph noise within the STM tunnelling current. An analytical framework to uncover these transition rates from the telegraph noise was developed based on biophysical techniques [18–20, 70], which allowed for the exploration of a vast parameter space of possible experiments.

7.2 Summary of Major Results

The exploration began with measuring the telegraph noise of DBs at set bias voltages with varying radial tip distances from the DB centres. A basic model was constructed to explain the behaviour observed when the telegraph traces at each distance were placed into 1D histograms, revealing three distinct states whose pop-

ulations depended on distance (Chapter 4). The model was based on assumptions that the dominant filling mechanism of the DB was electron tunneling events from the tip, while the emptying processes were tunneling events from the DB state into the conduction band of the silicon bulk. Since the tunneling current from the tip is exponentially sensitive to distance, it was assumed that the filling rates should also have this behaviour, while the emptying rates should remain constant and independent of distance. While the agreement of these experimental data to the model was good, the model did not reveal any specific values for the transition rates between states.

In order to calculate the transition rates between charge states, a biophysical analysis method was adapted and implemented (Chapter 5). The adaptations to the method provided the ability to rapidly test many potential theories of how the DB could transition between states without the need to re-derive equations for each test. It was found that the DB followed a linear charging pathway (Scheme 5.1) with filling rates between 50 Hz–3000 Hz that were exponentially dependant on the radial tip distance (from DB centre), and insensitive to bias voltage. It was also found that the emptying rates were between 50 Hz–1000 Hz and essentially independent of radial tip distance, but increased with bias voltage.

Other important experimental considerations were explored in addition, such as the dependence of the rates on the initial set height of the tip, and how the character of the tunnelling current noise changes depending on the amount of tunneling current being measured. It was found that over the range of tip heights normally utilized in the experiment the initial tip height did not significantly alter the value of the calculated rates. Although, it was determined that larger tip sample separations resulted in poor signal quality and an inability to gather useful data. The noise in the tunnelling current measurements was investigated, and it was experimentally demonstrated that the noise in the tunnelling current is linearly dependent on the tunnelling current itself. That is, if the tunnelling current increases, the noise increases along with it. This result had important implications for how experiments were carried out and what ranges of currents could be used to observe DB charging dynamics through telegraph noise.

In order to gain further insight into the dynamics of DBs, a stochastic simulation algorithm was implemented to generate telegraph data. These data could be tailored in the simulation to have any desired transition rates between states. With the use of custom data, many theoretical datasets were generated and analysed to see if any relations to the experimental data could be found. It was shown that a 2D representation of these telegraph data, known as signal-pair histograms [18, 70] was able to provide qualitative insight into the dynamics of DBs without any sophisticated analysis (Chapter 6).

7.3 Extensions and Further Work

The work here only begins to explore the entire space of possible parameters and variations of experiments. It has laid the groundwork to chase many of the open questions that remain as a result of these explorations, and fully characterize the fundamental properties of DBs. One of the big open questions that has arisen from these studies is if there are actually intrinsic transition rates between states in the absences of the tip, and if so what is the role of defects and dopants on these rates. The effects of temperature on the rates need to be investigated as well since all of these experiments were conducted at liquid helium temperatures. Faster STM current pre-amplifiers need to be pursued in order to delve into regimes where states are currently impossible to resolve within these telegraph data. The functional form of the relationship between bias and emptying rates also needs to be investigated in more detail, since only a small range of biases were explored here. Identifying if there is actually a linear relationship or some other functional dependence would go a long way to understanding the charging dynamics in the absence of a tip and bias.

Experiments with two tunnel-coupled DBs are also of great interest [5], and have already shown some preliminary results with more than three states in the telegraph signals. The in-lab atomic fabrication techniques are also constantly improving, making it possible to create DB pairs with consistent separation between them (allowing for more reproducible experiments).

In order to analyse these new data with 3+ states, work has already also begun

on generalizing the analysis framework to N-states and N-rates. Not only will this new framework be extremely useful for DB telegraph experiments, it opens up the potential of analysing many other phenomena with state transitions. Among these possibilities is to complete the analogous study of DBs on boron doped p-type silicon as it has already been shown that these DBs may exhibit binary behaviours [77, 78] instead of the three states observed here.

Regardless of which direction these experiments take, it seems there is endless potential to answer some very fundamental questions about charge dynamics at the nanoscale.

Bibliography

[1] P. M. Solomon, "IBM Research Report (Unpublished)." March, 2010.

[2] Robert A. Wolkow, Lucian Livadaru, Jason Pitters, Marco Taucer, Paul Piva, Mark Salomons, Martin Cloutier, Bruno V. C. Martins, *Field-Coupled Nanocomputing, Silicon Atomic Quantum Dots Enable Beyond-CMOS Electronics*, vol. 8280. Springer, 2014.

[3] I. Žutić, J. Fabian, and S. D. Sarma, "Spintronics: Fundamentals and applications," *Rev. Mod. Phys.* **76** no. April, (2004) 323–410, arXiv:0405528 [cond-mat].

[4] Y. C. Tseng and S. B. Darling, "Block copolymer nanostructures for technology," *Polymers (Basel).* **2** no. 4, (2010) 470–489.

[5] J. L. Pitters, L. Livadaru, M. B. Haider, and R. A. Wolkow, "Tunnel coupled dangling bond structures on hydrogen terminated silicon surfaces," *J. Chem. Phys.* **134** (2011) .

[6] M. Taucer, L. Livadaru, P. G. Piva, R. Achal, H. Labidi, J. L. Pitters, and R. A. Wolkow, "Single-Electron Dynamics of an Atomic Silicon Quantum Dot on the H:Si(100)–(2x1) Surface," *Phys. Rev. Lett.* **112** no. June, (2014) 256801.

[7] L. Livadaru, P. Xue, Z. Shaterzadeh-Yazdi, G. A. Dilabio, J. Mutus, J. L. Pitters, B. C. Sanders, and R. A. Wolkow, "Dangling-bond charge qubit on a silicon surface," *New J. Phys.* **12** (2010) , arXiv:0910.1797.

[8] S. R. Schofield, P. Studer, C. F. Hirjibehedin, N. J. Curson, G. Aeppli, and D. R. Bowler, "Quantum engineering at the silicon surface using dangling bonds.," *Nat. Commun.* **4** (Jan., 2013) 1649.

[9] B. Naydenov and J. J. Boland, "Engineering the electronic structure of surface dangling bond nanowires of different size and dimensionality.," *Nanotechnology* **24** no. 27, (July, 2013) 275202.

[10] W. P. C S Lent, P D Tougaw and G. H. Bernstein, "Quantum Cellular Automata," *Nanotechnology* **4** (1993) 49–57, arXiv:0808.0679.

[11] C S Lent, P D Tougaw, "A device architecture for computing with quantum dots," *Proc. IEEE* **85** no. 4, (1997) 541–557.

[12] L. Lu, W. Liu, and M. O'Neill, "QCA systolic array design," *IEEE Trans. Comput.* **62** no. 3, (2013) 548–560.

[13] S. Chen, H. Xu, K. E. J. Goh, L. Liu, and J. N. Randall, "Patterning of sub-1 nm dangling-bond lines with atomic precision alignment on H:Si(100) surface at room temperature," *Nanotechnology* **23** (2012) 275301.

[14] K. E. J. Goh, S. Chen, H. Xu, J. Ballard, J. N. Randall, and J. R. Von Ehr, "Using patterned H-resist for controlled three-dimensional growth of nanostructures," *Appl. Phys. Lett.* **98** no. 2011, (2011) 98–101.

[15] H. Kawai, F. Ample, Q. Wang, Y. K. Yeo, M. Saeys, and C. Joachim, "Dangling-bond logic gates on a Si(100)-(2 » 1)Ű́H surface," *J. Phys. Condens. Matter* **24** (2012) 095011.

[16] R. Robles, M. Kepenekian, S. Monturet, C. Joachim, and N. Lorente, "Energetics and stability of dangling-bond silicon wires on H passivated Si(100)," *J. Phys. Condens. Matter* **24** (2012) 445004, arXiv:1206.2154.

[17] L. Livadaru, J. Pitters, M. Taucer, and R. A. Wolkow, "Theory of nonequilibrium single-electron dynamics in STM imaging of dangling bonds on

a hydrogenated silicon surface," *Phys. Rev. B - Condens. Matter Mater. Phys.* **84** (2011) 1–14, arXiv:1105.2332.

[18] A. Hoffmann and M. T. Woodside, "Signal-pair correlation analysis of single-molecule trajectories," *Angew. Chemie - Int. Ed.* **50** (2011) 12643–12646.

[19] I. V. Gopich and A. Szabo, "Theory of the statistics of kinetic transitions with application to single-molecule enzyme catalysis," *J. Chem. Phys.* **124** no. 2006, (2006) 0–21.

[20] I. V. Gopich, D. Nettels, B. Schuler, and A. Szabo, "Protein dynamics from single-molecule fluorescence intensity correlation functions," *J. Chem. Phys.* **131** (2009) 1–5.

[21] M. F. Crommie, C. P. Lutz, and D. M. Eigler, "Confinement of electrons to quantum corrals on a metal surface.," *Science* **262** no. 5131, (1993) 218–220.

[22] D. M. Eigler and E. K. Schweizer, "Positioning single atoms with a scanning tunnelling microscope," *Nature* **344** no. 6266, (Apr, 1990) 524–526.

[23] C. J. Chen, *Introduction to Scanning Tunneling Microscopy (Monographs on the Physics and Chemistry of Materials)*. Oxford University Press, 2007.

[24] G. Binnig and H. Rohrer, "Scanning tunneling microscopy," *Surf. Sci.* **126** (1983) 236–244.

[25] J. W. Lyding, "UHV STM nanofabrication: Progress, technology spin-offs, and challenges," *Proc. IEEE* **85** no. 4, (1997) 589–600.

[26] M. Schmid, "Schematic diagram of a scanning tunneling microscope." Creative commons attribution sharealike 2.0 austria license. https://upload.wikimedia.org/wikipedia/commons/f/f9/ScanningTunnelingMicroscope_schematic.png.

[27] Omicron, *Omicron Nanotechnology The LT STM User's Guide*.

[28] N. W. Ashcroft and N. D. Mermin, *Solid State Physics*. Brooks Cole, 1976.

[29] V. Ukraintsev and J. T. Yate, "The role of nickel in Si(001) roughening," *Surf. Sci.* **346** (1996) 31–39.

[30] Y. J. Chabal and K. Raghavachari, "New Ordered Structure for the H-Saturated Si(100) Surface: The (3x1) Phase," *Phys. Rev. Lett.* **54** (Mar, 1985) 1055–1058.

[31] C. C. Cheng and J. T. Yates, "H-induced surface restructuring on Si(100): Formation of higher hydrides," *Phys. Rev. B* **43** (Feb, 1991) 4041–4045.

[32] J. J. Boland, "Scanning tunnelling microscopy of the interaction of hydrogen with silicon surfaces," *Adv. Phys.* **42** no. July 2015, (1993) 129–171.

[33] A. Sherman, "In situ removal of native oxide from silicon wafers," *Journal of Vacuum Science & Technology B: Microelectronics and Nanometer Structures* **8** no. 4, (Jul, 1990) 656.

[34] K. Hata, T. Kimura, S. Ozawa, and H. Shigekawa, "How to fabricate a defect free Si(001) surface," *Journal of Vacuum Science & Technology A: Vacuum, Surfaces, and Films* **18** no. 4, (2000) 1933.

[35] H. Bender, S. Verhaverbeke, M. Caymax, O. Vatel, and M. M. Heyns, "Surface reconstruction of hydrogen annealed (100) silicon," *J. Appl. Phys.* **75** no. 100, (1994) 1207–1209.

[36] G. F. Cerofolini, C. Galati, S. Reina, L. Renna, N. Spinella, D. Jones, and V. Palermo, "Formation of terraced, nearly flat, hydrogen-terminated, (100) Si surfaces after high-temperature treatment in H2 of single-crystalline silicon," *Phys. Rev. B - Condens. Matter Mater. Phys.* **72** no. 100, (2005) 1–10.

[37] A. P. Legg, "Characterization of Point Projection Microscope for In-Line Holography," Master's thesis, University of Alberta, 2013.

[38] M. Rezeq, J. Pitters, and R. Wolkow, "Tungsten nanotip fabrication by spatially controlled field-assisted reaction with nitrogen," *J. Chem. Phys.* **124** (2006) .

[39] V. T. Binh, N. Garcia, and S. Purcell, "Electron Field Emission from Atom-Sources: Fabrication, Properties, and Applications of Nanotips," in *Advances in Imaging and Electron Physics*, pp. 63–153. Elsevier BV, 1996.

[40] H.-W. Fink, "Point source for ions and electrons," *Physica Scripta* **38** no. 2, (Aug, 1988) 260–263.

[41] J. L. Pitters, R. Urban, C. Vesa, and R. A. Wolkow, "Tip apex shaping of gas field ion sources," *Ultramicroscopy* **131** (Aug, 2013) 56–60.

[42] E. W. Müller and K. Bahadur, "Field Ionization of Gases at a Metal Surface and the Resolution of the Field Ion Microscope," *Physical Review* **102** no. 3, (May, 1956) 624–631.

[43] R. G. Forbes, "Field electron and ion emission from charged surfaces: a strategic historical review of theoretical concepts," *Ultramicroscopy* **95** (May, 2003) 1–18.

[44] R. Urban, J. L. Pitters, and R. A. Wolkow, "Gas field ion source current stability for trimer and single atom terminated W(111) tips," *Applied Physics Letters* **100** no. 26, (2012) 263105.

[45] A. Bellec, D. Riedel, G. Dujardin, N. Rompotis, and L. N. Kantorovich, "Dihydride dimer structures on the Si(100):H surface studied by low-temperature scanning tunneling microscopy," *Phys. Rev. B* **78** no. 16, (Oct, 2008) .

[46] T. C. Shen, C. Wang, G. C. Abeln, J. R. Tucker, J. W. Lyding, P. Avouris, and R. E. Walkup, "Atomic-scale desorption through electronic and vibrational excitation mechanisms.," *Science* **268** (1995) 1590–1592.

[47] E. Foley, A. Kam, J. Lyding, and P. Avouris, "Cryogenic UHV-STM Study of Hydrogen and Deuterium Desorption from Si(100)," *Phys. Rev. Lett.* **80** no. 100, (1998) 1336–1339.

[48] Q. H. Yuan, Q. S. Li, K. D. Wang, and Z. F. Liu, "Theoretical investigation of an intermediate in the STM tip-induced atomic process on H/Si(100) surfaces," *Phys. Rev. B - Condens. Matter Mater. Phys.* **81** no. 100, (2010) 1–7.

[49] T. Kleinpenning, "On noise and random telegraph noise in very small electronic devices," *Physica B: Condensed Matter* **164** no. 3, (Sep, 1990) 331–334.

[50] J. Schaffert, M. C. Cottin, A. Sonntag, H. Karacuban, C. a. Bobisch, N. Lorente, J.-P. Gauyacq, and R. Möller, "Imaging the dynamics of individually adsorbed molecules.," *Nat. Mater.* **12** no. 3, (Mar., 2013) 223–7.

[51] M. B. Haider, J. L. Pitters, G. a. Dilabio, L. Livadaru, J. Y. Mutus, and R. a. Wolkow, "Controlled coupling and occupation of silicon atomic quantum dots at room temperature," *Phys. Rev. Lett.* **102** no. JANUARY, (2009) 2–5, `arXiv:0807.0609`.

[52] H. Raza, "Theoretical study of isolated dangling bonds, dangling bond wires, and dangling bond clusters on a H:Si (001) - (2x1) surface," *Phys. Rev. B - Condens. Matter Mater. Phys.* **76** (2007) 1–8, `arXiv:0611417 [cond-mat]`.

[53] T. Yoshida and H. Hasegawa, "Ultrahigh-Vacuum Contactless Capacitance–Voltage Characterization of Hydrogen-Terminated-Free Silicon Surfaces," *Japanese Journal of Applied Physics* **39** no. Part 1, No. 7B, (Jul, 2000) 4504–4508.

[54] T. Blomquist and G. Kirczenow, "Controlling the charge of a specific surface atom by the addition of a non-site-specific single impurity in a Si nanocrystal," *Nano Lett.* **6** (2006) 61–65.

[55] A. Bellec, D. Riedel, and G. Dujardin, "Electronic properties of the n -doped hydrogenated silicon (100) surface and dehydrogenated structures at 5 K," *Phys. Rev. B* **80** no. 24, (Dec., 2009) 245434.

[56] K. Teichmann, M. Wenderoth, S. Loth, R. G. Ulbrich, J. K. Garleff, A. P. Wijnheijmer, and P. M. Koenraad, "Controlled Charge Switching on a Single Donor with a Scanning Tunneling Microscope," *Phys. Rev. Lett.* **101** (Aug, 2008) 076103.

[57] D. H. Lee and J. A. Gupta, "Tunable Field Control Over the Binding Energy of Single Dopants by a Charged Vacancy in GaAs," *Science* **330** no. 6012, (Dec, 2010) 1807–1810.

[58] S. M. Sze, *Physics of Semiconductor Devices*. Wiley-Interscience, 1981.

[59] J. L. Pitters, P. G. Piva, and R. A. Wolkow, "Dopant depletion in the near surface region of thermally prepared silicon (100) in UHV," *J. Vac. Sci. Technol. B Microelectron. Nanom. Struct.* **30** no. 100, (2012) 021806.

[60] M. Taucer, L. Livadaru, P. G. Piva, R. Achal, H. Labidi, J. L. Pitters, and R. A. Wolkow, "Supplemental Material: Single Electron Dynamics of an Atomic Silicon Quantum Dot on the H-Si(100) 2x1 Surface," *Phys. Rev. Lett.* **112** no. June, (2014) 256801.

[61] P. L. Krapivsky, S. Redner, and E. Ben-Naim, *A Kinetic View of Statistical Physics*. Cambridge University Press, 2010.

[62] *Python 2.7*, 2014. `https://www.python.org`.

[63] R. Brun and F. Rademakers, "ROOT - An Object Oriented Data Analysis Framework," in *AIHENP'96 Workshop, Lausane*, vol. 389, pp. 81–86. 1996. `http://root.cern.ch/`.

[64] S. van der Walt, S. C. Colbert, and G. Varoquaux, "The NumPy Array: A Structure for Efficient Numerical Computation," *Computing in Science & Engineering* **13** no. 2, (Mar, 2011) 22–30.

[65] J. D. Hunter, "Matplotlib: A 2D Graphics Environment," *Computing in Science & Engineering* **9** no. 3, (2007) 90–95.

[66] *EasyGUI*, 2013. `http://easygui.sourceforge.net/`.

[67] R. Phillips, J. Kondev, J. Theriot, and H. Garcia, *Physical Biology of the Cell*. Garland Science, 2012.

[68] R. L. Ott and M. T. Longnecker, *An Introduction to Statistical Methods and Data Analysis*. Duxbury Press, 2008.

[69] W. H. Press, B. P. Flannery, S. A. Teukolsky, and W. T. Vetterling, *Numerical Recipes in FORTRAN*. Cambridge University Press, 1989.

[70] A. Hoffmann, D. Nettels, J. Clark, A. Borgia, S. E. Radford, J. Clarke, and B. Schuler, "Quantifying heterogeneity and conformational dynamics from single molecule FRET of diffusing molecules: recurrence analysis of single particles (RASP).," *Phys. Chem. Chem. Phys.* **13** (2011) 1857–1871.

[71] S. A. Rice, *Advances in Chemical Physics (Volume 137)*. Wiley-Interscience, 2008.

[72] A. Hoffmann and M. T. Woodside, "Signal-Pair Correlation Analysis of Single-Molecule Trajectories Supplemental Material," *Angew. Chemie - Int. Ed.* (2011) .

[73] J. Keizer, *Statistical Thermodynamics of Nonequilibrium Processes*. Springer, 2012.

[74] R. M. Feenstra, "Electrostatic potential for a hyperbolic probe tip near a semiconductor," *J. Vac. Sci. Technol. B Microelectron. Nanom. Struct.* **21** no. 2003, (2003) 2080.

[75] D. Kitchen, *Atom-by-atom substitution of transition metals in GaAs adn visualization of hole-mediated interactions*. PhD thesis, 2006.

[76] S. Loth, *Atomic Scale Images of Acceptors in III-V Semiconductors*. PhD thesis, 2008.

[77] A. Bellec, *Transfert de charges a l'echelle atomique sur la surface de silicium (100) hydrogenee*. Thesis, 2008.

[78] A. Bellec, L. Chaput, G. Dujardin, D. Riedel, L. Stauffer, and P. Sonnet, "Reversible charge storage in a single silicon atom," *Phys. Rev. B* **88** no. 24, (Dec., 2013) 241406.

[79] J. Milton and T. Ohira, *Mathematics as a Laboratory Tool: Dynamics, Delays and Noise*. Springer, 2014.

[80] R. M. L. Evans, "Rules for transition rates in nonequilibrium steady states," *Phys. Rev. Lett.* **92** no. April, (2004) 150601–1, `arXiv:0402527 [cond-mat]`.

[81] R. M. L. Evans, "Detailed balance has a counterpart in non-equilibrium steady states," *J. Phys. A: Math* **293** (2005) , `arXiv:0408614 [cond-mat]`.

[82] H. Qian and L. M. Bishop, "The chemical master equation approach to nonequilibrium Steady-state of open biochemical systems: Linear Single-molecule enzyme kinetics and nonlinear biochemical reaction networks," *Int. J. Mol. Sci.* **11** (2010) 3472–3500.

[83] N. Yildirim and C. Kazanci, *Computer Methods, Part C, Volume 487 (Methods in Enzymology), Deterministic and stochastic simulation and analysis of biochemical reaction networks: The lactose operon example*, vol. 487. Academic Press, 2011.

[84] D. T. Gillesple, "Exact Stochastic Simulation of couple chemical reactions," *J. Phys. Chem.* **81** no. 1, (1977) 2340–2361.

Appendix A

Additional Images

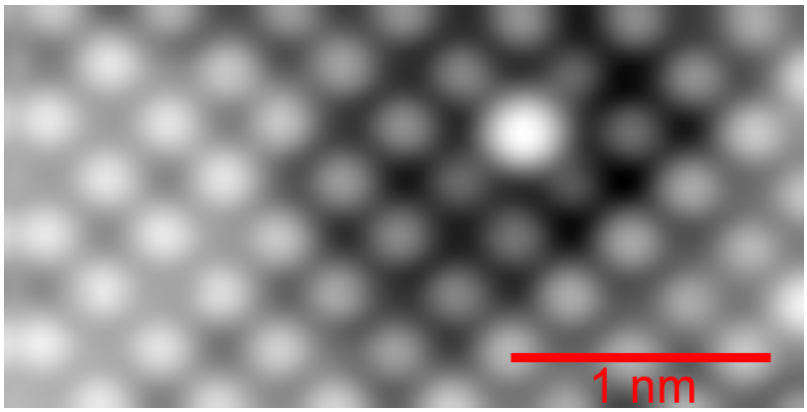

Figure A.1: A high resolution STM image of an atomic silicon dangling bond on the surface of a hydrogen terminated n-type silicon (100)–2×1 wafer. The dangling bond is the brightest feature in the middle of the image, where an open orbital exists instead of a hydrogen atom. The image was acquired at a sample bias of 1.6 V and a current of 30 pA. The STM tip utilized to acquire this image was extremely sharp, giving an image with minimal distortion of the atoms.

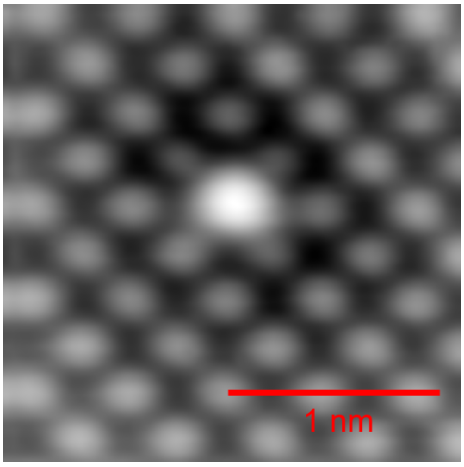

Figure A.2: The same dangling bond (DB) as in figure A.1. In this image a minor tip crash occurred prior to imaging, likely resulting in a change in the tip structure (dulling it). The shape of the atoms in the image have now changed slightly (they're less circular). The subtle changes illustrate the sensitivity of the STM resolution based on tip sharpness.

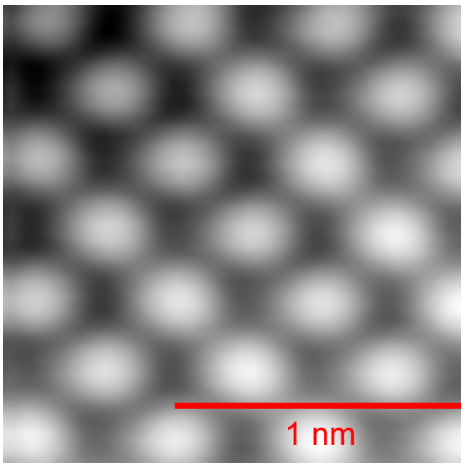

Figure A.3: A similar illustration as in figure A.2 of an image of hydrogen atoms after a minor tip crash. The resolution between atoms is significantly worse than in image 1.1. Larger tip crashes can destroy the atomic resolution altogether, or create false artifacts or features in images.

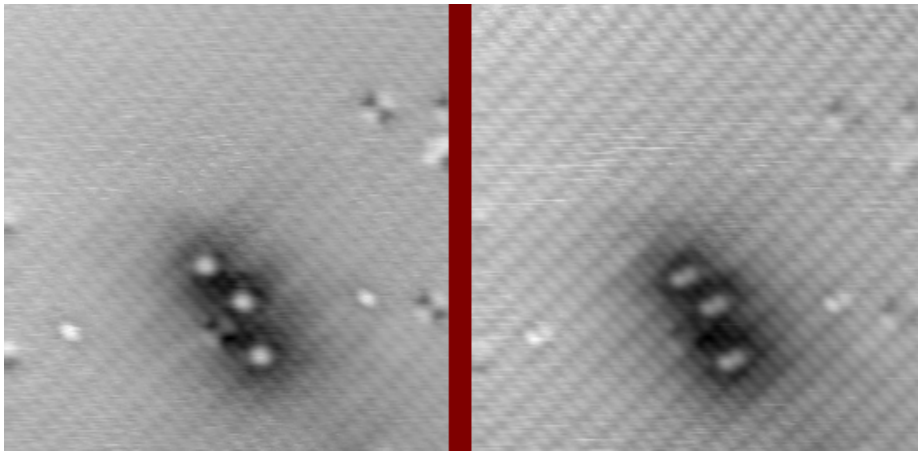

Figure A.4: Two STM image taken at a bias of 1.35 V and a current of 30 pA. The first image is of three dangling bonds (DBs) taken with a fairly sharp tip. The second image is of the same DBs after a major tip crash. In the second image the DBs appear to have split into two features. This type of multi imaging is the artifacts described in figure A.3.

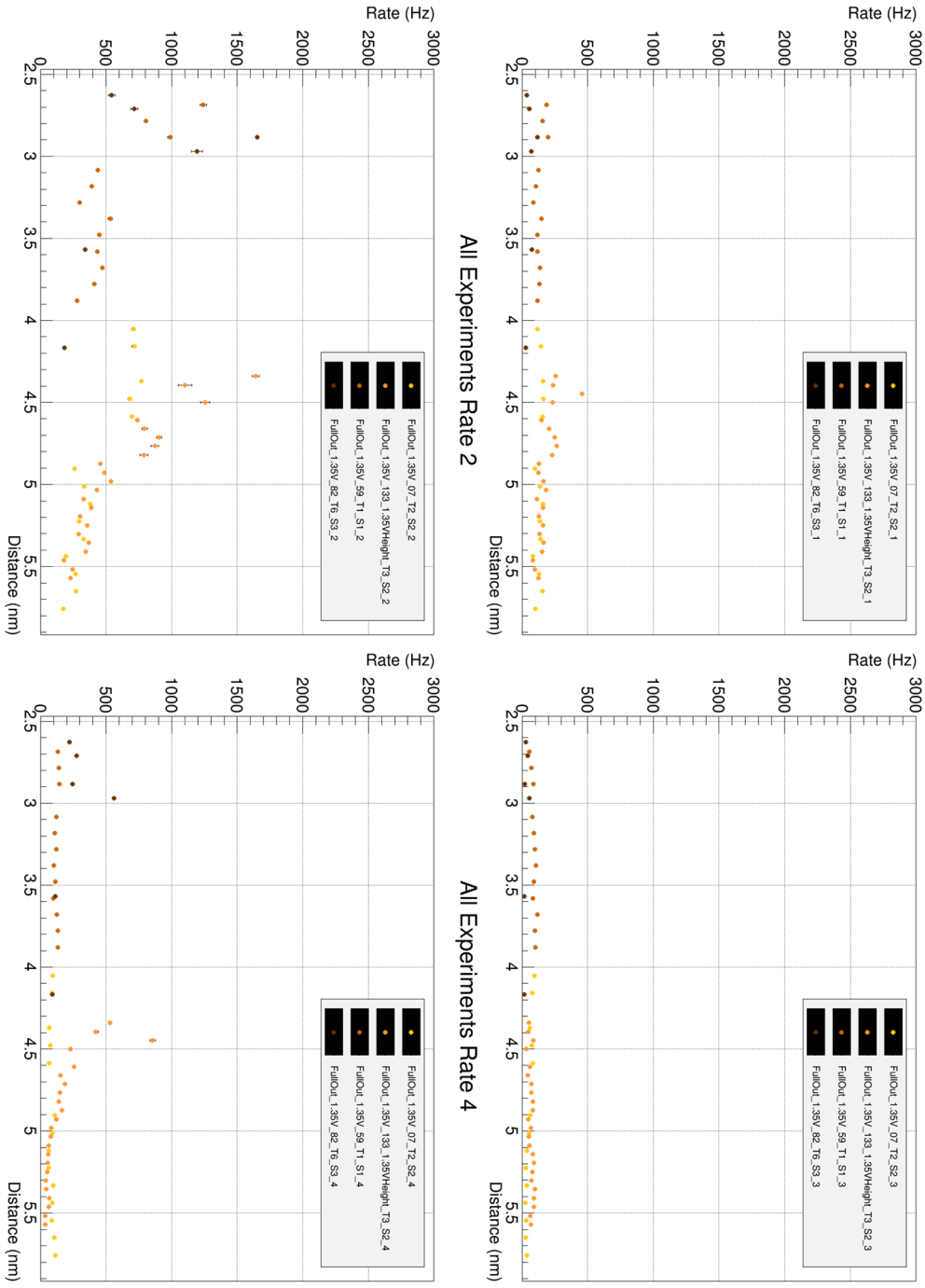

Figure A.5: Larger view of figure 5.11.

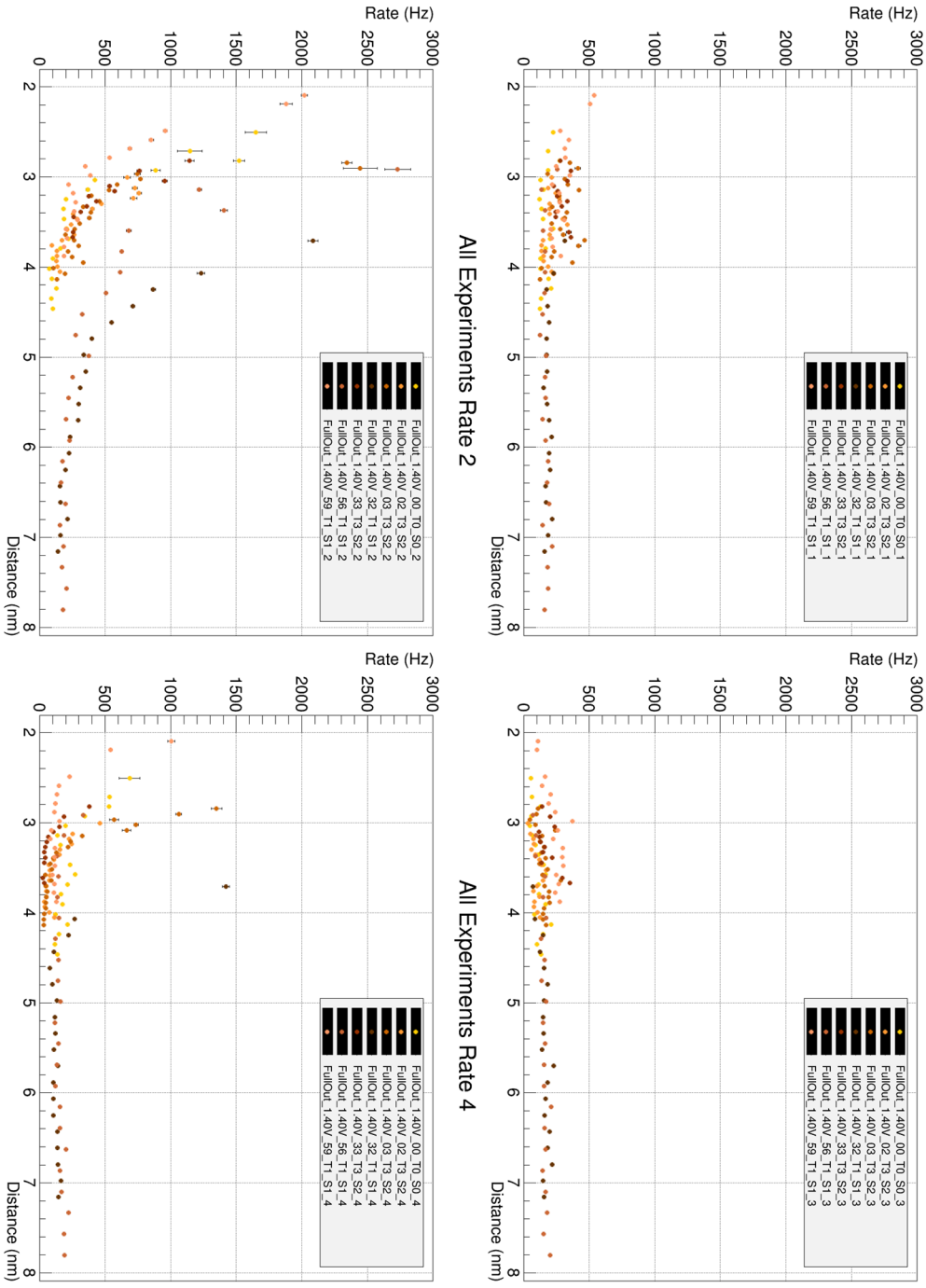

Figure A.6: Larger view of figure 5.12.

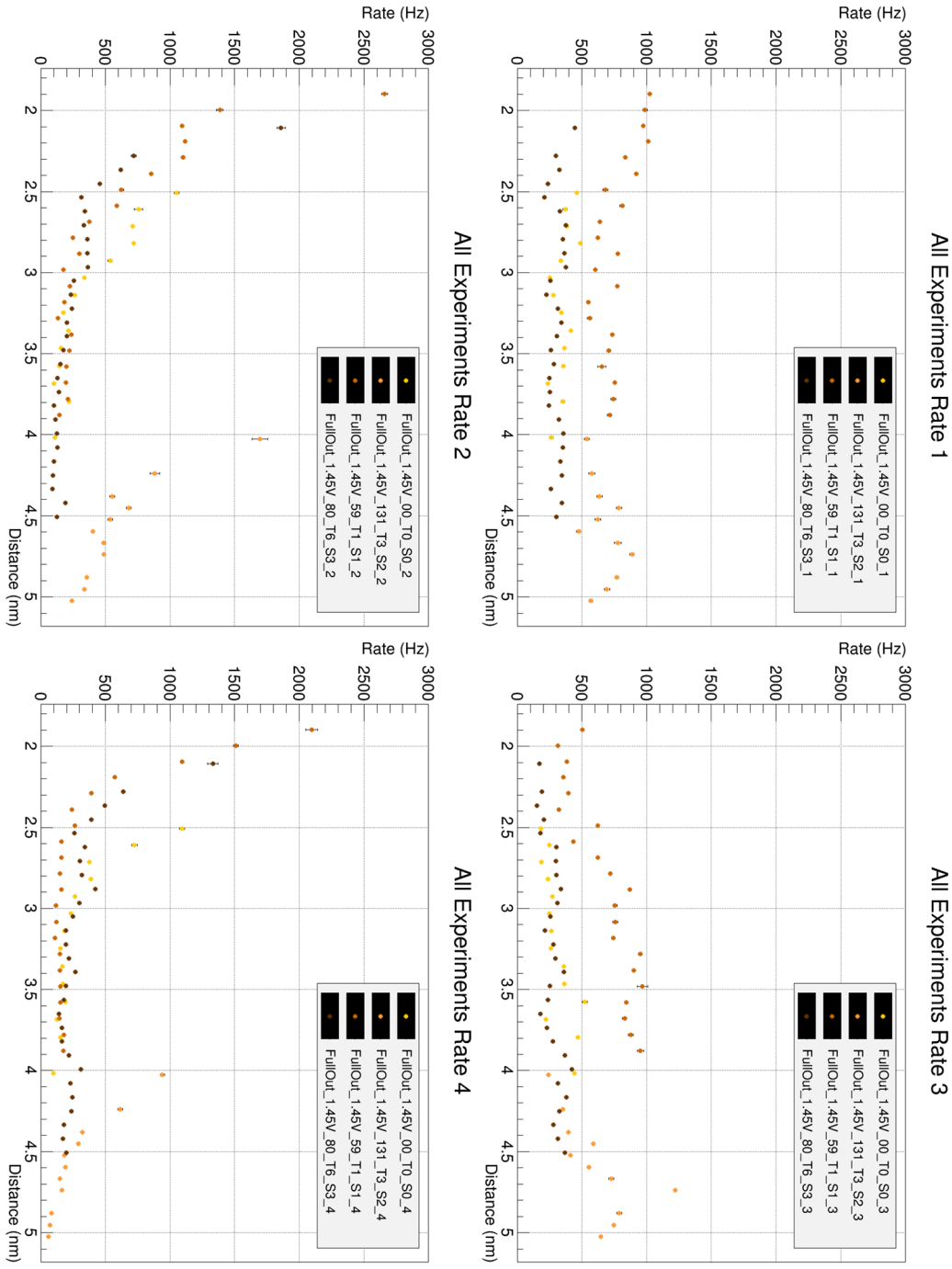

Figure A.7: Larger view of figure 5.13.

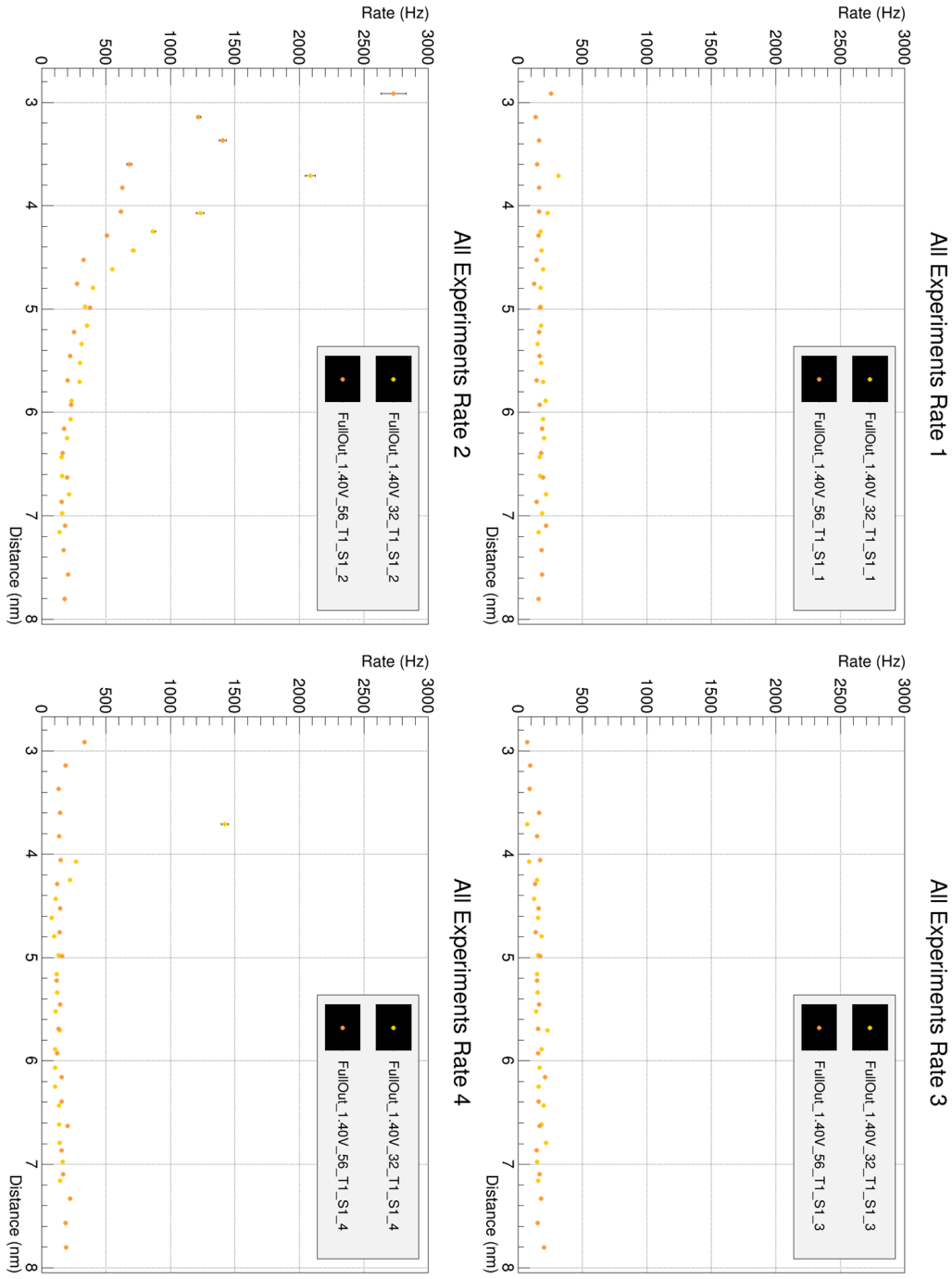

Figure A.8: Larger view of figure 5.24.